Mechanochemical Route to Novel High Entropy Materials for Rechargeable Batteries and Water Splitting Electrocatalysis

1. Lithium-ion Batteries; Electrode Materials; Electrochemical Properties

2. Water Splitting Electrocatalysts; Oxygen Evolution Reaction; Hydrogen Evolution Reaction

3. High Entropy Materials; Sulfides; Oxides; Oxyfluorides; Mechanochemical Synthesis

TECHNISCHE UNIVERSITÄT DARMSTADT

Vom Fachbereich Material- und Geowissenschaften
der Technischen Universität Darmstadt

Zur Erlangung des akademischen Grades
DOKTOR DER NATURWISSENSCHAFTEN (Dr. rer. nat.)

genehmigte Dissertation von
Ling Lin geboren in People's Republic of China

1. Gutachten: Prof. Dr. -Ing. Horst Hahn
2. Gutachten: Prof. Dr. rer. nat. Wolfgang Donner

Darmstadt 2023

Ling Lin: Mechanochemical Route to Novel High Entropy Materials for Rechargeable Batteries and Water Splitting Electrocatalysis
Darmstadt, Technische Universität Darmstadt,
Year thesis published in TUprints 2023
Date of the viva voce 30.11.23

Erklärung zur Dissertation

Hiermit versichere ich, dass ich meine Dissertation selbstständig und nur mit den angegebenen Quellen und Hilfsmitteln angefertigt habe. Diese Arbeit hat in gleicher oder ähnlicher Form noch keiner Prüfungsbehörde vorgelegen.

Darmstadt, 19.07.2023
Ling Lin

Abstract

Owing to the significantly growing consumption of fossil fuels and emerging environmental concerns, new sustainable energy sources and innovative energy storage solutions are gaining significance in contemporary society. Hydrogen is being considered as a promising clean and renewable energy source, but efficient production to meet demand remains a challenge. Electrocatalytic water splitting is a potential pathway, however, its practical realization requires the development of stable, low-cost, and highly active catalysts. Furthermore, in order to optimize the harnessing of renewable energy sources, particularly those with inherent variability, there is a burgeoning requirement for energy storage systems, notably exemplified by the prominence and extensive investigation of lithium-ion batteries (LIBs) in scientific discourse. Among the various components of these devices, the electrode material is a crucial part that greatly affects the performance and cost of rechargeable batteries. Frequently, the enhancement of energy technologies necessitates the discovery and development of optimized materials, underscoring the criticality of exploring novel substances for energy conversion and storage purposes. In this context, catalysts and electrode materials hold particular importance, and investigating their composition-structure-property relationships becomes indispensable for facilitating future advancements in the field.

In recent years, high entropy materials (HEMs) have emerged as a promising class of materials for various applications, due to their distinctive structural features, customizable chemical composition, and resulting adjustable functional properties. The application of the high entropy concept to the energy field also offers opportunities for the design and the synthesis of novel materials with unprecedented properties.

In this dissertation, a novel mechanochemical method was successfully applied to synthesize HEMs, including high entropy oxides, oxyfluorides, and sulfides of different composition and structures, containing thermally unstable or air-sensitive ions. The structural and chemical details of the prepared HEMs are studied by various techniques of X-ray diffraction (XRD), inductively coupled plasma optical emission spectroscopy (ICP-OES), scanning electron microscopy (SEM), transmission electron microscopy (TEM), Mössbauer spectroscopy and X-ray photoelectron spectroscopy (XPS). By this facile one-step synthesis, a series of HEMs were designed, prepared and investigated as electrode materials for LIBs and electrocatalysts for oxygen evolution reaction (OER) and hydrogen evolution reaction (HER). These HEMs, particularly high entropy sulfides, showed exceptional capabilities in rechargeable batteries and water electrolysis, highlighting the potential and capacity of customized HEMs for various future applications.

Zusammenfassung

Aufgrund des signifikant wachsenden Verbrauchs fossiler Brennstoffe, und der damit zusammenhängenden Umweltprobleme, gewinnen neue nachhaltige Energiequellen und innovative Energiespeicherlösungen in der heutigen Gesellschaft an Bedeutung. Wasserstoff wird als vielversprechende, saubere und erneuerbare Energiequelle betrachtet, jedoch bleibt die effiziente Produktion zur Deckung des Bedarfs eine Herausforderung. Die elektrokatalytische Wasserspaltung ist ein vielversprechender Weg, jedoch erfordert ihre praktische Umsetzung die Entwicklung stabiler, kostengünstiger und hochaktiver Katalysatoren. Neben der Produktion von sauberen Energieerzeugern wie Wasserstoff besteht auch eine hohe Nachfrage nach Energiespeichersystemen, z.B. Lithium-Ionen-Batterien (LIBs), damit die von erneuerbaren Energieträgern erzeugte Energie effizient verwendet werden kann. Unter den verschiedenen Komponenten dieser LIBs ist das Elektrodenmaterial ein entscheidender Bestandteil, der die Leistung und Kosten von wiederaufladbaren Batterien maßgeblich beeinflusst. Materialien werden in allen Energietechnologien benötigt. Daher ist es entscheidend, neue Materialien für die Energieumwandlung und -speicherung, wie Katalysatoren und Elektrodenmaterialien, zu erforschen und deren Zusammensetzungs-Struktur-Eigenschafts-Beziehungen für weitere Fortschritte zu untersuchen.

In den letzten Jahren haben sich Hochentropie-Materialien (HEMs) als vielversprechende Materialklasse für verschiedene Anwendungen herauskristallisiert, aufgrund ihrer einzigartigen strukturellen Merkmale, anpassbaren chemischen Zusammensetzung und resultierenden einstellbaren funktionellen Eigenschaften. Die Anwendung des Hochentropie-Konzepts im Bereich der erneuerbaren Energien bietet auch die Möglichkeit der Synthese neuartiger Materialien, welche mit besonderen Eigenschaften hocheffizient die entsprechenden Anwendungen erfüllen können.

In dieser Dissertation wurde eine neuartige mechanochemische Methode erfolgreich angewendet, um HEMs zu synthetisieren, einschließlich Hochentropie-Oxide, Oxyfluoride und Sulfide unterschiedlicher Zusammensetzung und Struktur, die auch thermisch instabile oder sonst luftempfindliche Ionen enthalten. Die strukturellen und chemischen Details der hergestellten HEMs wurden mit verschiedenen Techniken wie Röntgenbeugung (XRD), induktiv gekoppelte plasmaoptische Emissionsspektroskopie (ICP-OES), Rasterelektronenmikroskopie (SEM), Transmissionselektronenmikroskopie (TEM), Mössbauer-Spektroskopie und Röntgen-Photoelektronenspektroskopie (XPS) untersucht. Mit dieser einfachen Ein-Schritt-Synthese wurden eine Reihe von HEMs entworfen, hergestellt und als Elektrodenmaterialien für LIBs und als Elektrokatalysatoren für die Sauerstoffentwicklung (OER) und Wasserstoffentwicklung (HER) untersucht. Insbesondere Hochentropie-Sulfide zeigten außergewöhnliche Fähigkeiten in wiederaufladbaren Batterien und der Wasserelektrolyse, was das Potenzial und die Kapazität maßgeschneiderter HEMs für verschiedene zukünftige Anwendungen unterstreicht.

Contents

Chapter 1

1. Introduction

Since the beginning of civilization, people have been striving to discover sources of energy to provide a comfortable and convenient lifestyle. In the 21st century, energy has become one of the critical areas in terms of technological development, however, with the development of the world economy since the Industrial Revolution, fossil fuels have become increasingly depleted. This depletion, along with the escalating environmental crisis and the geopolitical implications of energy dependence, has created an urgent need to explore and adopt more efficient, pollution-free, convenient, and safe energy sources.[1]

Clean energy sources, such as solar energy, wind energy, geothermal energy, and hydropower, have received widespread attention in the world today. Many clean energy sources are also renewable energy sources, which are available in various countries, but their potential is far from being fully utilized. In the rapid rise of renewable energy, one of the biggest challenges is the balancing of the power grid during supply and demand fluctuations. Battery storage systems can effectively store and release intermittent renewable energy as needed, and they are one of the indispensable components of future renewable energy systems.[2]

In order to develop efficient energy conversion and storage technologies, researchers have been actively exploring material optimization and innovation. In recent years, a new class of materials known as high entropy materials (HEMs) has shown great potential for energy applications, such as rechargeable batteries, supercapacitors, energy catalysis and conversion.[3] The high entropy concept allows for the incorporation of multiple elements in equimolar or non-equimolar ratios, resulting in an almost infinite number of possible combinations. This exceptional flexibility enables tailoring of material properties, such as enhanced stability, improved conductivity, and optimized catalytic performance. Furthermore, the cocktail effects arising from the interaction of multiple elements within the HEMs offer synergistic advantages, leading to enhanced energy conversion and storage capabilities. These distinctive attributes make HEMs a captivating area of research, holding immense potential for promoting the development of energy technologies.

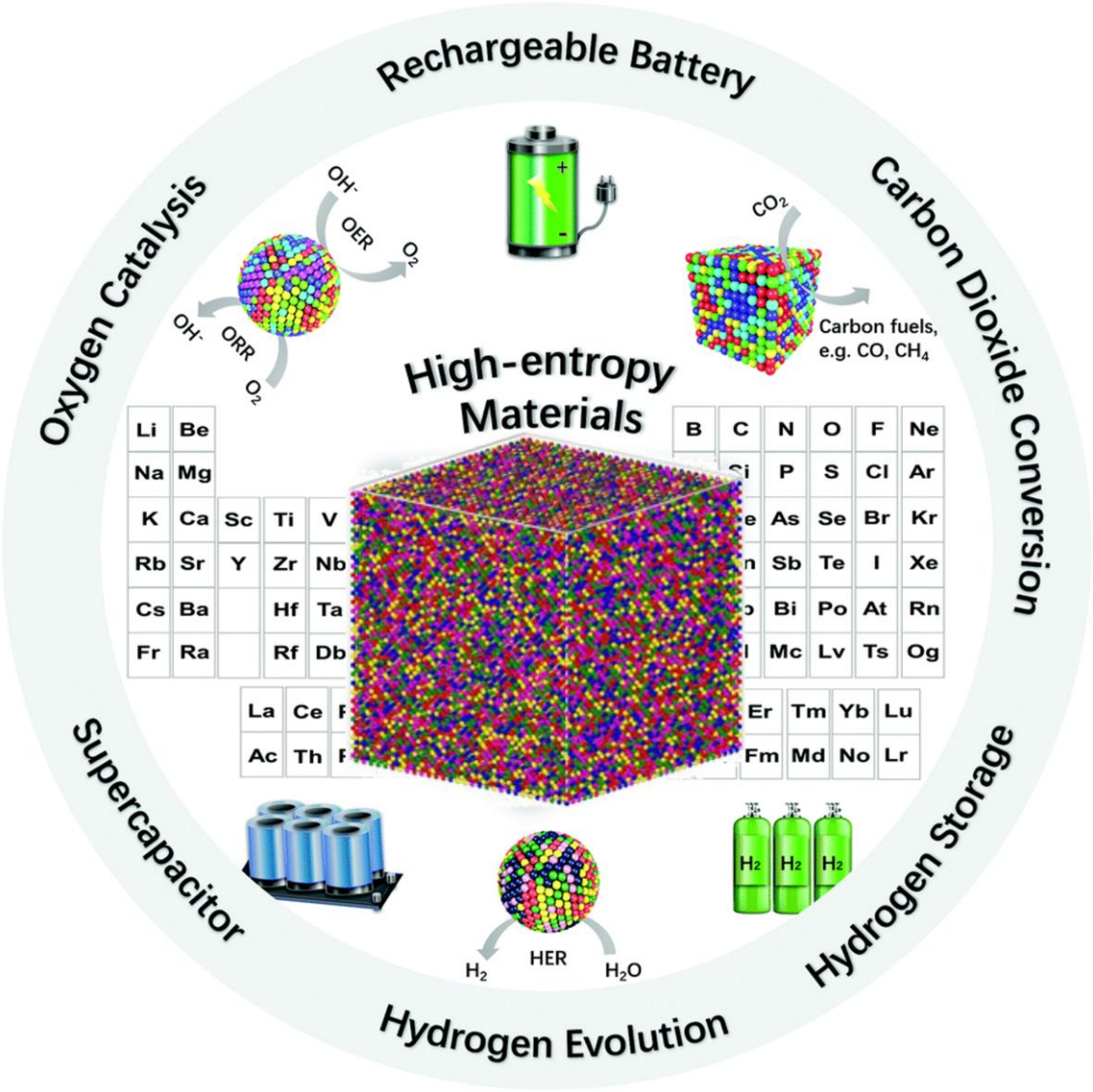

Figure 1.1: The applications of HEMs in energy storage and conversion.[3]

This dissertation deals with the development of a fabrication method, an adapted mechanochemical synthesis, to produce novel and innovative materials such as high entropy sulfides, oxides and oxyfluorides. These materials are thoroughly characterized and applied as active materials in rechargeable batteries and hydrogen (or oxygen) production by water splitting electrocatalysis.

This thesis is divided in different chapters that guide through the work performed during this dissertation. In Chapter 1 the topic is introduced. Chapter 2 provides an overview of the basic principles, electrode materials, development of Li-ion battery, as well as the fundamental principles and catalysts involved in water splitting electrocatalysis. Additionally, it covers the background, concept and theory of HEMs.

Chapter 3 introduces the fundamentals of various characterization techniques and relevant experimental details. The basic characterization techniques include X-ray diffraction (XRD), inductively coupled plasma optical emission spectroscopy (ICP-OES), scanning electron microscopy (SEM), transmission electron microscopy (TEM), Mössbauer spectroscopy and X-ray photoelectron spectroscopy (XPS). In addition, the experimental

details of battery fabrication and measurement, electrocatalytic preparation and testing, the synthesis methods involved are also introduced.

Chapter 4 describes the development of a mechanochemical route to synthesize high entropy oxides, oxyfluorides and sulfides. This synthesis method is explored for the incorporation of various elements, particularly redox-sensitive ions, and to obtain different elemental compositions in HEMs. As-prepared HEMs are thoroughly characterized via XRD, ICP-OES, TEM, XPS and Mössbauer spectroscopy.

Chapters 5-7 discuss the HEMs that were prepared for energy applications. Chapter 5 presents the HEMs as electrode materials in Li-ion batteries, while Chapter 6 investigates the prepared HEMs as catalysts for the oxygen evolution reaction and Chapter 7 studies the prepared HEMs as catalysts for the hydrogen evolution reaction.

Chapter 8 discuss the conclusions derived from this dissertation and provides an outlook for future research.

Chapter 2

2. Fundamentals

This chapter briefly presents an introduction of Li-ion rechargeable batteries, provides an overview of water splitting electrocatalysis, and explains the background of high entropy materials

2.1. Lithium-ion Batteries (LIBs)

The development of lithium-ion batteries (LIBs) has led to their widespread use in almost all fields of our daily lives, such as portable electronics, electric vehicles, and grid energy storage systems. As rechargeable batteries, LIBs have many advantages such as high energy density, wide operating temperature range and long cycle life.[1] LIBs currently stand as the market leader in the field of rechargeable batteries, consequently attracting widespread attention. This section briefly introduces the components, working principle and electrode materials of LIBs.

2.1.1. Components and Working Principle of LIBs

As a type of rechargeable battery, LIBs typically consist of an anode electrode, a separator, an electrolyte, a cathode electrode, two current collectors and a housing.[4] During discharge, the anode and cathode correspond to the negative and positive electrodes, respectively, and are commonly referred to as such. The separator is a membrane typically made of electrically insulating material, such as polypropylene, whose role is the prevention of an electrical short circuit caused by direct contact between the electrodes while allowing for Li-ion diffusion. The electrolyte in lithium-ion batteries typically consists of a lithium salt (such as $LiPF_6$ and $LiClO_4$) dissolved in an organic solvent mixture that exhibits high electrochemical stability throughout the operating voltage range, such as ethylene carbonate (EC), dimethyl carbonate (DMC), diethyl carbonate (DEC), or ethyl methyl carbonate (EMC).[5] Figure 2.1 shows the interior structures of the four commonly used commercial LIBs, including coin,

cylindrical, prismatic, and pouch.[6]

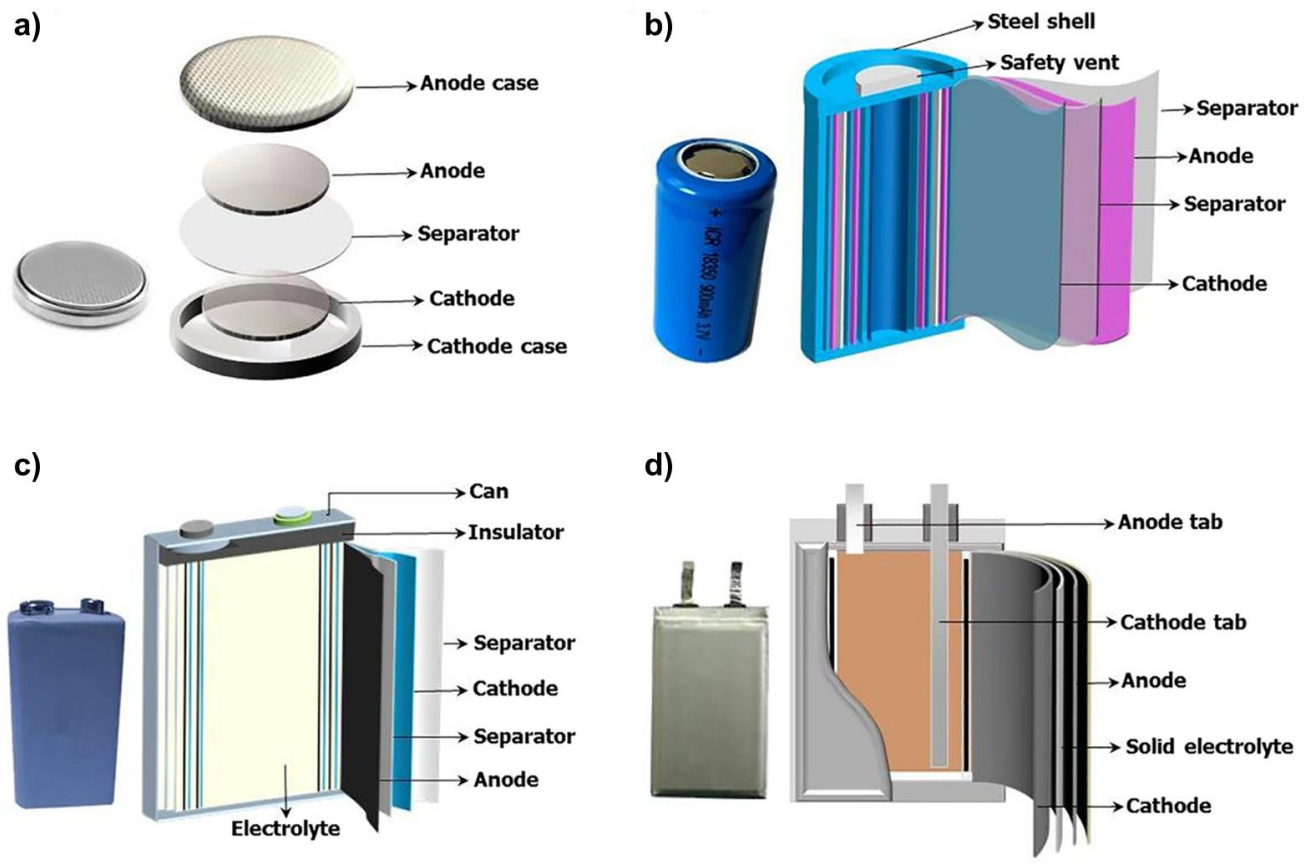

Figure 2.1: Four types of typical LIBs configurations: (a) coin, (b) cylindrical, (c) prismatic and (d) pouch models.[6]

LIBs are a type of swing battery or rocking chair battery, as lithium ions move back and forth between the anode and cathode through the electrolyte during charging and discharging. During this process, conversion occurs between chemical energy and electrical energy, which enables the storage and utilization of electrical energy. For example, in a $Li_xC_6/Li_{1-x}CoO_2$ lithium-ion cell (Figure 2.2),[7] lithium ions diffuse from the cathode ($LiCoO_2$) into the anode (graphite, C_6) with oxidation of the cathode and reduction of the anode during the charge process. During the discharge process, the anode (a lithiated graphite structure, Li_xC_6) releases lithium ions that diffuse into the cathode (a delithiated $Li_{1-x}CoO_2$ structure) causing oxidation of the anode and reduction of the cathode.

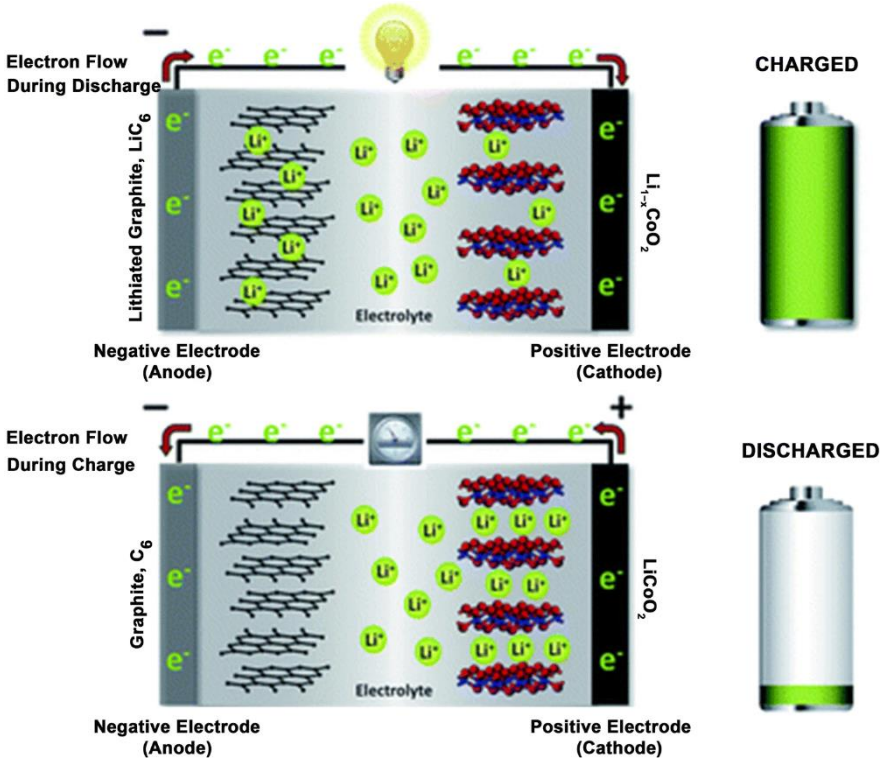

Figure 2.2: The working principle of LIBs based on the $Li_xC_6/Li_{1-x}CoO_2$ lithium-ion cell.[7]

2.1.2. Electrode Materials for LIBs

The performance of the electrode materials directly affects the performance of the entire battery system.

In commercial LIBs, the anode is typically made of graphite-based materials because of the low cost, high availability of carbon, and the stability of graphite for lithium intercalation.[4] However, the amount of lithium that can be accommodated in graphite is relatively limited, with a theoretical capacity of 372 mAh g^{-1}.[8] In recent years, researchers have made considerable efforts to optimize graphite-based anode materials and also to develop new anode materials, such as silicon, alloys and metal ceramics.[9–11]

The cathode, which serves as a lithium-ion donor, is typically composed of complex lithiated compounds, such as $LiFePO_4$ (LFP), $LiCoO_2$ (LCO), $LiMn_2O_4$ (LMO), $LiNi_{1/3}Mn_{1/3}Co_{1/3}O_2$ (NMC-111 or NMC), and $LiNi_{0.8}Co_{0.15}Al_{0.05}O_2$ (NCA).[5] These compounds exhibit high impedance compared to metallic lithium due to their low diffusion coefficients and ionic conductivities, leading to reduced energy efficiency and battery lifespan. Therefore, before use, the finely powdered active material are usually mixed with conductive material (such as carbon) and binder (such as polyvinylidene fluoride) in a solvent (such as N-methyl-2-pyrrolidone) and subsequently dried.[12]

Based on the primary Li-ion storage mechanism in LIBs, electrode materials can be categorized into insertion type, conversion type, and alloy type, as shown in Figure 2.3.[13]

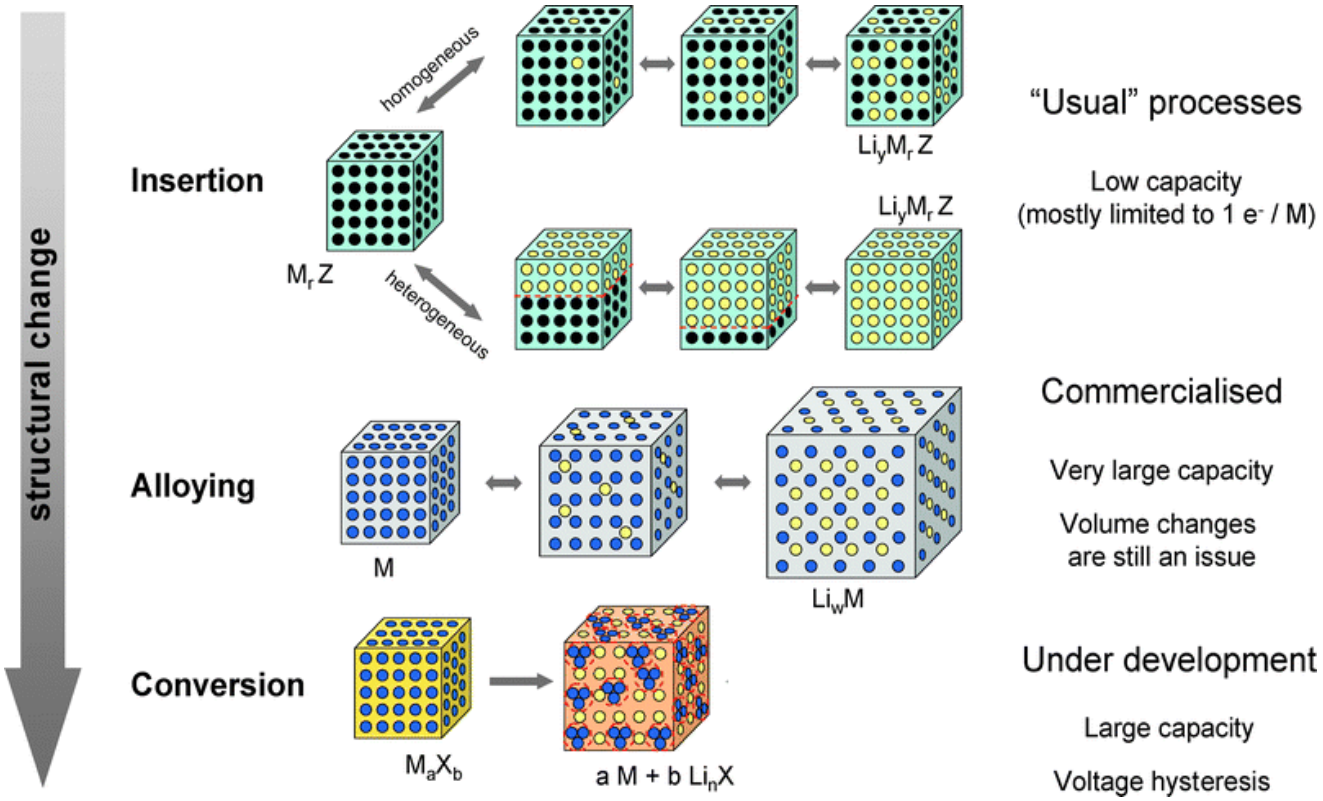

Figure 2.3: Different reaction mechanisms observed in electrode materials for lithium batteries, with voids in the crystal structure represented by black circles, metal by blue circles, and lithium by yellow circles.[13]

Typical insertion electrodes have inherent diffusion pathways of one, two, or three dimensions that facilitate the transport of lithium ions without causing any significant (irreversible) deterioration to the initial crystal structure, and with minimal volume variation.[14] As a result, these electrodes demonstrate high capacity retention and excellent cycle stability, such as LFP and NMC commercial cathode material.

Alloy-type materials (such as Si, Sn, Ge, or Zn) offer high lithium storage capacities by direct bonding between inserted Li-ions and the host element, finally forming composite alloys (such as $Li_{15}Si_4$ or $Li_{4.4}Sn$).[15] However, significant volume changes associated with alloy-type electrode materials can cause the fresh surface to continuously be exposed to the electrolyte, which results in ongoing electrolyte decomposition and the formation of a solid electrolyte interphase (SEI). This limits the cycle life of these electrodes.

Conversion reactions take place when lithium ions are inserted into binary compounds of nanoscale size, represented by MX (where M is a transition metal such as Mn, Fe, Co, Ni, and X is an anion such as O, S, or F). This leads to the reduction of M cations and the formation of M^0 and LiX, resulting in higher capacities than those obtained using insertion-type materials.[16]

2.2. Water Splitting Electrocatalysis

The advancements in energy storage technologies, such as rechargeable batteries, have not only revolutionized the storage and utilization of energy but also played an important role in promoting the development of new energy

sources. Hydrogen, as a highly promising energy source for the future, has garnered significant attention. Producing hydrogen (and oxygen) through electrolysis of water or electrochemical water splitting is widely regarded as a clean, efficient, and sustainable alternative strategy to fossil fuels. Because water is the only starting molecule and by-product in the hydrogen economy cycle, where energy is released by burning hydrogen and water is regenerated.[17] Despite showing promise, this technology still faces technical and economic challenges, such as large overpotential of the catalyst and high cost.[18] This section briefly introduces the principle, mechanism and catalysts used in water splitting electrocatalysis.

2.2.1. Principle of Water Splitting Electrocatalysis

The electrolysis of water was first reported in 1789.[19]. The process is H_2O (l) → H_2 (g) + 1/2 O_2 (g) ($\Delta G°$ = +237.2 kJ mol^{-1}, $\Delta E°$ = 1.23 V vs normal hydrogen electrode), including two half-cell reactions: hydrogen evolution reaction (HER) at cathode and oxygen evolution reaction (OER) at anode (Figure 2.4).[17] In alkaline condition, at the cathode the reaction occurs $2H_2O + 2e^- \rightarrow H_2 + 2OH^-$, and at the anode the reaction occurs $4OH^- \rightarrow O_2 + 2H_2O + 4e^-$. In acidic condition, at the cathode the reaction occurs $2H^+ + 2e- \rightarrow H_2$, and at the anode the reaction occurs $2H_2O \rightarrow O_2 + 4H^+ + 4e^-$.[20] In a practical operation, generating hydrogen or oxygen from water using electrochemical processes generally demands a greater energy input or higher potential to overcome the energy barriers, compared to the minimum thermodynamic energy required for the reaction.

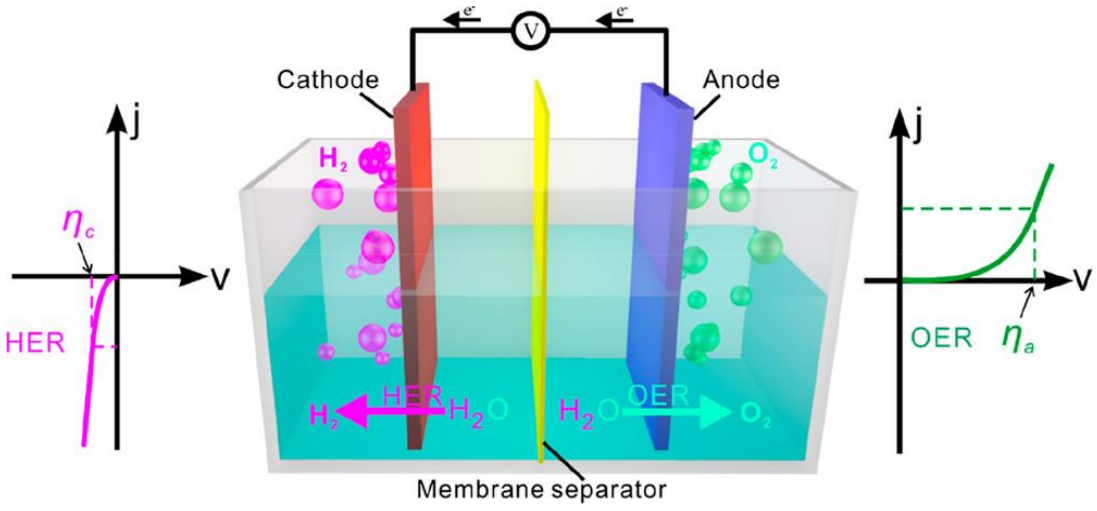

Figure 2.4: Schematic illustration of electrocatalytic water splitting (HER and OER).[17]

In practical applications, producing hydrogen or oxygen from water in the electrochemical process requires a higher potential (more energy input) to overcome the barriers. This additional potential is also known as overpotential (η), mainly attributed to resistance among electrodes, the electrolyte and the catalysts.[20]. Both the HER and OER need appropriate catalysts to minimize overpotentials and thus achieve efficient production of H_2 or O_2. A typical electrolytic cell is composed of the anode, cathode, and electrolyte. And electrocatalysts are usually distributed on the electrodes to achieve high catalytic activity.

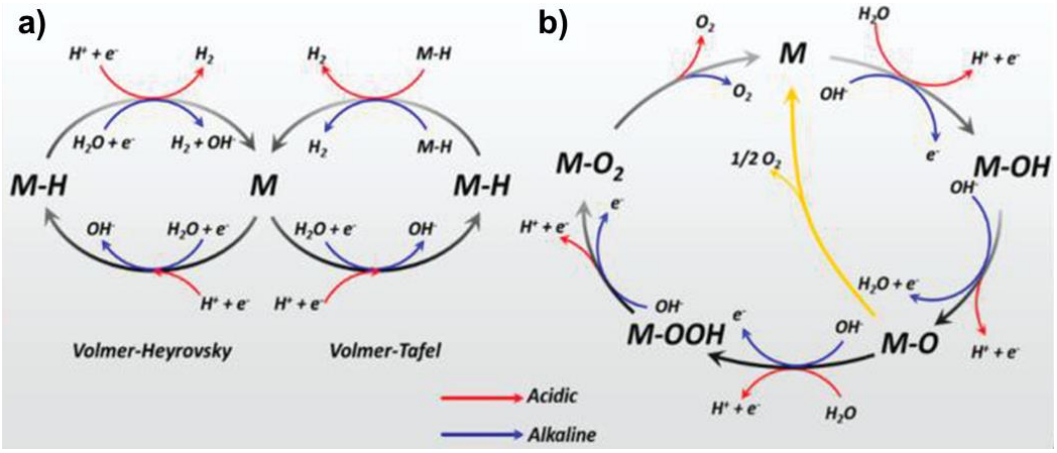

Figure 2.5: General reaction pathways for (a) HER and (b) OER.[20]

The widely accepted reaction pathways for the HER and OER are shown in Figure 2.5.

The electrochemical HER process involves three reaction steps, which can occur in either acidic media for proton reduction or alkaline media for water molecule reduction, leading to the production of hydrogen molecules (H_2) on the electrode surface.[17] As shown in the lower part of Figure 2.5a, the initial step in the electrochemical process of HER involves the Volmer reaction, where a proton combines with an electron to produce an adsorbed hydrogen atom ($H^+ + e^- \rightarrow H_{ads}$) on the surface of the electrode material (M). The protons come from the hydronium cation (H_3O^+) in acidic media or water molecule in alkaline media. In alkaline conditions, HER is slower than in acidic conditions because water dissociation occurs before the formation of H_{ads}.[20] As shown in the upper part of Figure 2.5a, after the formation of H_{ads}, two competing or cooperative reaction steps take place for H_2 evolution. One possible pathway is the Heyrovsky mechanism, where a proton diffuses to the H_{ads} and reacts with a second electron to evolve H_2 ($H_{ads} + H^+ + e^- \rightarrow H_2$). The second pathway, which is the Tafel reaction, is relatively fast. It involves the combination of two H_{ads} in the vicinity on the electrode surface to form H_2 ($H_{ads} + H_{ads} \rightarrow H_2$).[17,21] When there is a relatively low coverage of H_{ads} on the catalyst surface, the dominant reaction pathway is the sequential Volmer and Heyrovsky sequences, as shown on the left side of Figure 2.5a. However, if there is a sufficient coverage of H_{ads} on the catalyst, the faster Volmer-Tafel steps will occur predominantly, as shown in the right pathway in Figure 2.5a.[20]

For OER, various possible mechanisms have been proposed in the literature.[20,22–26] These mechanisms involve complex multi-steps that require relatively large overpotentials to complete the entire reaction. Figure 2.5b provides a brief schematic diagram of OER catalytic mechanism. The commonly accepted mechanisms in acidic conditions involve the oxide path and electrochemical oxide path.[25] In alkaline conditions, the initial step involves the adsorption of a hydroxyl radical (OH^-) on the surface of the electrode material (M), forming M-OH, which is then followed by the reaction of another OH^- with M-OH to produce M-O. The intermediates M-OH and M-O are commonly found in most of the proposed mechanisms. After that, two general reaction mechanisms are proposed for the formation of O_2. One pathway entails the nucleophilic attack of OH^- on M-O to generate an M-OOH intermediate, which is then decomposed into M-O_2, ultimately producing O_2 gas and the free M. Another pathway is the direct combination of two M–O to generate O_2 and free M, as shown by the yellow arrow in Figure

2.5b.[20] The bonding interactions within the intermediates (M-O, M-OH, and M-OOH) play a crucial role in determining the overall electrocatalytic activity.[27]

2.2.2. Catalyst Materials for OER and HER

The reaction of electrochemical water splitting is kinetically sluggish and requires overpotential to overcome the barriers. In order to accelerate reactions (OER and HER) smoothly and without hindrance, efficient catalysts are required.[28]

Currently, industrial-level OER electrocatalysts heavily rely on noble metal catalysts, primarily Ir and Ru based catalysts, especially under acidic conditions. Nevertheless, the low earth abundance, high cost and relatively low stability of noble metal-based OER electrocatalysts significantly impede their commercialization on a large scale.[29] In addition to noble metal-based electrocatalysts, (non-noble) transition metal-based electrocatalysts have also been widely investigated due to their remarkable OER performance. Especially in alkaline conditions, many reported (non-noble) transition metal-based materials are superior to noble metal-based electrocatalysts.[30] Non-noble metals and alloys typically require stabilization through a host material such as carbon materials or saturation with highly electronegative elements, as they couldn't directly survive in harsh alkaline or acidic electrolytes. Low-cost metal oxides and (oxy)hydroxides have been widely studied as candidates for OER electrocatalysts, showing promising performance.[29] In recent years, non-noble metal chalcogenides and phosphides have gained increasing attention due to their significantly improved OER catalytic performance through heteroatom doping.[31,32] While transition metal nitrides have a slightly higher OER overpotential, their unique electronic structure and good corrosion resistance make them highly promising for OER applications.[33] Additionally, stability of non-precious metal-based electrocatalysts in acidic media is a great challenge. Fortunately, recent reports have shown that some non-precious metal-based OER electrocatalysts such as manganese oxide,[34] metal phosphates,[35,36] and borates[37] can catalyze well under neutral and acidic conditions, offering new possibilities for addressing this challenge. Most non-noble metal based OER catalysts, such as oxides, hydroxides, chalcogenides and phosphides, tend to convert to oxyhydroxides species on the surface during the OER process. Because OER operates in a strongly oxidative environment, it involves a large number of strongly oxidizing intermediates such as M-O, M-OH and M-OOH.[38]

Up to date, platinum group metals (PGMs, including Pt, Pd, Ru, Ir, and Rh) and their derivatives (especially commercial carbon-based platinum Pt/C) remain the most efficient electrocatalysts for HER due to their low overpotential and rapid kinetics.[17,28] However, the large-scale application of PGM-based catalysts is limited by the high cost and limited reserves of Pt and other noble metals on earth. A significant portion of research efforts have been shifted towards developing of non-noble metal-based compounds as alternatives, due to their lower cost, higher earth abundance, diversity, accessibility and tunable composition.[17] In particular, significant experimental and theoretical breakthroughs have been made in the design and development of non-noble transition metal-based (Mo, Fe, Co, Ni, W, V, Cu, etc.) HER electrocatalysts. In fact, a large number of studies on transition metal alloys,[39] transition metal oxides,[40] transition metal nitrides,[41] transition metal carbides,[41] transition metal

chalcogenides,[42] transition metal phosphides,[43] and transition metal borides[44] have been reported, some of which have shown activity comparable to benchmark Pt-based materials. Materials based on Mo and W are considered as promising alternatives to noble metals in various non-noble transition metal-based ceramics, and they constitute a significant fraction of non-noble metal catalysts.[17,20]

Over the past few decades, tremendous research efforts have been devoted to the development of non-noble metal-based OER and HER electrocatalysts, leading to significant scientific advances in this field. However, their overall electrocatalytic performance is still relatively inferior to that of noble metal-based materials, and they are not yet ready for large-scale commercialization.[29] Improving the catalytic performance of non-noble metal-based electrocatalysts remains a challenging task.

2.3. High Entropy Materials (HEMs)

High-entropy materials (HEMs), a new class of materials, have experienced rapid growth and increasing popularity in recent years. The high-entropy concept is focused on incorporating numerous elements into a single phase lattice, resulting in a high configurational entropy and creating a distinctive combination of interactions based on the stoichiometry and type of the included elements.[45]

The concept of high-entropy has been initially introduced in alloy systems,[46,47] and later extended to ceramics, such as oxides,[48,49] oxyfluorides,[50,51] borides,[52], carbides,[53] nitrides,[54] fluorides,[55–57] silicides,[58] chalcogenides,[45,59–62] and phosphides.[63,64] This section briefly introduces the background and theory of HEMs, developments in high entropy sulfides for a general overview of this dissertation in the field.

2.3.1. Background and Theory of HEMs

In 2004, the general high-entropy concept was first deployed in high entropy alloys (HEAs) by Yeh et al.[47] and Cantor et al.[46] independently. HEAs can be defined in two primary ways, one related to their composition and the other based on configurational entropy.[65] In a first definition, HEAs are alloys that consist of a minimum of five principal elements with atomic ratio between 5% and 35%, and any minor elements present must have atomic ratio less than 5%.[47,66] A second definition defines HEAs as alloys with the configurational entropy (ΔS_{config}) greater than 1.5R, where the ideal ΔS_{config} for a random solid solution can be generally be expressed as an Equation 2.1 derived from the Boltzmann and Gibbs interpretation of entropy.[3,65,67]

$$\Delta S_{\text{config}} = -R \sum_{i=1}^{N} x_i \ln x_i \qquad (2.1)$$

In this equation, the molar fraction of the i_{th} component is represented by x_i, while R denotes the ideal gas constant. Early reports of high-entropy ceramics (HECs) involved high entropy carbides, nitrides and oxides.[68–70] Later in 2015, the entropy stabilization concept in multicomponent oxide was further discussed.[48] The ΔS_{config} of ceramic materials can be determined using the following equation:[51]

$$\Delta S_{\text{config}} = -R[(\sum_{i=1}^{N} x_i \ln x_i)_{sl1} + (\sum_{j=1}^{M} x_j \ln x_j)_{sl2}] \qquad (2.2)$$

In this equation, sl1 and sl2 denote different sub-lattices within the structure, N and M represent the number of elements in the sub-lattices, x_i and x_j correspond to the molar fraction of the i_{th} and j_{th} component of the respective sublattice, respectively.

The high-entropy concept involves the dependence of ΔS_{config} solely on the number of incorporated elements, resulting in a competitive situation between the additional enthalpy (ΔH_{mix}) required for mixing different elements and the increased entropy (ΔS_{mix}), based on the Gibbs-Helmholtz equation.[71]

$$\Delta G_{\text{mix}} = \Delta H_{\text{mix}} - T\Delta S_{\text{mix}} \qquad (2.3)$$

When the value of $T\Delta S_{mix}$ is larger than ΔH_{mix}, it leads to the entropy stabilization of one crystal structure. As a result of the more negative ΔG_{mix}, the stability of the compound increases with higher ΔS_{config},[3] particularly at a high temperature (T).

There are four core factors that impact the microstructure and properties: the high entropy effect, sluggish diffusion effect, severe lattice distortion effect, and cocktail effects. These factors are first summarized for HEAs by Yeh[66] and they are also applicable to HECs. In detail, these factors include the interference of complex phase formation in thermodynamics due to the high entropy effect, the slowdown of phase transformation in kinetics caused by the sluggish diffusion effect, the alteration of properties to some extent in structure brought by severe lattice distortion, and the enhanced performance beyond what is predicted by the mixture rule in properties due to the cocktail effect.[66] One very important factor on application of HECs is caused by cocktail effect based on elemental composition and elemental interactions. The properties of materials can be customized to meet specific requirements by altering the type or stoichiometry of incorporated elements.[45] In general, HEMs exhibit exciting and unforeseen properties that have a wide range of applications, such as catalysis,[72,73] thermoelectricity,[62,74] and electrochemical energy storage.[51,75]

2.3.2. State of the Art for High Entropy Sulfides

In the huge family of HEMs, high entropy sulfides (HESs) have just been developed within the last 5 years and are still in their infancy. In this dissertation, HESs as the main research material are investigated as electrode materials for batteries and catalysts for OER and HER. Here, the background of HESs materials are introduced.

As of 2022, reported HESs have been applied in fields of water splitting electrocatalysis,[60,76,77] electrocatalytic reduction of carbon dioxide,[78] rechargeable batteries,[45,79] and thermoelectric materials.[62]

A significant portion of HESs publication is focused on the application as electrocatalysts which are most used for electrochemical water splitting. In a first report in 2020,[60], Cui et al. reported the synthesis of a cubic Fm-3m structured HES $(CrMnFeCoNi)_9S_8$ using a pulsed thermal decomposition method. This HES displayed reamarkable catalytic activity for OER. In 2021,[76] Nguyen et al. reported the excellent OER catalytic

performance of pyrite structured HESs ($FeNiCoCrXS_2$, with X = Mn, Cu, Zn, or Al) synthesized via a two-step solvothermal method. In 2022,[77], Lei et al. reported the good catalytic activity and stability of carbon fiber supported high-entropy sulfide (CoZnCdCuMnS@CF) nanoarrays as electrocatalysts for overall water splitting (OER and HER), which were prepared using a mild cation exchange strategy. Later, $FeNiCoMnCuS_2$ was studied as promising OER electrocatalysts by two groups of synthesis methods, one is prepared via metal-organic frameworks precusors reported by Li et al.,[80] another is synthesized through glycerol-assisted self-template reported by Moradi et al..[81] In addition to electrolysis of water, there is also a HES publication related to carbon dioxide electroreduction, such as 2D HES material $(MoWVNbTa)S_2$ reported by Cavin et al. in 2021.[78] These studies highlight the synergistic effect and stability of HESs, demonstrating their potential in various energy conversion applications by excellent catalytic activity and long-term durability, while the concept of high entropy plays a pivotal role in their design and performance.

For energy storage, HESs have also garnered attention as electrode materials in rechargeable battery. The first report is dated from early 2022,[45] which is related to LIBs application and included in the chapter 4 and 5 in this dissertation. HESs with different M:S ratios, such as pyrite MS_2 (M includes Fe, Co, Ni, Mn, Cu, Cr, or Ti) and orthorhombic MS (M includes Fe, Co, Ni, Mn, and Cr), are prepared by a facile one-step ball-milling method and demonstrate remarkable specific capacities and rate capabilities in LIBs. After that, Zhao et al. use the similar synthesis method to obtain tetragonal-structured material $Cu_4MnFeSnGeS_8$, and report excellent rate capability and cyclability of that HES in sodium-ion battery.[79] These works highlight the advantageous properties of HESs as electrode materials, such as their high specific capacities, improved rate capabilities, and improved cyclability. The concept of high entropy enables the design and utilization of diverse compositions for creating innovative electrode materials that exhibit enhanced electrochemical performance, thus contributing to the advancement of energy storage technologies.

Apart from the conventional high temperature approach and the preparation techniques mentioned above, there are also researchers who make efforts to explore novel synthesis methods for HESs. In 2021,[61] McCormick et al. report a simultaneous multication exchange as an alternative low-temperature pathway to colloidal nanoparticles of the wurtzite-type HES $Zn_{0.25}Co_{0.22}Cu_{0.28}In_{0.16}Ga_{0.11}S$.

The work in this dissertation begins by exploring the appropriate method for synthesizing HEMs that contain thermally unstable or air-sensitive ions. By employing a straightforward mechanochemical approach in an inert atmosphere, single-phase high entropy oxides and oxyfluorides incorporating these unstable ions were successfully synthesized. Then this approach was applied to explore the preparation of single-phase HESs with different elemental compositions. Various novel HESs were designed for application of energy storage or conversion, and successfully synthesized. The exceptional capabilities demonstrated by HESs as electrodes for LIBs, as well as electrocatalysts for OER and HER, serve as compelling illustrations of the potential and capacity of customized HESs for many future applications.

Chapter 3

3. Experimental

This chapter provides a concise introduction to the materials characterization methods and experimental processes employed throughout this dissertation. It delves into the experimental procedures utilized for determining the properties of the synthesized materials, with a particular emphasis on assessing their catalytic and battery performance. It is important to note that, unless explicitly specified otherwise, all experiments documented in this dissertation were personally conducted by the author.

3.1. Fundamentals and Measurements

This section provides a summary of various characterization methods employed to study the samples. It covers X-ray diffraction (XRD), inductively coupled plasma optical emission spectroscopy (ICP-OES), scanning electron microscopy, scanning electron microscopy (SEM), transmission electron microscopy (TEM), Mössbauer spectroscopy and X-ray photoelectron spectroscopy (XPS).

3.1.1. X-ray Diffraction (XRD)

X-ray diffraction (XRD) is a fast, accurate and efficient technique for non-destructive characterization of crystalline phases of materials. The diffraction pattern, obtained by collecting and processing X-ray diffraction data from the crystal, carries information about the spatial arrangement of atoms within the crystal lattice. The peaks in diffraction pattern are determined by the size, symmetry, shape, and orientation of the unit cell, while the intensity of diffraction is influenced by the atom types and their positions within the unit cell. [82] Through the analysis of these diffraction patterns, qualitative and quantitative relationships between X-ray diffraction and the crystal structure can be established.

The Bragg equation[83] is important for analyzing the diffraction pattern as it uses the principles of diffraction to describe the intrinsic relationship between diffraction and crystal structure. In the equation, $n\lambda = 2d \sin\theta$, n is an integer, λ represents the wavelength of X-rays, d stands for the crystal plane spacing, and θ describes the angle between incident X-rays and corresponding crystal planes. When X-rays are diffracted on parallel planes within the crystal, the path difference between the X-rays is $2d\sin\theta$. Only if the path difference is equal to n times the X-rays wavelength (n = 1, 2, 3…), the diffraction intensity strengthens and constructive interference occurs, which could be detected and appears as a peak in the XRD pattern, allowing d to be calculated. In other cases, waves interfere destructively, resulting in a weaker intensity and contributing to the baseline on the XRD pattern.

XRD patterns were collected on powder samples at room temperature, using STOE Stadi P diffractometer with a Ga-jet X-ray source (Ga-K_β radiation, 1.2079 Å), or Bruker D8 Advance diffractometer with a Cu-K_α radiation source (λ = 1.5406 Å). Diffraction patterns were obtained by scanning between 2θ = 10° and 90° with a step size of 0.1°. The scanning rate used was 4 s per step. Refinement of the XRD pattern was performed using TOPAS Academics V5 software. Si served as a calibration sample to determine the instrumental resolution. Background refinement was done using a linear interpolation function comprising 36 parameters. Rietveld refinements were performed by Dr. Simon Schweidler (KIT).

3.1.2. Inductively Coupled Plasma Optical Emission Spectroscopy (ICP-OES)

Inductively Coupled Plasma Optical Emission Spectroscopy (ICP-OES) is a common technique to analyze the elemental stoichiometry of samples. Usually samples dissolved in acid solution are nebulized and transported into a plasma environment. Within the plasma, the atoms of the elements undergo excitation, wherein their electrons are promoted to higher energy levels. Subsequent relaxation of these excited electrons to their ground state results in the emission of light, which can be detected and measured using an optical spectrometer. Each element shows own characteristic wavelengths, enabling the identification and quantification of different elements present in the sample.[84]

In chapter 4 and 6, samples were dissolved in aqua regia (HCl: HNO_3 = 3:1) and analysed by performing a double determination using a ARCOS ICP-OES (Spectro Analytical Instruments, Kleve, Germany) with axial plasma view. ICP-OES was measured and analysed by Dr. Guruprakash Karkera (HIU).

3.1.3. Electron Microscopy

Electron microscopy is a distinct imaging technique that differs from optical microscopy. Electron microscopy replaces the use of light beams and optical lenses with electron beams of much shorter wavelengths and electromagnetic lenses based on the principles of electron optics, enabling the visualization of fine structures of substances at a significantly higher magnification and resolution. Nowadays, electron microscopy has become an important method to study the microstructure and morphology of samples. Scanning electron microscopy (SEM) and transmission electron microscopy (TEM) are used in this dissertation.

SEM as microscopy technique can be combined with energy dispersive X-ray spectroscopy (EDX) for chemical composition analysis. In SEM, the focused electron beams are controlled by the scanning coils to scan the sample, and interact with the sample to produce various signals, among which secondary electrons (SEs) and backscattered electrons (BSEs) are the main signals for SEM. SEs originate from inelastic interactions between the primary electron beam and samples. Only SEs from within a few nanometer of the surface can escape and are mainly detected for topographic contrast. BSEs arise from the elastic scattering of the primary electron beam within larger depth regions of the sample, contributing to compositional and imaging analysis in SEM.[85,86]

In a TEM system, highly accelerated and focused electron beams are projected onto thin samples. The interaction between the electron beams and sample atoms results in electron scattering, generating electron or energy signals that carry characteristic information about the samples. Subsequently, these signals are amplified and projected onto an electronic image device for visualization and analysis. The sample has to be thin (preferably below 100 nm), so that sufficient electrons can be transmitted and collected.[87] Different from normal TEM that collects parallel electron beams to get images, scanning transmission electron microscopy (STEM) focuses the electron beams into tiny beam spots, and performs point-by-point scanning imaging on thin samples under the precise control of scanning coils.[88] Benefiting from high spatial resolution, the morphology, lattice and atomic images of samples at the nanoscale and atomic level can be directly observed by TEM. Equipped with selected area electron diffraction (SAED), EDX and electron energy loss spectroscopy (EELS) detectors, TEM can possibly be used for analysis of crystal phases, element distributions and oxidation states.

All SEM measurements were performed on a ZEISS Gemini Leo 1530 equipped with an Oxford EDX detector. The powder samples for each SEM experiment were prepared by coating them with Au using a sputter coater (30 s, 30 mA) to improve conductivity. All TEM measurements were conducted by Dr. Kai Wang and Ziming Ding in the group of Prof. Dr. Christian Kübel (KIT). Data of TEM was analyzed by the author with the help of Kai Wang and Ziming Ding. SAED, high resolution TEM (HRTEM) and STEM-EDX were performed on a FEI Titan 80-300 microscopy, equipped with a CEOS image spherical aberration corrector, a high angle angular dark field (HAADF) STEM detector (Fischione model 3000), EDAX SUTW EDX detector and a Tridiem Gatan image filter. The microscopy was conducted at an accelerating voltage of 300 kV. The powder samples were dispersed on a holey carbon-coated gold grid and loaded onto an FEI double tilt holder.

3.1.4. Mössbauer Spectroscopy

Mössbauer spectroscopy can distinguish extremely small changes in the chemical environment and oxidation state of Fe, resulting in a splitting or shift of the peaks in the Mössbauer spectrum. ^{57}Fe Mössbauer spectroscopy was performed using a spectrometer in transmission geometry with a moving source of ^{57}Co in a Rh matrix and a triangular velocity variation. The isomer shift is given relative to bcc-Fe at room temperature. Mössbauer spectroscopy was conducted and analyzed by Dr. Abhishek Sarkar (KIT).

3.1.5. X-ray Photoelectron Spectroscopy (XPS)

X-ray photoelectron spectroscopy (XPS) is a surface analysis method. The sample is irradiated with X-rays, and then the kinetic energy and number of excited electrons escaping from the surface (typically within a few nanometers) of the material are measured using an electron analyzer. XPS can be used for qualitative analysis and semi-quantitative analysis. Generally, the element composition, chemical state and molecular structure of the sample surface can be obtained from the peak position and peak shape of the XPS spectrum, and the element content on the surface can be obtained from the peak intensity.

In chapter 4, XPS spectra were acquired on a K-alpha+ spectrometer (Thermo Fisher Scientific). The monochromatic Al-Kα line was used as X-ray excitation (1486.6 eV). The samples were analyzed using a microfocused, monochromated Al-Kα X-ray source (400 µm spot size). Data acquisition and processing were carried out using the Thermo Avantage software.[89] XPS spectra were fit with one or more Voigt profiles (binding energy uncertainty: ±0.2 eV). The analyzer transmission function, Scofield sensitivity factors,[90] and effective attenuation lengths (EALs) for photoelectrons were applied for quantification. EALs were calculated using the standard TPP-2M formalism.[91] All spectra were referenced to the C 1s peak (C–C, C–H) at 285.0 eV binding energy controlled by means of the photoelectron peaks of metallic Cu, Ag, and Au, respectively. XPS was measured and analyzed by Dr. Raheleh Azmi and Dr. Christian Njel (KIT).

In chapter 7, X-ray photoelectron spectroscopy (XPS) measurements were conducted using a Phoibos 150 spectrometer system (Specs) with monochromatized Al Kα radiation (400 W, 15 kV) and a detection angle of 45°. The pass energies at the analyzer were set to 90 and 30 eV for survey and detail measurements, respectively. To calibrate the binding energy, the C 1s peak of adventitious carbon was used and set to 284.8 eV. Peak fitting was performed using CasaXPS software, with Gaussian-Lorentzian peak shapes and expected values for intensity ratios and spin-orbit-splittings of the S 2p and Mo 3d peak doublets.[92] To account for the contribution of S 2s peaks from different S species in the Mo3d detail spectrum, corresponding peaks were entered. The positions of these S 2s peaks were fixed by assuming a constant distance of 64.4 eV between the S 2p and S 2s peak. The intensities were related to the S 2p peaks, taking into consideration the relative sensitivity factors of the S 2p and S 2s peaks. XPS was measured and analyzed by Dr. Thomas Diemant and Dr. Guruprakash Karkera (HIU).

3.2. Battery Fabrication and Testing Techniques

The slurry for electrodes, containing active material, binder and conductive carbon, was coated on Cu foil (MTI Corporation) by doctor blading (100-200 µm slit size), followed by drying in a vacuum oven at 80 °C overnight. After drying, circular electrodes (13 mm in diameter) were cut from the electrode tape with an areal loading of active material around 0.5-1 mg cm^{-2}. In chapter 5, the active materials for HES cells were obtained by ball-milling (6 h) with 10 wt. % MWCNTs and 90 wt. % as-prepared HES powders. The multi-walled carbon nanotubes (MWCNTs) were purchased from commercial sources. (Sigma Aldrich, >7.5% MWCNT basis, outer diameter 7 to 15 nm, length 0.5 to 10 µm). The slurry of HESs was formed by uniformly mixing 70 wt. % active material, 10

wt. % super C65 carbon black additive (TIMCAL Ltd.), and 10 wt. % sodium carboxymethyl cellulose (Na CMC, average M.W. ~90000, Sigma Aldrich) in water. The slurry of HEOs contained 63 wt. % of as-prepared HEO, 22 wt. % super C65 carbon black, and 15 wt. % polyvinylidene fluoride binder (PVDF, Solef5130, Solvay) dissolved in N-methyl-2-pyrrolidone (NMP, Sigma Aldrich).

All materials were tested in CR2032 type coin cells and assembled inside an Ar-filled glovebox. LP57 (1 M $LiPF_6$ in a 3:7 weight mixture of ethylene carbonate (EC)/ethyl methyl carbonate (EMC), BASF SE), GF/D glass microfiber filter paper of diameter 17 mm (GE Healthcare Life Science, Whatman) and Li metal foil of diameter 13 mm (China Energy Lithium Co., Ltd) were used as the electrolyte, separator and counter electrode, respectively. Cyclic voltammetry (CV) was performed on a Bio-logic VSP-300 potentiostat device at room temperature. The sweep rate was set to 0.1 mV s^{-1} and the range of voltage was 0.1-3.0 V versus Li^+/Li. The galvanostatic rate capability measurements were performed on an Arbin BT 2000 battery test system (Arbin Instruments) and LAND CT3001A battery test system (Wuhan LAND Electronic Co. Ltd) at 25 °C. The calculation of specific capacity was based on mass of the active material.

For operando XRD analysis, customized CR2032 coin cells with Kapton windows (4 mm in diameter) on each side were prepared and measured on both Bio-logic potentiostat and STOE Stadi P diffractometer with a Ga-jet X-ray source. The slurry for electrodes was coated on carbon film. The higher loading of active material (3.5-4 mg cm^{-2}) was applied to get stronger signal of XRD diffraction. Operando XRD measurement was carried out by Bei Zhou (KIT).

3.3. Electrocatalytic Preparation and Testing Techniques

Electrochemical measurements were conducted using a three-electrode setup on a modulated speed rotator (Equilabrium SAS) with a rotating glassy carbon working electrode (area = 0.196 cm^2) at rotation speeds of 1600 rpm.

In chapter 6 for OER measurements, Pt spiral and Ag/AgCl were used as counter and reference electrodes. The solution, dropped on the working electrode, was prepared by mixing 10 mg of the active material in a solution consisting of 100 µL of H_2O, 1800 µL of 2-propanol and 100 µL of Nafion (5 wt. % Nafion in water/1-propanol, VWR international GmbH). The solution was sonicated in an ultrasonic finger/homogenizer (Scientz-IID, Scientz) in an ice water bath for 30 min. Later, 8 µL of the solution was dropped onto the surface of the working electrode and dried, resulting in a catalyst loading of 0.20 mg cm^{-2}. Iridium oxide powder (IrO_2, 99 % Alfa Aesar) was used as reference material. All measurements were conducted in an O_2-saturated electrolyte of 1M KOH (90 %, reagent grade, Sigma Aldrich) at room temperature using a potentiostat (BioLogic GmbH). Linear sweep voltammetry (LSV) was performed at a sweep rate of 5 mV s^{-1} in a potential range from 1.0 to 1.8 V vs. reversible hydrogen electrode (RHE). Tafel slope is calculated from LSV. The measured potentials are referred to the RHE, $E_{RHE} = E_{Ag/AgCl} + 0.059pH + E^{\theta}_{Ag/AgCl\ vs\ RHE}$, where $E^{\theta}_{Ag/AgCl\ vs\ RHE}$ is 0.1976 at 25 °C and the pH of the electrolyte was measured by pH meter. No iR correction was applied. The overpotential $\eta = E_{RHE} - 1.23$. The double-layer capacitance (C_{dl}) was evaluated via CV measurement using five different scan rates of 5, 10, 20, 40 and 60 mV

s^{-1} in a non-Faradaic potential range of 0.877 - 0.977 V vs. RHE. The electrochemical active surface area (ECSA) was calculated based on the equation ECSA = C_{dl}/Cs, with a specific capacitance Cs of 0.04 mF cm^{-2} according to literature.[60,93] Electrochemical impedance spectroscopy (EIS) measurements were carried out at an overpotential of 400 mV in a frequency range from 1 to 100 kHz with an alternating current (AC) amplitude of 10 mV. The durability properties of HESs were compared by chronopotentiometry at current densities of 10, 20, 50 mA cm^{-2}.

In chapter 7 for HER measurements, a graphite rod and Hg/HgO were used as counter and reference electrodes. The solution, dropped on the working electrode, was prepared by mixing 8 mg of the active material and 2 mg carbon black (Super P Conductive, 99+ %, Alfa Aesar) in a solution consisting of 1800 µL of 2-propanol, 100 µL of H_2O and 100 µL of Nafion. The uniform ink was obtained by sonicating in an ice water bath for 30 min in an ultrasonic finger/homogenizer. Subsequently, 16.5 uL of the solution was dropped onto the surface of the working electrode and dried, resulting in a catalyst loading of 0.33 mg cm^{-2}. Platinum on graphitized carbon (Pt/C, 20 wt. % Pt loading, Sigma Aldrich) was used as commercial HER catalyst reference. All measurements were performed in an N_2-saturated 1M KOH electrolyte at room temperature by a potentiostat (BioLogic GmbH). LSV was conducted at the sweep rate of 5 mV s^{-1} in a potential range from 0.1 to –0.6 V vs. RHE. The measured potentials are referred to the RHE, $E_{RHE} = E_{Hg/HgO} + 0.059pH + 0.098$. The pH of the electrolyte was determined by pH meter. No iR correction was applied. The overpotential $\eta = 0 - E_{RHE}$. The ECSA were evaluated by C_{dl} measured by CV curves in a non-Faradaic potential range from 0.282 V to 0.182 V vs. RHE with different scan rates at 5, 10, 20, 40 and 60 mV s^{-1}. The durability of samples were compared by chronopotentiometry at the constant current densities of −10 mA cm^{-2}. The long-term stability of MS2-Mo were performed by 1000, 2000, 5000, 8000, 9000 CV scans between 0.10 and −0.42 V vs. RHE at the scan rate of 100 mV s^{-1}.

3.4. Materials Synthesis

The high entropy materials studied in this dissertation are mainly powders with nanometer or micrometer sized particles. This section presents the synthesis strategies, including mechanochemical synthesis and nebulized spray pyrolysis.

3.4.1. Mechanochemical Synthesis

Ball-milling was employed in this study as the main preparation method, due to process simplicity and modifiable stoichiometric ratio. All raw chemicals were purchased from commercial sources (Sigma Aldrich/Alfa Aesar/abcr GmbH, Purity ≥ 99%) and used without further purification.

For the synthesis of HEOs, divalent metal oxides powders (ZnO, CuO, MnO, FeO, NiO, CoO, MgO) were used. Equimolar ratios of corresponding oxides were mixed and ball milled for 12 h. All Li(HEO)Fs were prepared via 24 h of ball-milling, with 1:1 molar ratio of LiF and corresponding divalent metal oxide powders.

For the synthesis of equimolar metal sulfides, MS2s and 4MS2 were obtained by ball milling over 110 h using corresponding metal sulfide powders (FeS_2, CuS, MnS, Ni_3S_2, CoS_2, TiS_2, MoS_2), Cr metal powder and sulfur

powder in the respective metal to sulfur ratios. MS, MS-Mo, MS-Ti, M2S3 and M3S4 were prepared through ball milling for 60 h by mixing corresponding metal sulfides (FeS, MnS, Ni_3S_2, CoS_2, TiS_2, MoS_2), Cr powder and sulfur powder in the respective metal to sulfur ratios. For the synthesis of M3S2 sample, metal sulfides (FeS, MnS, Ni_3S_2), Cr, Co and sulfur powder were employed in a 60 h ball-milling process.

For the synthesis of non-equimolar metal HESs, HESMo, HESMoMn, HESMoCu and HESCu were obtained by 14 h ball milling using metal sulfide powders (FeS, Ni_3S_2, CoS, TiS_2, MoS_2, MnS, CuS) in the respective metal ratio. Similarly, for the synthesis of HESMoCu-1 and HESMoAg-1 the corresponding metal sulfides powders (FeS, Ni_3S_2, CoS, TiS_2, MoS_2, Cu_2S, Ag_2S) were mixed according to the respective metal ratio.

All products were synthesized in a high-energy planetary ball-milling machine (Retsch PM 100, Retsch GmbH) at 500 rpm using 50 ml WC vials and 5 mm diameter WC balls under argon atmosphere. The weight ratio of balls to materials was 40:1.

3.4.2. Nebulized Spray Pyrolysis (NSP)

Nebulized spray pyrolysis (NSP) is one common synthetic method for HEOs, as it can quickly produce compositionally complex nanocrystalline particles at high yield without any post-synthesis treatment.[94] During NSP, an aqueous precursor solution containing metal salts is nebulized into mist and then transferred to a hot-wall reactor by flowing gas, finally to form the desired crystalline oxides at the elevated temperature.

In chapter 4, (ZnNiCoMnCu)O 5-cation sample for comparison named HEO-5MC NSP was prepared by NSP method. The precursor aqueous solution contains equimolar metal nitrates (cation concentration 0.1 mol L^{-1} in total): ($Co(NO_3)_2 \cdot 6H_2O$, $Cu(NO_3)_2 \cdot 2.5H_2O$, $Mn(NO_3)_2 \cdot 4H_2O$, $Ni(NO_3)_2 \cdot 6H_2O$ and $Zn(NO_3)_2 \cdot 6H_2O$ (All abcr GmbH, purity ≥ 98%). Subsequently, the as-prepared solution was nebulized using ultrasonic generator and transported into hot zone of a tube furnace (1050 °C) through flowing carrier gas of N_2 by pumping. The product was collected using a filter based collector (120 °C). NSP process was operated with the help of Dr. Junbo Wang (KIT).

Chapter 4

4. Mechanochemical synthesis: route to novel high-entropy oxides, oxyfluorides and sulfides

Major parts of this chapter were published in Journal of Materials Science[95] *and Advanced Energy Materials*[45].

4.1. Introduction

In recent years, a large number of studies report on high entropy oxides (HEOs) of different structures incorporating multiple elements. Different crystal structures have been explored: rock-salt-type HEOs, e.g. (CoCuMgNiZn)O,[49] spinel-type HEOs, e.g. $(CoCrFeMnNi)_3O_4$,[96] perovskite-type HEOs, e.g. (GdLaNdSmY)(CoCrFeMnNi)O_3,[97] fluorite-type HEOs, e.g. (CeZrHfSnTi)O_2, to name a few.[98] The HEOs are generally synthesized using high temperature processing or precursors prepared in air/solution, such as hydrothermal (HT), nebulized spray pyrolysis (NSP), reverse co-precipitation (RCP), solution combustion synthesis (SCS) or flame spray pyrolysis (FSP).[49,97,99–103] Thus, these methods are usually not suitable for thermally unstable or air-sensitive ions. For example, NSP could be applied to prepare (CoCuMgNiZn)O with rock salt structure. However, it is difficult to introduce or replace elements because secondary phases are easily formed. If Fe or Mn precursors are introduced in equal ratios to other cations using NSP, it results in the formation of not only the necessary 2+ ions for the rock salt structure but also higher valence species. This leads to the appearance of secondary spinel phases that consist of both 2+ and 3+ ions, while the rock salt structure requires only 2+ ions. To counterbalance the presence of the 3+ ions and prevent the formation of these secondary phases, Li+ ions are often introduced.[104–106] The addition of Li^+ ions serves as a charge compensator by compensating for the higher valence 3+ ions, thereby maintaining the desired rock salt structure and suppressing the formation of undesired secondary spinel phases. This charge compensation mechanism helps stabilize the crystal structure and ensures the desired composition is included.

In this dissertation, a facile mechanochemical synthesis technique was successfully developed to prepare four novel pure phase rock-salt HEOs containing different metals than the already reported compound (CoCuMgNiZn)O in equimolar ratios, two of the systems even comprise 6 and 7 different cations in equimolar composition. This route can also be applied for the synthesis of high entropy oxyfluoride multi-anionic systems (Li(HEO)Fs) in rock-salt structures. Subsequently, the method is transferred to investigate the preparation and the structure of HESs with different metal to sulfur ratios. Without additional ions for charge compensation, all products can be synthesized by a straightforward high-energy ball-milling one-step process at room temperature in an inert atmosphere (Ar). These new HEO, Li(HEO)F and HES were characterized and studied using several characterization. This chapter provides a general and simple approach to synthesize multi-metal high entropy materials with tailored composition for numerous applications, even if thermally unstable or air-sensitive ions are incorporated.

4.2. Rock-salt-structured High Entropy Oxides and Oxyfluorides

This chapter presents the characterization of rock-salt structured HEOs with novel combinations of cations through one-step high-energy ball-milling synthesis process in an inert atmosphere at room temperature. The reactants are divalent metal oxides and used in equimolar ratios. The chosen metal ions (Mg^{2+}, Mn^{2+}, Fe^{2+}, Co^{2+}, Ni^{2+}, Cu^{2+}, Zn^{2+}) have similar radii[107] and finally form 5, 6 and 7-cationic single-phase systems. Four new HEOs, namely (ZnNiCoMnCu)O, (ZnNiCoMnFe)O, (ZnNiCoMnFeCu)O and (ZnNiCoMnFeCuMg)O, are later labeled as: HEO-5MC, HEO-5MF, HEO-6M and HEO-7M, respectively. In addition, four new Li containing high entropy oxyfluorides Li(HEO)F with similar cation composition were obtained by a mechanochemical process reported in literature[51]. The prepared compounds Li(ZnNiCoMnCu)OF, Li(ZnNiCoMnFe)OF, Li(ZnNiCoMnFeCu)OF and Li(ZnNiCoMnFeCuMg)OF are denoted as LiHEOF-5MC, LiHEOF-5MF, LiHEOF-6M and LiHEOF-7M, respectively. The configurational entropy (S_{config}) calculated by Boltzmann's entropy formula (Equation 2.2) is S_{config}(HEO-5MC, HEO-5MF) = 1.61R , S_{config}(HEO-6M) = 1.79R, S_{config}(HEO-7M) = 1.95R, S_{config}(LiHEOF-5MC, LiHEOF-5MF) = 2.19R, S_{config}(LiHEOF-6M) = 2.28R, S_{config}(LiHEOF-7M) = 2.36R, with R being the ideal gas constant. These new HEO and Li(HEO)F are characterized comprehensively using refined XRD, TEM, EDX, Mössbauer spectroscopy and XPS.

4.2.1. XRD

The obtained XRD pattern of different HEO and Li(HEO)F are compared and presented in Figure 4.1a. Despite introducing Mn and Fe, which could lead to secondary phase, these HEO and Li(HEO)F still exhibit phase-pure rock-salt structures. For the further clarification, the material HEO-5MC-NSP with the same composition as HEO-5MC were prepared by the NSP method. The corresponding pattern displays multiphases, which is probably caused by the oxidation of Mn^{2+} and Fe^{2+} during the NSP process. Figure 4.2 shows the phase analysis of the multi-phase HEO-5MC-NSP material.

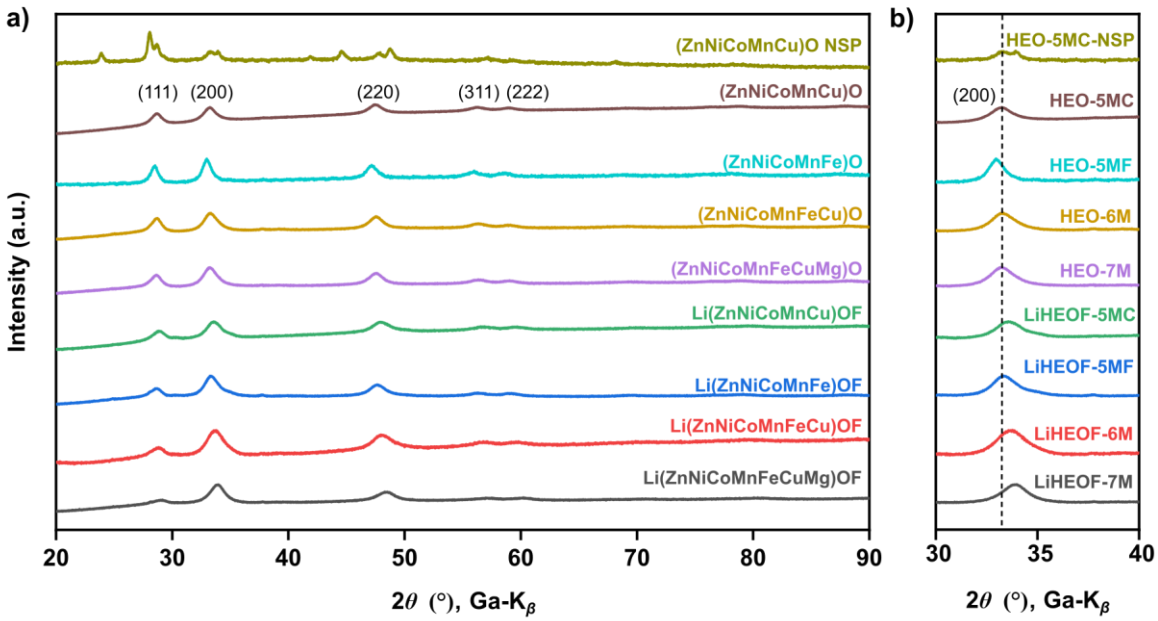

Figure 4.1: (a) Comparison of XRD patterns of as-prepared HEO and Li(HEO)F synthesized by ball-milling and NSP method. While the NSP prepared HEO powder exhibits multiple phases, the ball-milled samples show single-phases. (b) Comparison of the (200) reflection position. The different incorporated ions and lattice parameters result in the shifts.

A magnification of the (200) reflection is provided in Figure 4.1b. Both expansion and reduction of the unit cell size can be observed from the shift of peaks in XRD pattern. The incorporation of the bigger sized ions increases the lattice parameters as seen in the smaller 2θ value, while the incorporation of the smaller sized ions decreases the lattice volume leading to a shift of the peaks to larger 2θ angle. According to the ionic radii of different incorporated ions (assuming high spin configuration, as oxygen regarded as a weak ligand based on the spectrochemical series),[107–109] this shift can be observed in Figure 4.1b. Utilizing HEO-5MC as a reference, it could be found that the substitution of Cu^{2+} (0.73 Å) by Fe^{2+} (0.78 Å) gives rise to an enlargement of the lattice volume and a decrease in the 2θ value (HEO-5MF). The subsequent re-introduction of Cu^{2+} causes a shift to higher 2θ angle (HEO-6M), and the incorporation of the smaller size ion Mg^{2+} (0.72 Å) also leads to larger 2θ value (HEO-7M). Compared to these HEO, Li(HEO)F materials show similar trend and an extra shift, because in anionic sublattice the diameter of F^- (1.33 Å) is smaller than O^{2-} (1.4 Å).

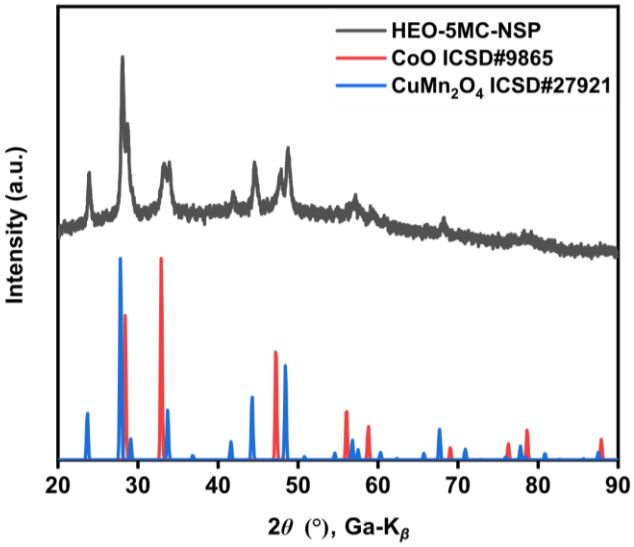

Figure 4.2: Pattern of the multi-phase HEO-5MC obtained by NSP method. During the process, Mn^{2+} is oxidized to Mn^{3+}, forming the $CuMn_2O_4$ compound. CoO is used as a reference for the rock-salt structure.

The lattice parameters and the refinement patterns for all HEO and Li(HEO)F are shown in Figure 4.3 and 4.4. Compared to HEO, the (111) reflections of Li(HEO)F generally exhibit lower intensity, since Li has lower atomic number than other metals.[51] The same trend as described above is clearly shown in the refinement results (Figure 4.3). Compared to HEO-5MC, the replacement of Cu with Fe enlarges the *a*-axis value and lattice volume (HEO-5MF). The re-introduction of Cu to HEO-5MF decreases the volume again (HEO-6M) and the addition of Mg reduces it even more (HEO-7M). Both HEO and Li(HEO)F show the same behavior, while Li(HEO)F exhibits the smaller *a*-axis length and volume of lattice because of small anion F.

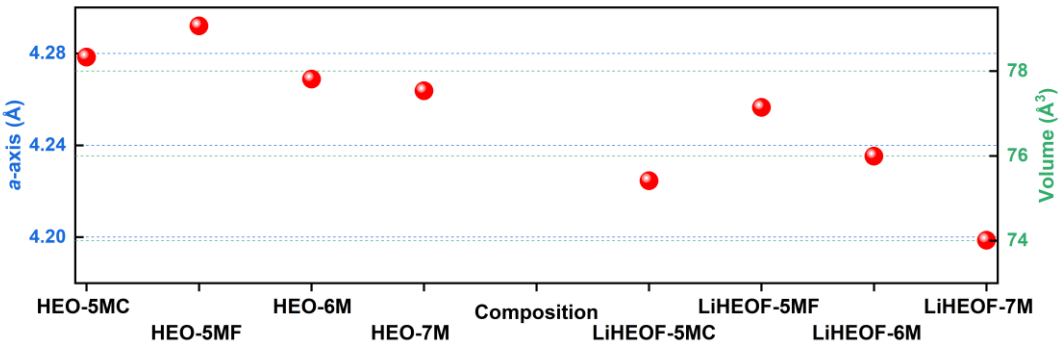

Figure 4.3: Refined *a*-axis length and unit cell volume of the different HEO and Li(HEO)F.

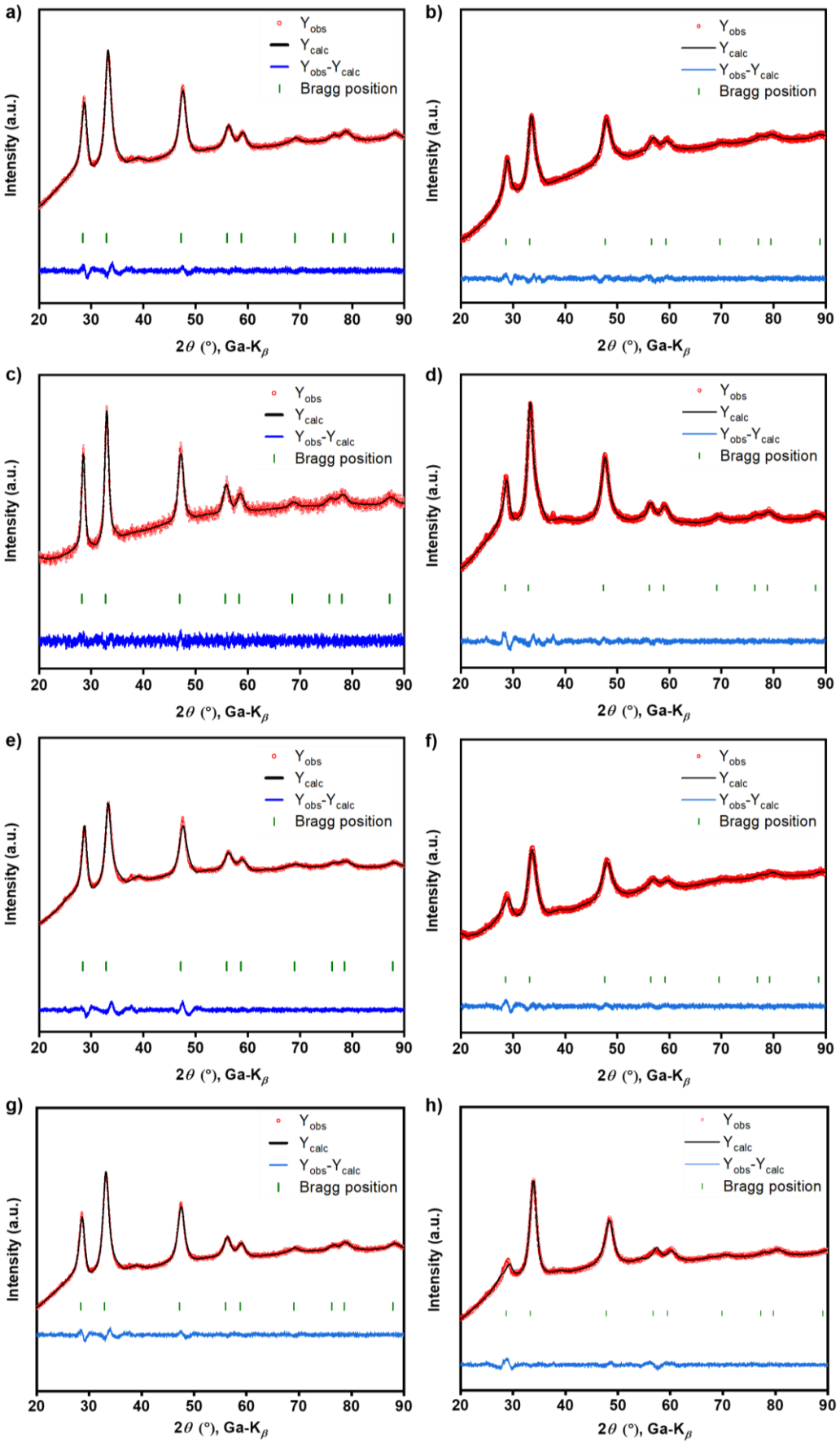

Figure 4.4: Rietveld refinements of (a) HEO-5MC, (b) LiHEOF-5MC, (c) HEO-5MF, (d) LiHEOF-5MF, (e) HEO-6M, (f) LiHEOF-6M, (g) HEO-7M and (h) LiHEOF-7M.

4.2.2. Microstructure

TEM analysis was carried out to further investigate the structural details of the materials. Figure 4.5 shows the morphology of the representative sample HEO-7M and LiHEOF-7M. The sizes of particles show hundreds of nanometers.

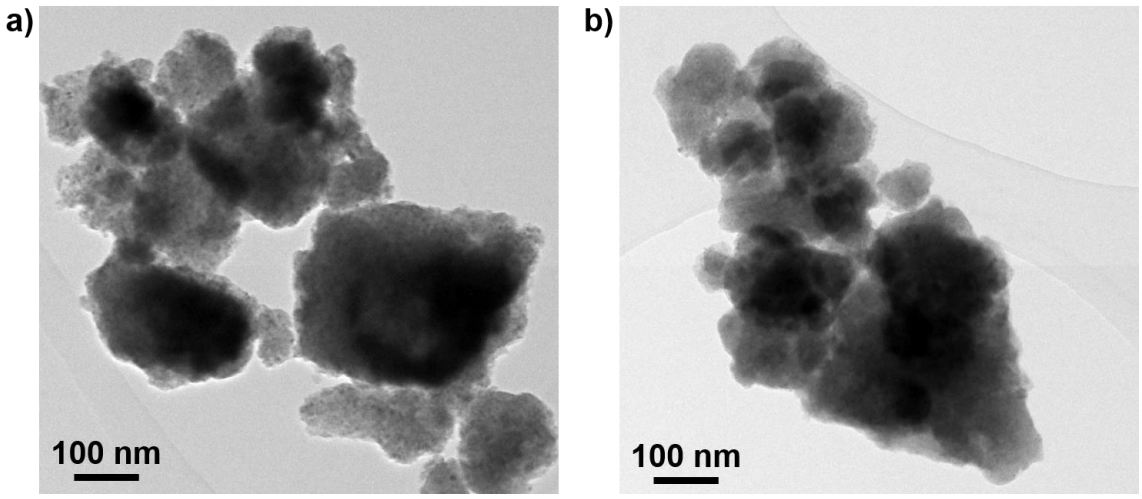

Figure 4.5: TEM images of (a) HEO-7M and (b) LiHEOF-7M.

High resolution TEM (HR-TEM) micrographs of HEO-7M are shown in Figure 4.6, Figure 4.6b being a larger magnification of the area marked by the white square in Figure 4.6a. The red and yellow circles correspond to areas with (111) and (200) lattice planes of the rock-salt structure. SAED is measured to further explore the structure detail of the compounds. In Figure 4.6c, the diffraction rings correspond to the XRD results, giving additional proof of the pure rock-salt phase. The scanning TEM (STEM)-EDX map of HEO-7M (Figure 4.7) shows that all incorporated elements are distributed uniformly, without any sign for aggregation or separation of individual elements. This is an important observation because a homogeneous distribution of all element could contribute to highest possible configurational entropy. In conclusion of the XRD, SAED and EDX results, the as-prepared materials can be regarded as single-phase.

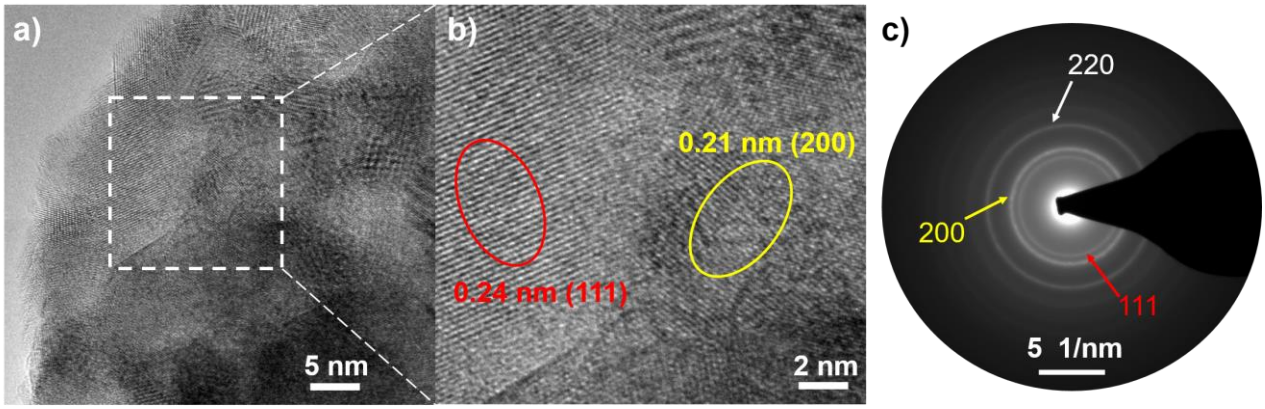

Figure 4.6: (a) HR-TEM of HEO-7M. (b) Magnified TEM image with crystal lattices of HEO-7M. (c) SAED ring taken from HEO-7M. The yellow and red circle refer to the (111) and (200) lattice plane with d-spacing of 0.24 and 0.21 nm, respectively.

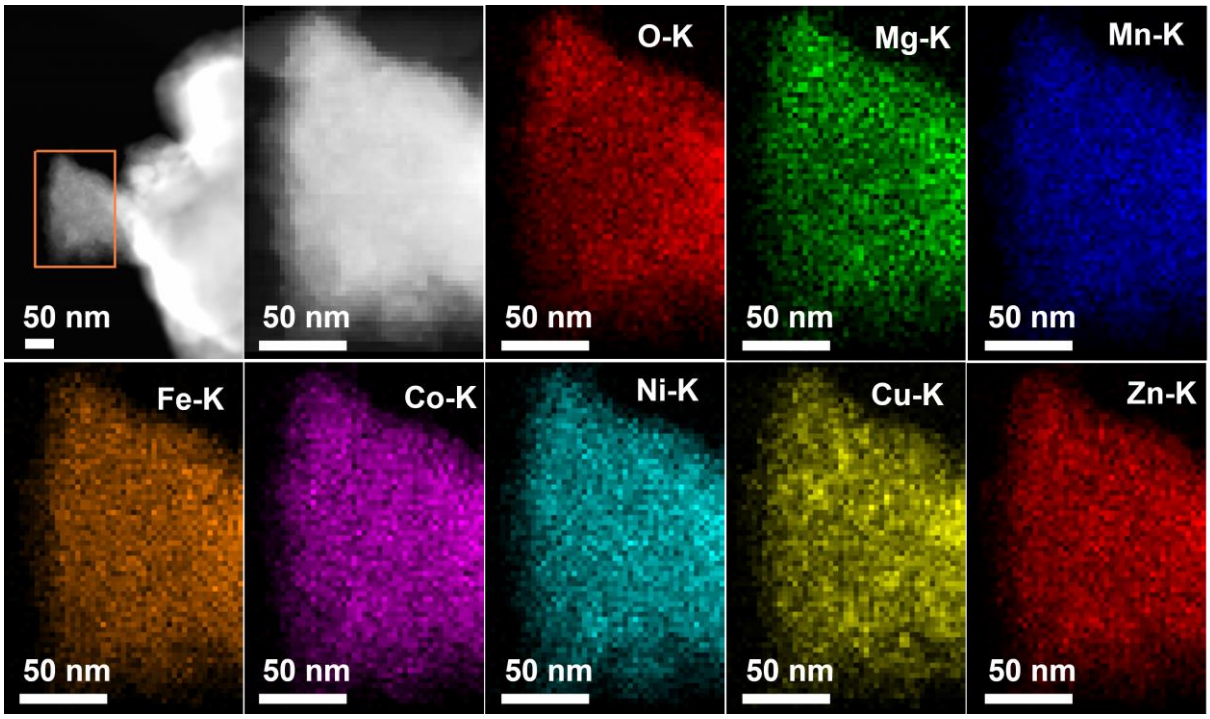

Figure 4.7: STEM-EDX mapping of HEO-7M. All cations and anions are distributed uniformly.

Li(HEO)F was prepared from HEO and LiF by ball-milling, as reported previously.[51] The HR-TEM, SAED and EDX measurements of LiHEOF-7M are shown in Figure 4.8 for comparison. Compared to HEO-7M, the crystallinity of LiHEOF-7M (Figure 4.8a) is greatly reduced, which can be clearly seen from the broader diffraction ring referring to (200) lattice plane in the SAED, noted by the yellow dashed line. The reduction of crystallinity could be attributed to longer ball-milling time for Li(HEO)F. EDX mapping of LiHEOF-7M (Figure 4.8b) still indicates uniform distribution of all elements, including F.

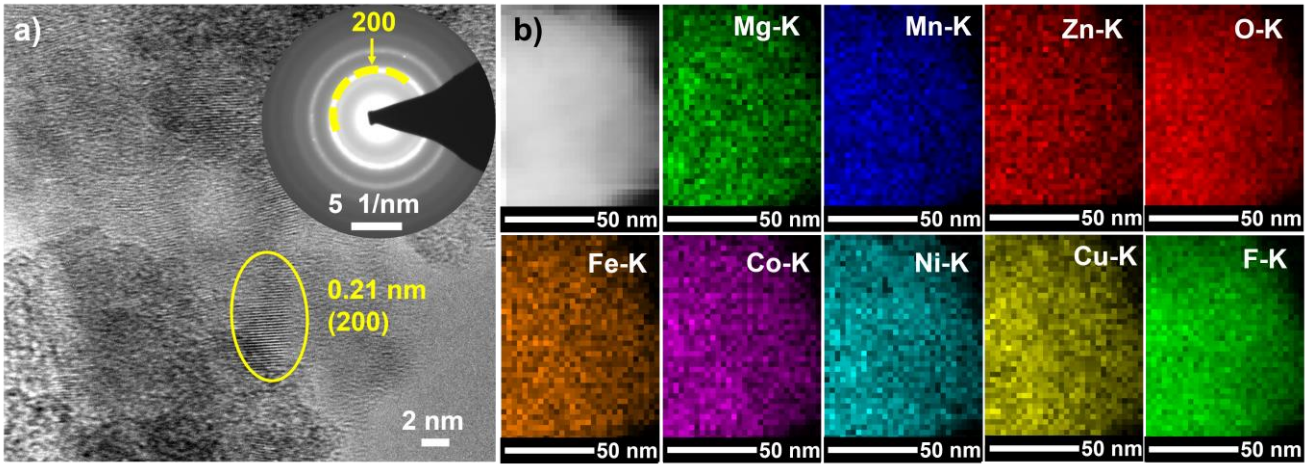

Figure 4.8: TEM investigation of LiHEOF-7M. (a) HR-TEM and SAED ring of LiHEOF-7M. The yellow circle indicates the (200) lattice planes with a spacing of 0.21 nm. (b) STEM-EDX mapping of LiHEOF-7M.

4.2.3. Oxidation State

Mössbauer spectroscopy is known to be extremely sensitive to all local Fe environments, which affect the electronic state of Fe, as indicated by a shift or splitting of peaks. The spectra shown in Figure 4.9 has been fitted assuming only one environment with Fe in 3+ valence state. One doublet spectrum, corresponding to Fe^{3+}, could be fitted with Mössbauer data of HEO-7M. The isomer shift is about 0.35 mm s^{-1} with reference to α-Fe and the quadrupole splitting is 0.79 mm s^{-1}. Generally, the material is paramagnetic at room temperature.[110] The fact that only one environment of Fe^{3+} is found in HEO-7M, gives strong evidence that the Fe ions are distributed homogenously.

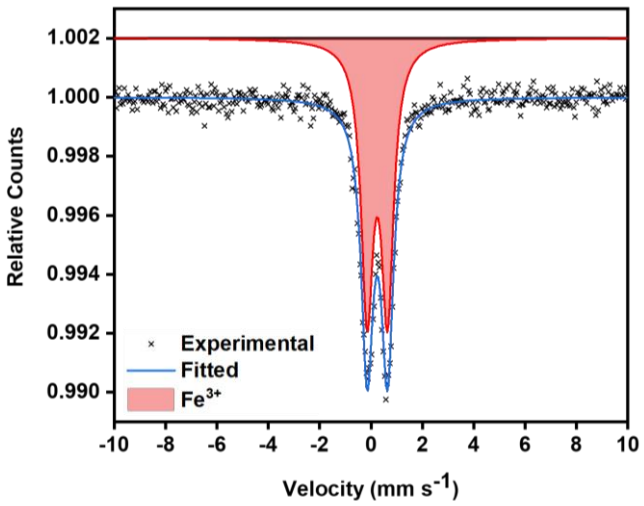

Figure 4.9: Mössbauer spectrum of HEO-7M measured at room temperature. Fe^{3+} ions are uniformly distributed throughout the whole structure.

Considering phase-pure rock-salt HEO produced, the average charge of metal ions in that structure is estimated to 2+, the cation Fe^{3+}, instead of Fe^{2+} from utilized precursor FeO, is not expected. As reported in earlier work,[106] metal cations with higher valences included into a rock-salt structure are prone to form an additional spinel phase. In this case, the charge compensation has to appear to keep the average charge of 2+ in rock-salt structure. It's expected that the charge of another ion changes from 2+ to 1+ or vacancies in the lattice take place, leading to an internal oxidation from Fe^{2+} to Fe^{3+} in HEO-7M. Cu is the most likely element that is suitable for this internal reduction process, as many examples reported that Cu^{+} ion is found to be formed in crystal structure.[111,112] The above Mössbauer results could be explained by the internal disproportionation of Fe^{2+} and Cu^{2+} to Fe^{3+} and Cu^{+}, which is also in agreement with XRD refined data (Figure 4.3). The ionic radii of the incorporated metal ions are particularly close (octahedral coordinated, high spin: Mg^{2+} of 0.72 Å, Fe^{2+} of 0.78 Å, Co^{2+} of 0.75 Å, Ni^{2+} of 0.69 Å, Cu^{2+} of 0.73 Å, Zn^{2+} of 0.74 Å, except Mn^{2+} of 0.83 Å). The ionic radius of Fe^{3+} exhibits smaller value (0.65 Å), while Cu^{+} is not much bigger (0.77 Å). Accordingly, the configuration containing Cu^{2+} and Fe^{2+} is supposed to have a bigger cell size (because of higher average ionic radius) than the configuration containing Fe^{3+} and Cu^{+}.

In comparison with materials including both Cu and Fe, in HEO-5MF and LiHEOF-5MF without Cu, no disproportionation reaction could happen, therefore the unit cell size could not be reduced. Figure 4.3 displays that the unit cells of these materials are exceptional large, which can explain the argument of an internal disproportionation reaction between Fe^{2+} and Cu^{2+}.

For further confirmation, XPS measurement was carried out to analyze the oxidation state of Cu (Figure 4.10). The XPS result of reduced valence for Cu supports the above explanation of an internal disproportionation reaction. The main Cu $2p_{3/2}$ peak lies at 932.8 eV, and a very weak satellite structure appear at 944.2 & 946.8 eV, and Cu LMM peak lies at 916.9 eV, which could be assigned to the Cu^{+} state according to literature.[113] The small Cu $2p_{3/2}$ peak at 934.5 eV could be attributed to minor copper hydroxide forming on surface due to handling in air.

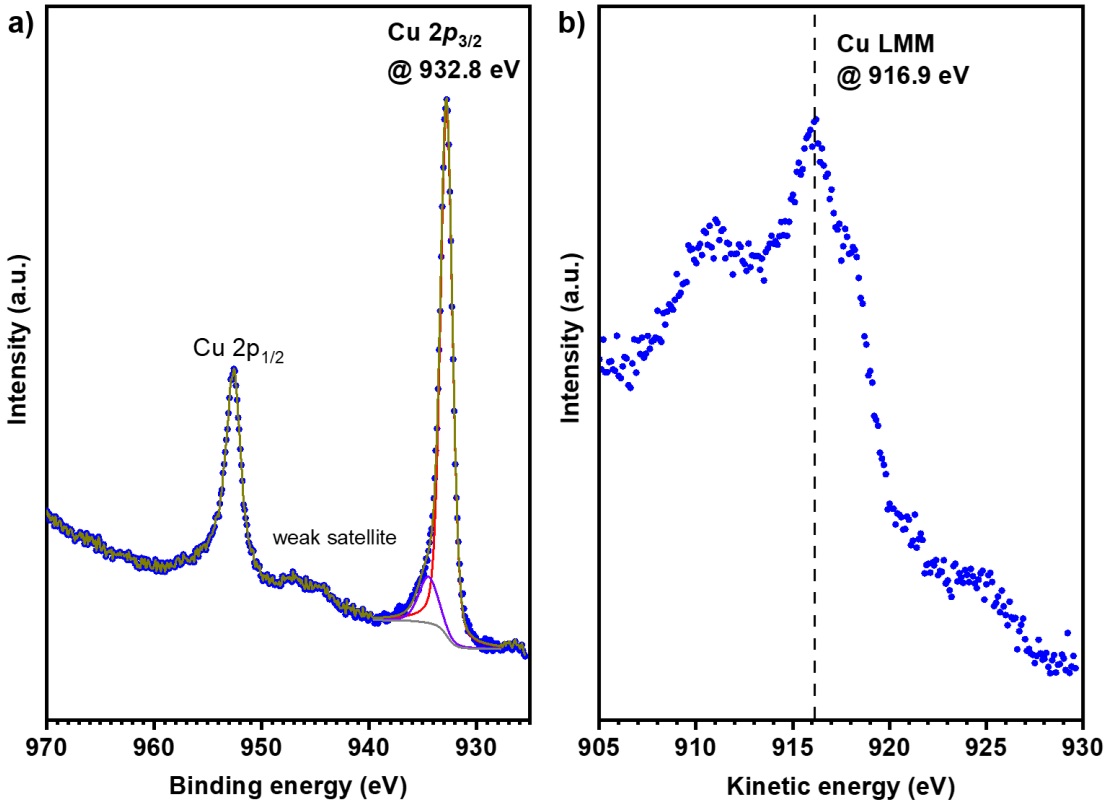

Figure 4.10: XPS spectra of (a) Cu 2p and (b) Cu LMM of HEO-7M

4.3. High Entropy Sulfides with Different Metal to Sulfur Ratio

The successful strategy of incorporating redox-sensitive ions, previously applied in synthesizing HEO and Li(HEO)F, was also employed in the preparation of HES. This chapter explores the influences of different metal-to-sulfur ratios on the structure of the final HESs, using the same one-step high-energy ball-milling process utilized for HEOs. To achieve diverse stoichiometry in the designed compounds, the concentrations of precursor materials, including metal sulfides, metals, and sulfur, were carefully controlled. Two types of single phase HES

structures were successfully synthesized: orthorhombic (*Pnma*) HES1 and pyrite (*Pa*-3) HES2. Table 4.1 summarizes the compositions, structures and abbreviations of the products. The mono-sulfides (FeMnNiCoCr)S and (FeMnNiTiCr)S are labeled as MS and MS-Ti, respectively. The disulfides $(FeMnNiCoCr)S_2$, $(FeMnNiCoCu)S_2$ and $(FeMnNiTiCr)S_2$ are named as MS2, MS2-Cu, MS2-Ti, respectively. Additionally, Sulfides with other metal-to-sulfur ratios, namely $(FeMnNiCoCr)_3S_2$, $(FeMnNiCoCr)_3S_4$ and $(FeMnNiCoCr)_2S_3$, were prepared and marked as M3S2, M3S4, and M2S3, respectively, for comparison. The configurational entropy of all HESs is calculated as 1.61R due to the incorporation of five metals in equimolar proportions. The chosen stoichiometries aim to explore the feasibility of synthesizing HESs with their respective structures, leveraging the existence of known sulfides with similar stoichiometries as references, such as Ni_3S_2 (*R*32),[114] Ni_3S_4 (*Fd*-3*m*),[115] Cr_2S_3 (*R*-3),[116] FeS (*Pnma*),[117] and FeS_2 (*Pa*-3).[118]

These novel HESs were fully characterized by XRD, ICP-OES, TEM, EDX, XPS and Mössbauer spectroscopy.

Table 4.1: Overview about the different prepared samples.

Composition	Structure	Abbreviation
$(FeMnNiCoCr)_3S_2$	Multiphase: *Pnma*, *Fd*-3*m*, $P6_3mc$	M3S2
(FeMnNiTiCr)S	Multiphase: *Pnma*, *Fd*-3*m*, $P6_3mc$	MS-Ti
(FeMnNiCoCr)S	*Pnma*	MS
$(FeMnNiCoCr)_3S_4$	Multiphase: *Pa*-3, *Pnma*	M3S4
$(FeMnNiCoCr)_2S_3$	Multiphase: *Pa*-3, *Pnma*	M2S3
$(FeMnNiCoCr)S_2$	*Pa*-3	MS2
$(FeMnNiCoCu)S_2$	*Pa*-3	MS2-Cu
$(FeMnNiTiCr)S_2$	*Pa*-3	MS2-Ti

4.3.1. XRD

The results of XRD measurements are shown in Figure 4.11. The comparison of XRD patterns indicates that single phase HESs are formed for two types of metal to sulfur ratios (1:1 and 1:2), and shifts of the reflection positions appear based on different incorporated elements.

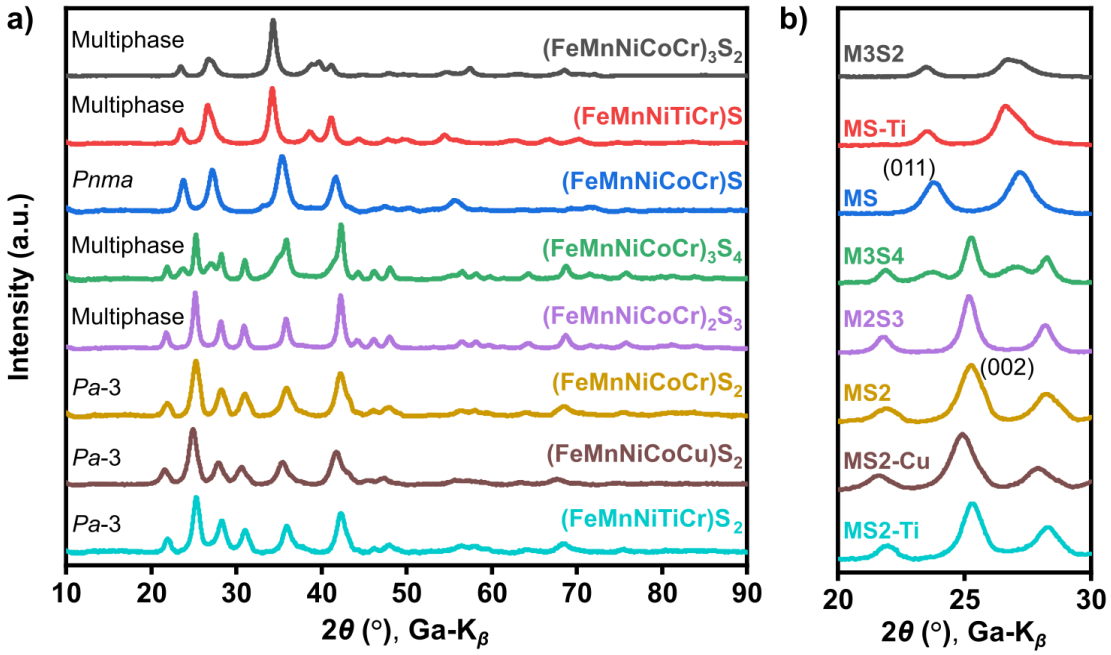

Figure 4.11: (a) Comparison of XRD patterns of as-prepared HESs with different M:S ratios and elemental composition. Transition of HES structure from *Pnma* to *Pa*-3 space group occurs with increasing sulfur content. (b) Comparison of the (002) reflection position of *Pa-3* structured HESs. The shifts can be related to the different sizes of incorporated ions. The data is background corrected.

It is noted that two typical crystal structures occur for as-prepared HESs, but some components include multiple phases. In detail, MS2 and MS seem to be two different single phase, M3S4 and M3S2 are obvious mixtures of different phases. Ni_3S_2 is the only reported M3S2 type in binary components (space group *R*32, ICDD PDF No. 00-044-1418), while M3S4 type exists many different structures for different elements, for example, Cr_3S_4 – *I*2/*m* (ICDD PDF No. 00-011-0008), Ni_3S_4 – *Fd*-3*m* (ICDD PDF No. 00-047-1739), Fe_3S_4 – *R*-3*m* (ICDD PDF No. 01-089-2000) and *Fd*-3*m* (ICDD PDF No. 00-016-0713). Consequently, for M3S2 and M3S4 type in a high entropy version, the mixing enthalpy could be too large to form stable single phase materials. For MS and MS2 type, observed structures of *Pnma* and *Pa*-3 are also the typical phases in corresponding binary components.

Based on different metal to sulfur ratios, the crystal structures of HESs change. The material M3S2 with the highest M:S ratio shows multiphase. As the M:S ratio decreases, the material converts to single phase MS with *Pnma* space group. With further reduction of the M:S ratio, a new phase pyrite structure (*Pa*-3) begins to appear together with Pnma phase, for example M3S4. Further decreasing the M:S ratio, finally only the pure pyrite phase appears, as shown in the MS2s.

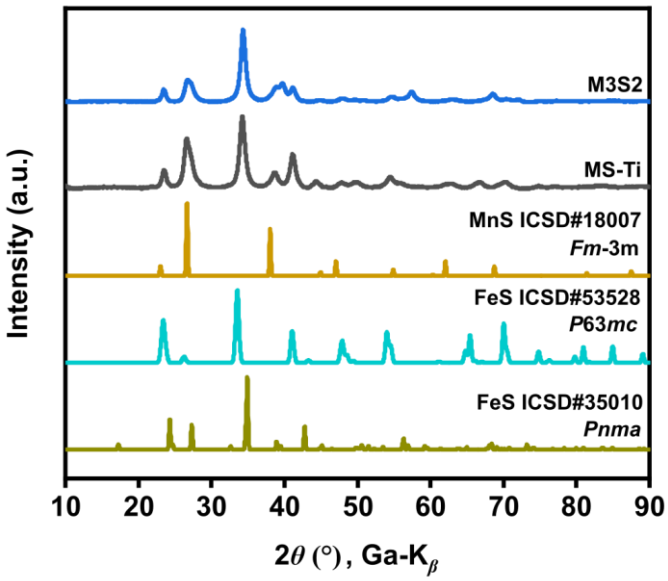

Figure 4.12: XRD patterns of the multi-phase M3S2 and MS-Ti. The data is background corrected.

To investigate the impact of incorporated ions with different sizes or oxidation states on the structure of HESs, certain transition metals in MS and MS2 are replaced. By replacing Co^{2+} (0.745 Å) in MS by Ti^{4+} (0.605 Å),[107] MS-Ti is produced, but it shows multi-phases with *Fm*-3*m*, *P*63*mc* and *Pnma* structures (Figure 4.12). Interestingly, unlike MS compounds, the structure of MS2 seems to be less affected by this replacement, as MS2-Ti remains a single phase. As reported previously,[105,119,120] charge compensation can happen in high-entropy systems by oxidizing or reducing other elements to keep the average charge of ions in the original parent structure. Furthermore, the oxidation states of S ions are different between MS2 and MS compounds. Using FeS_2 as an example, Fe generally shows a valence of 2+, while S exists in the form of disulfide anion (S_2^{2-}), with a valence of 1−.[118] In other binary MS2 compounds, most metal ions adopt oxidation states of 2+, with the exception of Ti^{4+} in TiS_2, where S^{2-} anions are expected to appear. As shown later in XPS measurements, the sulfur anions in MS2 compounds also show mixed valences (1− and 2−). This suggests the potential incorporation of metal cations in states of 2+ and 4+ into the structure of MS2 compounds. Therefore, MS2-Ti compound without secondary phases can be successfully obtained through the replacement of Co^{2+} by Ti^{4+}. Additionally, when Cr ions, which could show valence of 3+ (0.62 Å) and 6+ (0.44 Å), are replaced with the much larger Cu^{2+} ions (0.73 Å), MS2-Cu is obtained and still shows single phase. The shifts of reflection to smaller or larger angles in Figure 4.11 indicate that Cu^{2+} and Ti^{4+} are exactly incorporated into the lattice of high entropy disulfide. These successful replacements demonstrate the excellent resilience and flexibility of high-entropy MS2 compounds for incorporating ions of various charge and size.

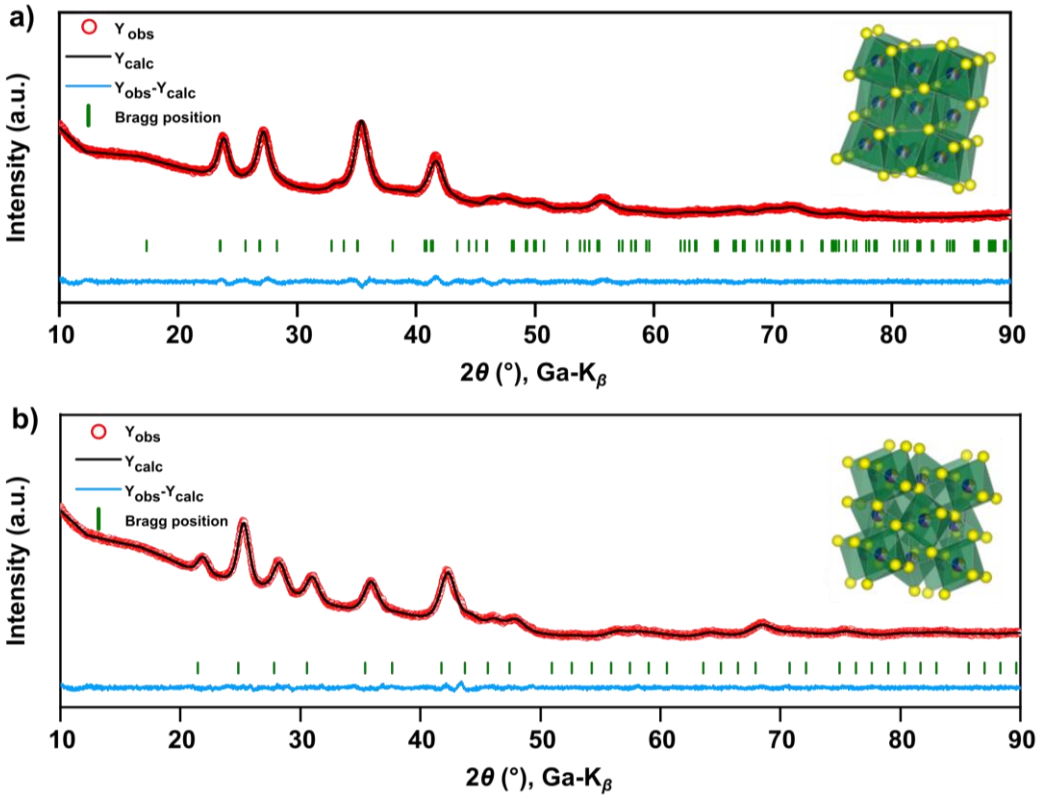

Figure 4.13: Rietveld refinement of (a) MS and (b) MS2.

To investigate the phase of as-prepared sulfides in more detail, XRD refinements of MS and MS2 patterns are shown in Figure 4.13, the refinements of M3S4, M2S3, MS2-Ti and MS2-Cu patterns are shown in Figure 4.14. Additionally, the lattice parameters of single phase HESs (MS, MS2, MS2-Ti and MS2-Cu) are summarized in Table 4.2. Refinement of MS pattern shows pure *Pnma* phase, a unit cell volume V = 110.4(1) Å^3, and the lattice parameters a = 5.443(3) Å, b = 3.428(3) Å, c = 5.913(5) Å. The refinement of M3S4 pattern demonstrates the mixture of *Pnma* and *Pa*-3 phase, corresponding to MS and MS2, respectively. The refinement of M2S3 pattern indicates that *Pa*-3 phase is mainly present. Refinements of MS2s patterns show pure *Pa*-3 phase and imply the impact of Cu^{2+} and Ti^{4+} replacement. Compared to MS2 with V = 177.3(1) Å^3 and a = 5.618(1) Å, the introduction of Cu in MS2-Cu enlarges the unit cell volume V = 181.8(4) Å^3 and the lattice constant a = 5.666(4) Å, the substitution of Ti for Co in MS2-Ti reduces the lattice parameters with V = 176.7(3) Å^3 and a = 5.611(3) Å.

Table 4.2: Refined lattice parameters and unit cell volume of MS and different MS2 compounds

Materials	Space group	a (Å)	b (Å)	c (Å)	V (Å^3)	χ^2	Phase density (g cm^{-3})
MS	*Pnma*	5.443(3)	3.428(3)	5.913(5)	110.4(1)	2.9	5.168(3)
MS2	*Pa*-3	5.618(1)	/	/	177.3(1)	1.4	4.535(2)
MS2-Cu	*Pa*-3	5.666(4)	/	/	181.8(4)	1.3	4.735(9)
MS2-Ti	*Pa*-3	5.611(3)	/	/	176.7(3)	1.2	4.439(7)

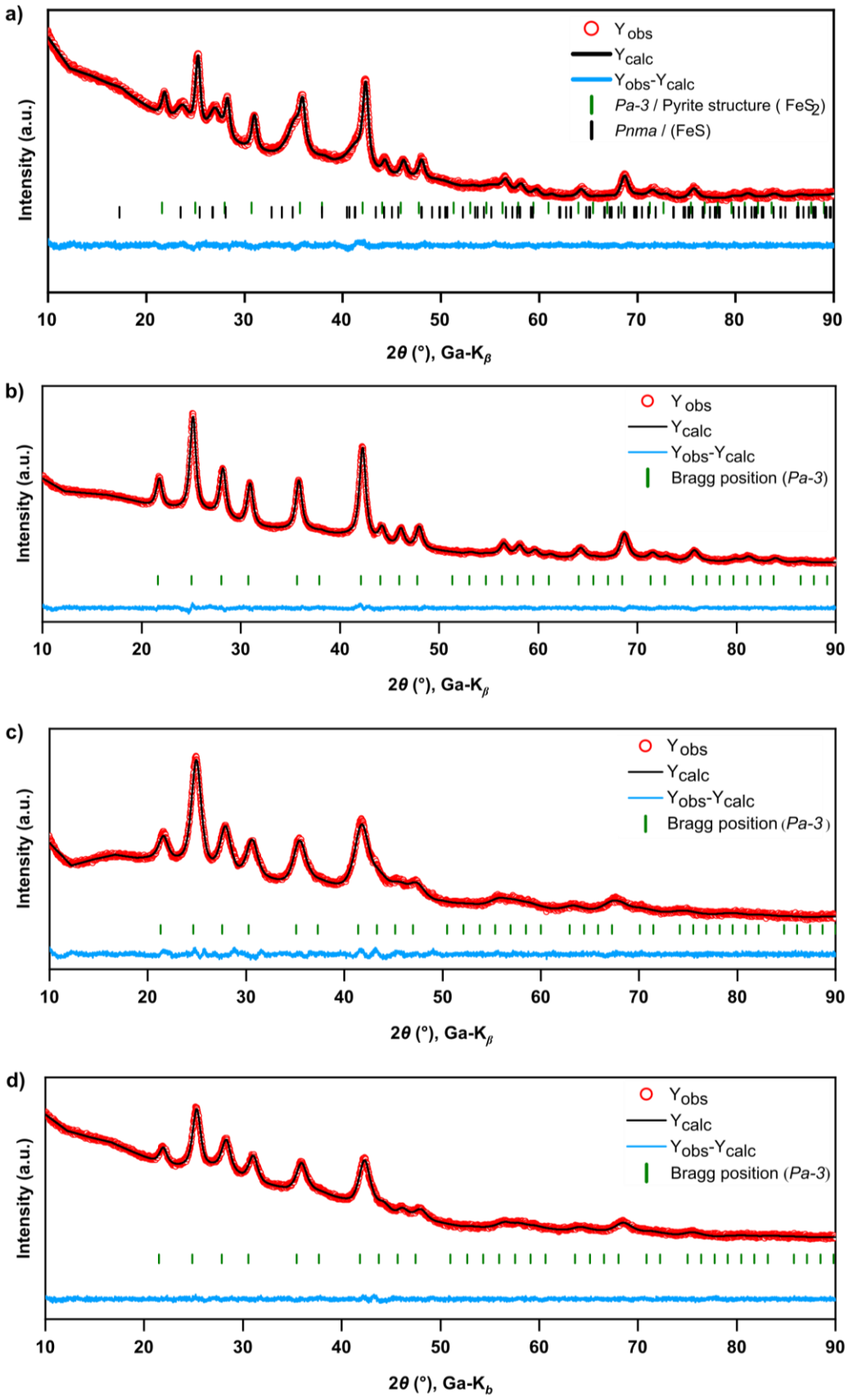

Figure 4.14: Rietveld refinements of (a) M3S4, (b) M2S3, (c) MS2-Cu and (d) MS2-Ti

4.3.2. Elemental Composition

To determine elemental composition of HESs, ICP-OES was carried out and the results are summarized in Table 4.3. The data confirm all theoretical ratios of metal to sulfur are nearly achieved by the one-step high-energy ball-milling process. Additionally, the proportions of transition metals are almost equimolar, which confirms the calculated configurational entropy above 1.5R.

Table 4.3: Stoichiometry of HESs with different metal to sulfur from ICP-OES analysis.

Materials	Normalized to sulfur	Metal to sulfur ratio
MS	$(Fe_{0.21}Mn_{0.21}Ni_{0.21}Co_{0.20}Cr_{0.21})S_1$	1.04:1 (~M_1S_1, *Pnma*)
M2S3	$(Fe_{0.14}Mn_{0.14}Ni_{0.14}Co_{0.13}Cr_{0.14})S_1$	0.69:1 (~M_2S_3, multiphase)
MS2	$(Fe_{0.11}Mn_{0.10}Ni_{0.10}Co_{0.10}Cr_{0.10})S_1$	0.51:1 (~M_1S_2, *Pa*-3)
MS2-Cu	$(Fe_{0.11}Mn_{0.10}Ni_{0.11}Co_{0.10}Cu_{0.11})S_1$	0.53:1 (~M_1S_2, *Pa*-3)
MS2-Ti	$(Fe_{0.10}Mn_{0.10}Ni_{0.09}Cr_{0.10}Ti_{0.09})S_1$	0.48:1 (~M_1S_2, *Pa*-3)

4.3.3. Microstructure

To further study the structural details of the materials, TEM analysis was carried out using samples MS and MS2. Figure 4.15 shows the morphology of HESs with particles of sizes in the range of hundreds of nanometers. HR-TEM micrographs are shown in Figure 4.16a and b. The yellow circled area refers to lattice planes of (011) in MS with lattice spacing of 0.30 nm, and red circled area corresponds to lattice plane of (002) in MS2 with spacing of 0.27 nm.

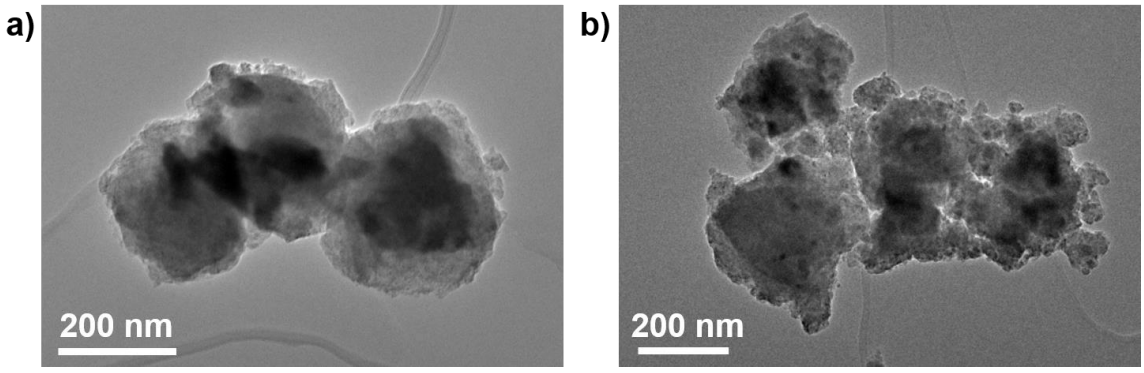

Figure 4.15: TEM images of (a) MS and (b) MS2.

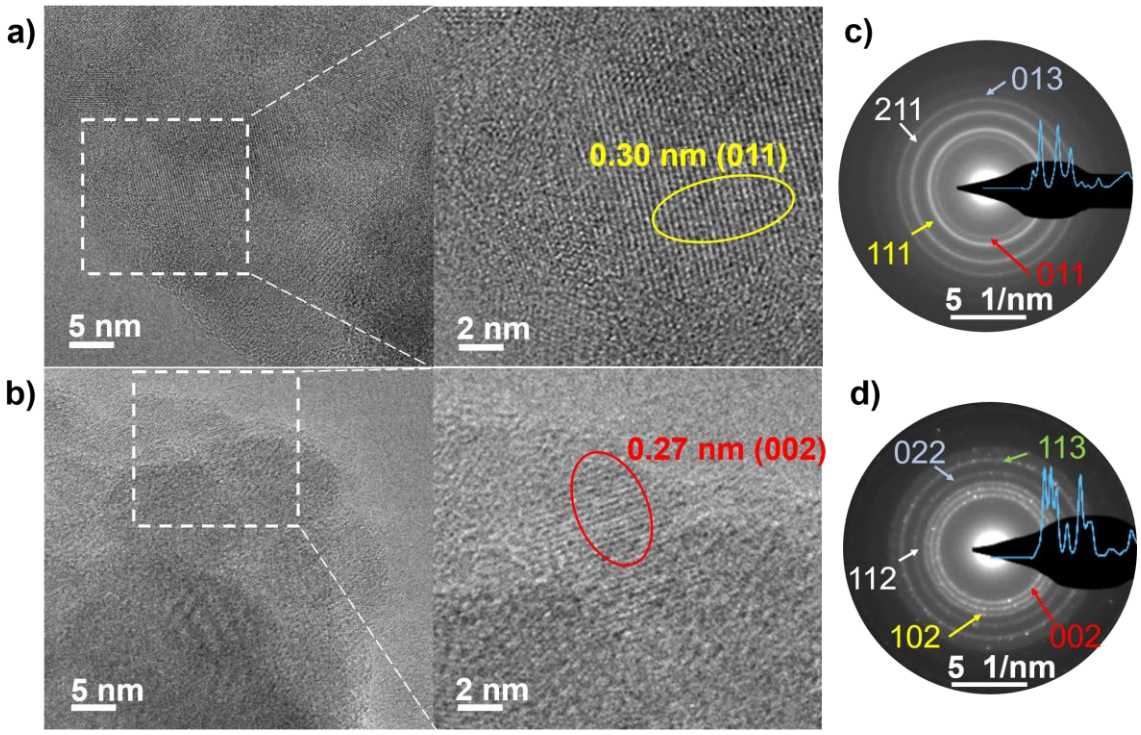

Figure 4.16: HR-TEM image with crystal lattices of (a) MS and (b) MS2. SAED patterns of (c) MS and (d) MS2. The yellow circle refer to the (011) lattice plane with d-spacing of 0.30 nm in MS, and the red circle refer to the (002) lattice plane with d-spacing of 0.27 nm in MS2.

For more information on the crystal structure, SAED of MS, MS2, and M2S3 was performed (Figure 4.16c, 4.16d and 4.17). The diffraction rings of MS and MS2 are in agreement with space group of *Pnma* and *Pa*-3, respectively, and are consistent with the XRD data (Table 4.4).

Table 4.4: *d*-spacing comparisons of SAED and XRD

MS reflection		011	111	211	013
d-spacing measured by SAED (nm)		0.30	0.26	0.20	0.17
d-spacing measured by XRD (nm)		0.30	0.26	0.20	0.17
MS2 reflection	002	102	112	022	113
d-spacing measured by SAED (nm)	0.28	0.25	0.23	0.20	0.17
d-spacing measured by XRD (nm)	0.28	0.25	0.23	0.20	0.17

From the SAED pattern of M2S3 (Figure 4.17), the diffraction rings mainly indicate pyrite phase. However, some other diffraction spots corresponding to 0.19 nm *d*-spacing appear next to the diffraction ring referring to lattice plane (022) of the main *Pa*-3 structure. These spots are probably corresponding to some multi-metal mono-sulfide crystallites or even unreacted precursors, such as CrS, FeS, CoS and NiS (most of their strongest reflection appears during 0.19 -0.20 nm *d*-spacing). Those diffraction signals are only found in SAED, perhaps because the crystallites are too small to be detected by XRD.

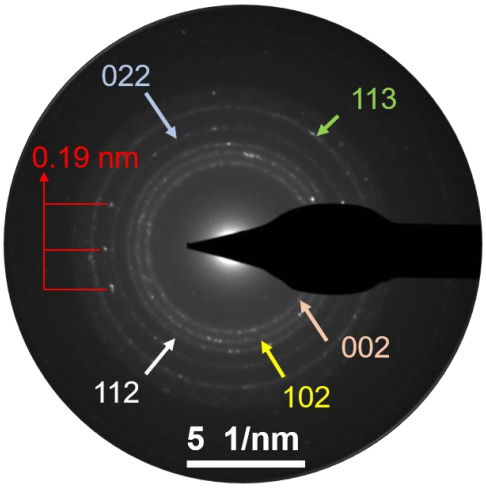

Figure 4.17: SAED taken from M2S3. Additional diffraction spots with *d*-spacing of 0.19 nm appear next to the diffraction ring referring to (022) lattice plane of *Pa-3* structure.

To investigate the elemental distribution of HESs, STEM-EDX elemental maps of MS and MS2 were conducted and are shown in Figure 4.18. The constituent elements are distributed uniformly at nanometer scale, and no obvious segregation or accumulation of individual elements are found. The solid solution state with homogeneous elemental distribution reveals the maximum configurational entropy.

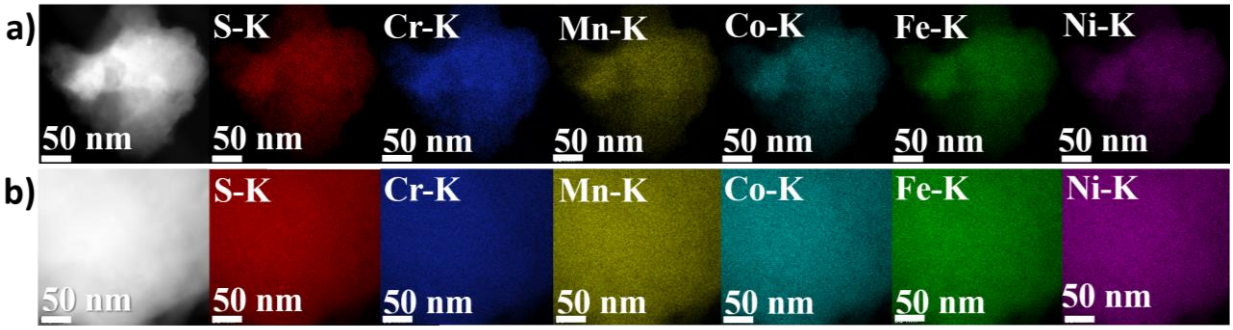

Figure 4.18: STEM-EDX mapping of (a) MS and (b) MS2. All cations and anions are distributed uniformly.

4.3.4. Oxidation State

To further study the oxidation states of HESs with different M:S ratios, XPS measurements were carried out on MS, MS2 and M2S3 powders. XPS analysis can provide surface information about the elemental composition, chemical states, and bonding environments of samples within a depth of 5-10 nm. Survey XPS spectra (Figure 4.19a) show the presence of eight main elements at the surface of all samples, including oxygen (O 1s), sulfur (S 2p), carbon (C 1s), chromium (Cr 2p), manganese (Mn 2p), iron (Fe 2p), cobalt (Co 2p), and nickel (Ni 2p). Due to multiple ion interactions in high-entropy systems and different ionic environments, the characteristic energy can shift slightly. Because of the novelty of the HESs, accurate determination of the oxidation state is very difficult without an exact reference.

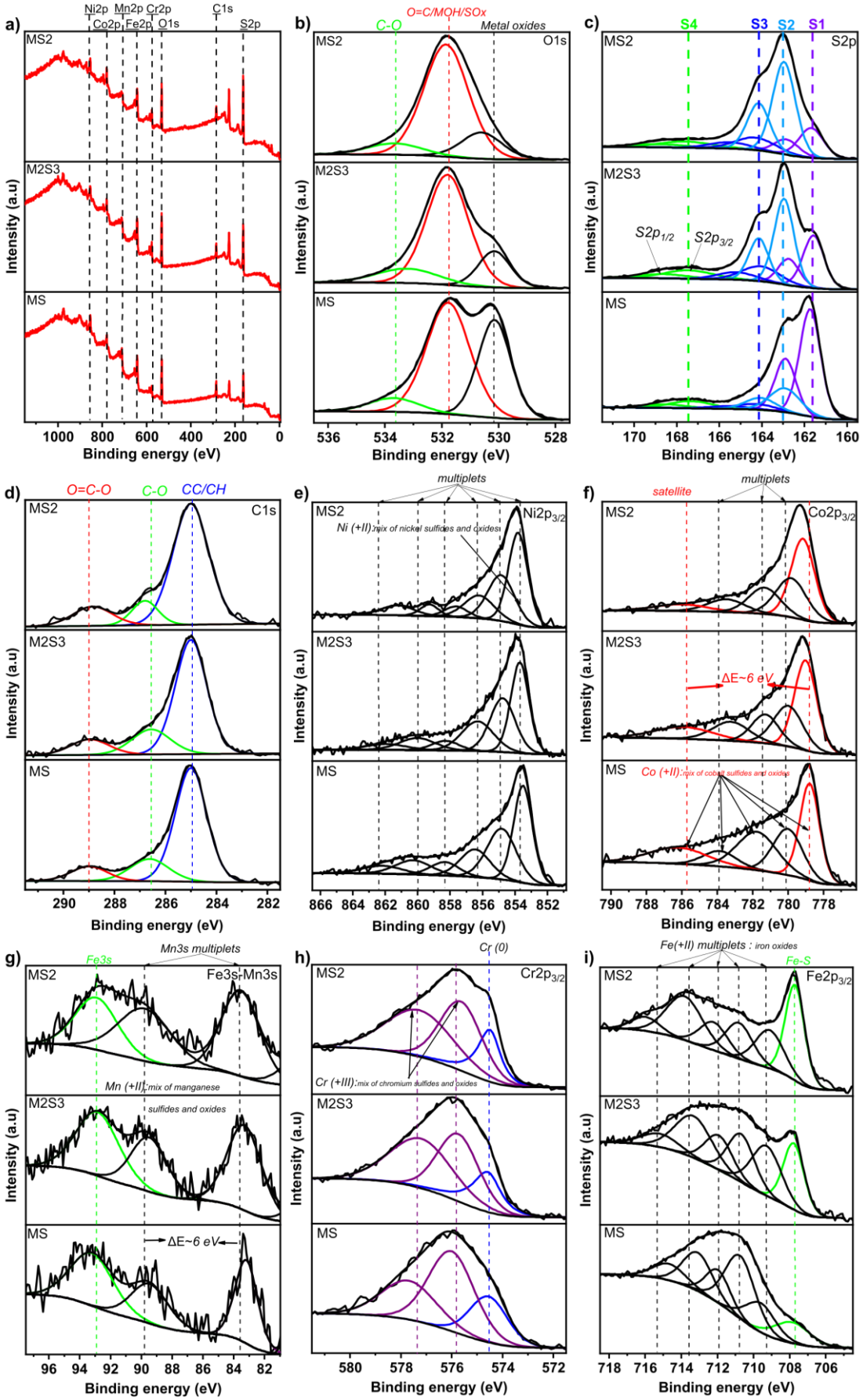

Figure 4.19: (a) Survey, (b) O 1s, (c) S 2p (d) C 1s, (e) Ni 2p, (f) Co 2p, (g) Mn 3s, (h) Cr 2p and (i) Fe 2p XPS spectra of HESs samples with different M:S ratio (MS, M2S3 and MS2 respectively).

The O 1s spectra (Figure 4.19b) reveal the chemical states and environments of oxygen atoms present at the surface. The main peak at 531.8 eV corresponds to a mixture of metal hydroxides (MOH), O=C and SO_X compounds. The peak at a low binding energy (~530.3 eV) can be attributed to metal oxides. Another peak at a high binding energy (~533.5 eV) comes from C-O environment. The presence of metal oxides and SO_X species suggests a slight oxidation of sample surfaces in the storage environment (glove box) or during the transfer process to XPS analysis.

The S 2p spectra (Figure 4.19c) are fitted with $2p_{3/2}$-$2p_{1/2}$ doublets separated by 1.2 eV with 2/1 intensity ratio due to spin-orbit coupling. Four components are shown in spectra: (S1) MS shows the main doublet with $2p_{3/2}$ component at 161.7 eV, corresponding to S_{2-} anion. (S2) The main doublet with $2p_{3/2}$ component at 162.9 eV from M2S3 and MS2 is attributed to S_2^{2-} (disulfide ion) environment, which can be always detected in polysulfide groups as M2S3 and MS2.[121,122] (S3) Another doublet with $2p_{3/2}$ component at 164.2 eV is the signal of S-S environments. (S4) The doublet with $2p_{3/2}$ component at 167.4 eV corresponds to SO_X (S^{4+} oxidation state).

The C 1s spectra (Figure 4.19d) reveal presence of three peaks coming from all carbon species at the surface. The peaks centered at 285 eV, 286.5 eV and 289 eV correspond to hydrocarbon contamination (C-C/C-H), mono and bi oxygenated carbon environments, respectively. These components are always present at the surface of samples during XPS analysis.

Based on the literature,[123–125] the spectra of the incorporated metals (Ni 2p, Co 2p and Mn 3s) indicate the oxidation state of 2+, which could be attributed to a mixture of metal oxides and sulfides, as shown in Figure 4.19e-g. The Cr 2p spectra (Figure 4.19h) show signals of different valence. The peak at the low binding energy (~574 eV) corresponds to chromium metal, probably coming from Cr metal precursor. As for others, two peaks at the high binding energies (~576 eV and ~577 eV) confirm the mixture of chromium sulfides and oxides, respectively, present on the powder surface.[123] The Fe 2p spectra (Figure 9i) clearly show a partial oxidation of iron. However, the proportion of oxidized iron seems to depend on the proportion of sulfur in the HES structure. Indeed, the proportion of oxidized iron seems to decrease when the proportion of sulfur increases.

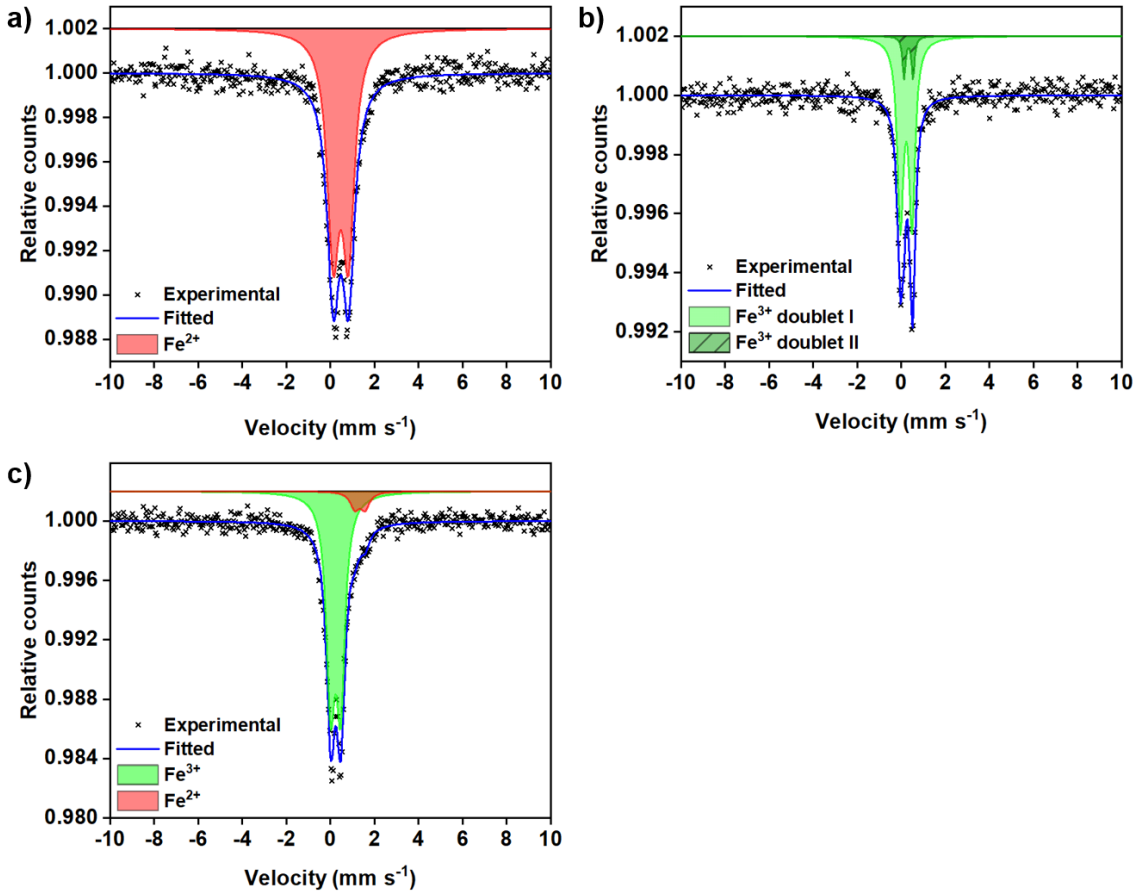

Figure 4.20: Mössbauer spectrum of (a) MS, (b) MS2 and (c) M2S3.

Mössbauer spectroscopy can distinguish extremely small changes in the oxidation state and chemical environment of Fe. Consequently, Mössbauer spectroscopy has used to study the Fe environment in MS, MS2 and M2S3. The Mössbauer spectrum of MS (Figure 4.20a) is fitted by only one doublet, corresponding to Fe^{2+} with an isomer shift (IS) of 0.598(4) mm s^{-1} and the quadrupole splitting (QS) of 0.691(7) mm s^{-1}. It indicates that all Fe ions are located in a very homogeneous chemical environment. Figure 4.20b shows the Mössbauer data of MS2, fitted by two quadrupole doublets sub-spectra, which indicate two Fe^{3+} environments (doublet I and II) with two IS (I = 0.350(7) mm s^{-1}, II = 0.454(4) mm s^{-1}) and two QS (I = 0.527(9) mm s^{-1}, II = 0.408(3) mm s^{-1}). As quantified by relative area fraction, the majority (90%) of detected Fe^{3+} species is Fe^{3+} (doublet I) and Fe^{3+} (doublet II) accounts for 10%. This could be the influence of the slightly oxidized surface, as discussed in XPS measurement. The Mössbauer data of M2S3 (Figure 4.20c) also shows Fe in two different environments, but different from MS2. It fitted by two quadrupole doublets sub-spectra corresponding to Fe in two oxidation states. The majority (92%) of Fe homogenously distribute in pyrite HES, displaying Fe^{3+} with doublet sub-spectrum of QS = 0.456(4) mm s^{-1} and a very close IS (0.365(0) mm s^{-1}) compared to the Fe^{3+} (doublet I) in MS2. The remaining (8%) Fe species is Fe^{2+} with doublet sub-spectrum of IS (1.468(4) mm s^{-1}) and QS (0.465(6) mm s^{-1}), which can be attributed to other minor phase of metal mixed mono-sulfides detected by SAED. This result also confirms the previous supposition of a MS secondary phase.

4.4. Conclusions

In summary, this chapter presents the characterization of as-prepared transition-metal-based HEO, Li(HEO)F and HES. A low-cost facile mechanochemical synthesis route was developed, which avoids high-temperature preparation or solution processes and allows the incorporation of redox-sensitive ions into single-phased high-entropy materials. The use of an inert atmosphere inhibits oxidation during synthesis. No charge compensating components, such as Li ion, are required. The internal disproportionation reactions, existing in multi-metallic high-entropy systems, don't change the average charge of the anion or cation in the sublattice and therefore don't cause structural changes to maintain charge neutrality. Four HEO and four multi-anionic Li(HEO)F with novel element composition were successfully synthesized and showed pure rock-salt phase. Afterwards, using the same method, novel HESs with designed M:S ratios were easily prepared and single phase HESs were formed with *Pnma* and *Pa*-3 crystal structures. All as-prepared high entropy materials were found to consist of particles with sizes in the range of hundreds of nanometers. All elements are uniformly distributed. This work provides a pathway for the design and synthesis of novel classes of high-entropy materials, extends the choice of applicable elements and countless further compositions for various applications. Some possible applications will be discussed in the following chapters.

Chapter 5

5. High Entropy Sulfides as Electrode Materials for Batteries

Major parts of the results in this chapter was published in Advanced Energy Materials.[45]

5.1. Introduction

Transition metal sulfides (TMSs) are a significant group of inorganic materials that have been widely investigated for applications in photonics,[126] catalysis,[20] lubrication,[127] electrochemistry,[128] and magnetism.[129] In the field of electrochemical energy storage, such as Li-ion batteries (LIBs), Na-ion batteries and supercapacitors, TMSs have gained immense attention as potential electrode materials owing to their low cost and high theoretical specific capacities.[128,130] For example, cobalt sulfides (CoS_X) are regarded as promising conversion-type electrode materials with theoretical specific capacities as high as 870 mA h g^{-1} for CoS_2, 702 mA h g^{-1} for Co_3S_4, 589 mA h g^{-1} for CoS, and 545 mA h g^{-1} for Co_9S_8.[130]

HEMs are typically composed of at least five or more elements, resulting in complex structures and highly tailorable properties. Before 2022, HESs as a new discovered class of HEMs have exhibited promising performance in thermoelectricity and electro-catalysis.[60–62] HESs could be promising to tailor the properties of TMSs by incorporating a wide range of elements for high-performance electrodes. Herein, several different HEMs prepared and characterized in chapter 4 are investigated and compared as electrode materials in LIBs. The study of HESs in battery applications constitutes a major part of this chapter.

5.2. Results and Discussion

In this chapter, the use of HESs as battery materials is described for the first time. Three novel pyrite (Pa-3) HES2s (metals being Fe, Co, Ni, Mn, Cu, Cr or Ti) and one orthorhombic (Pnma) HES1 (metals being Fe, Co, Ni, Mn, Cr) are investigated as electrode materials in LIBs.

5.2.1. XRD of Electrode Materials

In order to investigate electrochemical properties of HESs, single phase HES samples prepared in chapter 4.3 were applied in LIBs. To increase the electronic conductivity, HESs were mixed with multi-walled carbon nanotubes (MWCNTs) in a weight ratio of 9:1 (HES:MWCNTs), This mixture was used as active materials in half-cells with a lithium metal anode. Pure MWCNTs and CoS_2 mixed with the same ratio of MWCNTs were used as reference.

XRD measurements of the unused dried electrodes were conducted to investigate the possible decomposition or structural changes of the prepared sulfides, as some metal sulfides are known to be sensitive to moisture in the air.[131,132] As shown in Figure 5.1a, no degradation products or structural changes are detected, which implies that HESs are stable in the electrode preparation process. Additionally, a medium entropy sulfide $(FeMnNiCo)S_2$ (4MS2) was also prepared using the same way as the other HES2s, in order to investigate the effect of high entropy. XRD patterns of all prepared electrodes for other materials used are provided in Figure 5.1b.

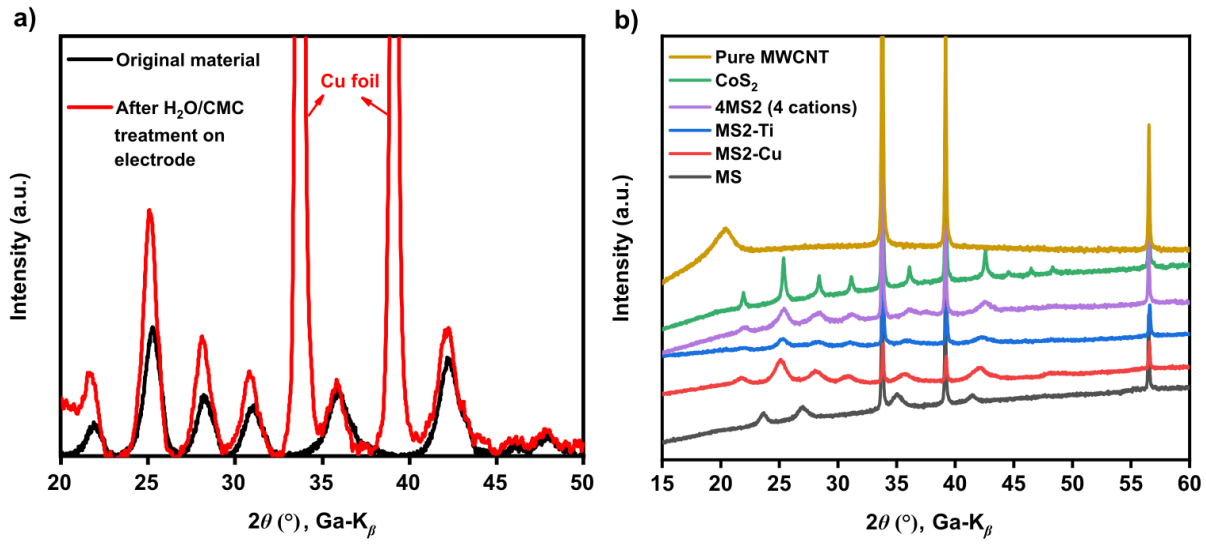

Figure 5.1: (a) Comparison of XRD patterns of MS2 and as-prepared MS2 electrode. (b) XRD pattern of other prepared electrodes. No decomposition products are observable. The high intensity peaks at about 34, 39 and 57° are from the copper current collector and the broad reflection at around 20° are from the MWCNTs.

5.2.2. Electrochemical Performance of High Entropy Sulfides

To investigate the electrochemical redox potentials of HESs, CV measurements were performed and are shown in Figure 5.2. For pyrite HES2s including MS2, MS2-Cu and MS2-Ti, the cathodic peaks between 0.8 to 1.7 V in the initial lithiation process can be ascribed to the reduction of HESs to metal and Li_2S.[133] Referring to the reaction of other metal sulfides with the same crystal structure (such as CoS_2 and FeS_2), their first discharge reaction can be interpreted in two steps:[130,134,135] 1) $MS_2 + xLi^+ + xe^- \rightarrow Li_XMS_2$ (peak at about 1.6 V), 2) Li_XMS_2

+ (4–x)Li^+ + (4–x)e^- → $2Li_2S$+M. Subsequently, two distinct anodic peaks occur around 2.0 V and 2.4 V in delithiation process. They could be assigned to two-step re-sulfidation process. The split of the anodic peak might be subject of the different sulfidation potentials of the incorporated transition metals.[133,136] In addition to the upshift of the reduction peaks from second cycle, the CV curves in following cycles almost overlap, which indicates reversibility during the first cycles. Compared to CoS_2 in CV curves (Figure 5.2e), HES2s behave similar redox performance. But probably due to the cocktail effect of multiple elements in HESs, they show broader peaks and shifted reaction potentials.

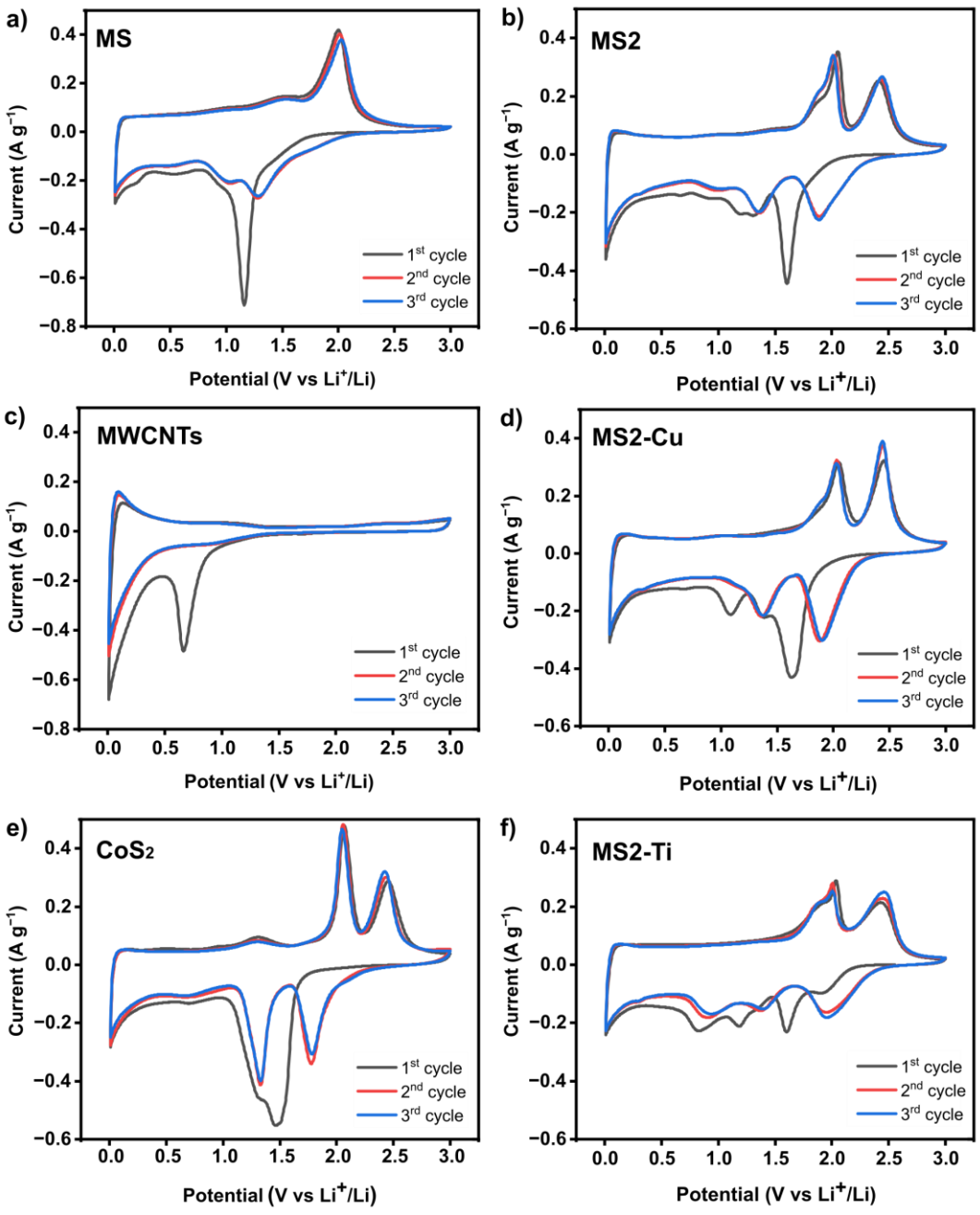

Figure 5.2: CV profiles of (a) MS, (b) MS2, (c) MWCNTs, (d) MS2-Cu, (e) CoS_2 and (f) MS2-Ti measured in the voltage range of 0.01-3 V vs Li^+/Li with a scan speed of 0.1 mV s^{-1}.

For high entropy mono-sulfides MS, one strong oxidation peak occurs at about 2.0 V and no peak is found at 2.4 V in the initial cycle, indicating a one-step oxidation. In addition, compared to CV of MWCNTs electrode (Figure 5.2c), the peaks below 0.7 V of HESs could come from Li-ion intercalation/insertion into the carbon materials, such as MWCNTs and conductive additive.

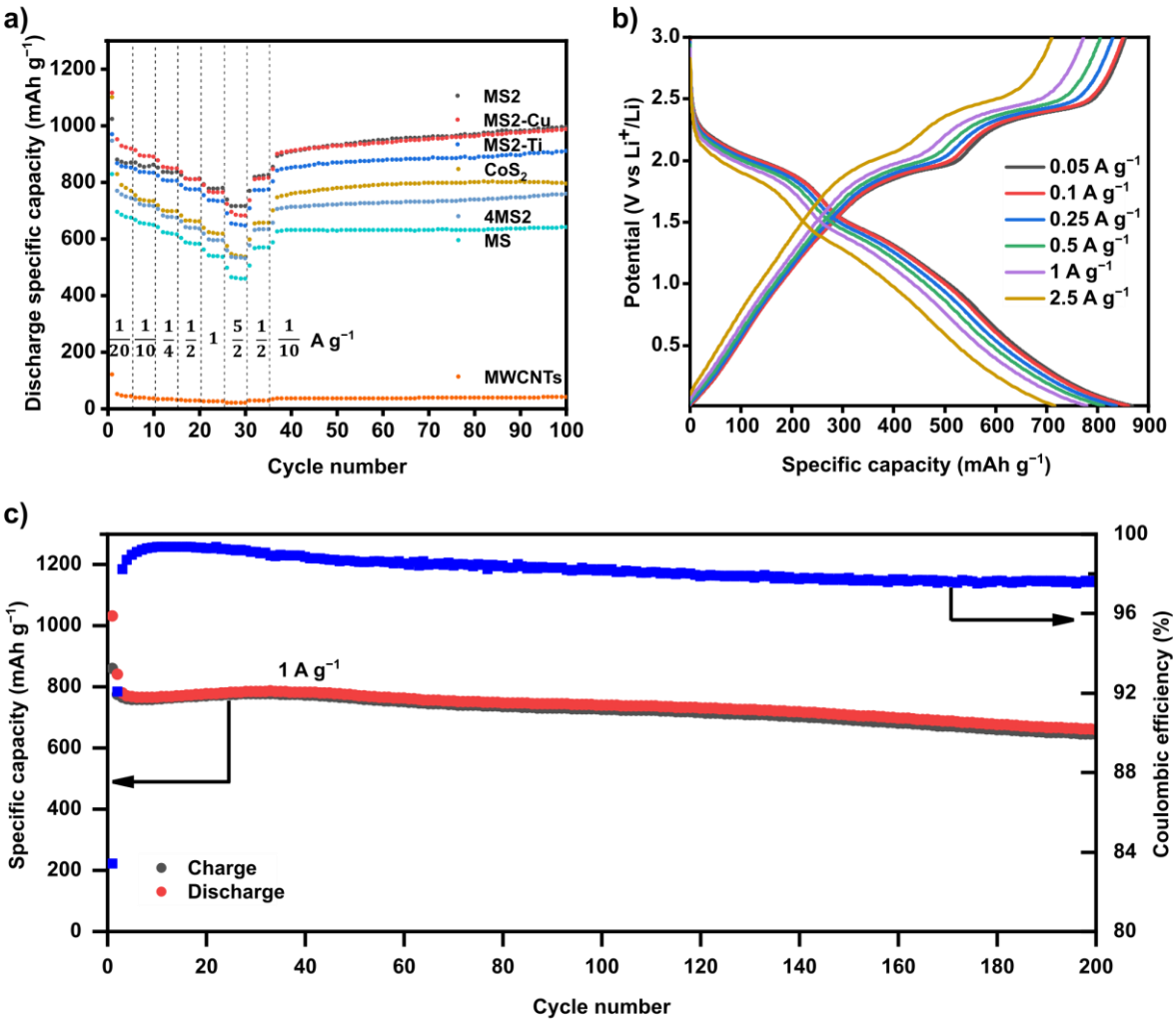

Figure 5.3: (a) Galvanostatic rate performance of all as-prepared HESs, CoS_2, 4MS2 and MWCNTs half-cell measured in different current densities. (b) Voltage profiles of MS2 half-cell at different current densities. (c) Specific charge/discharge capacity of MS2 half-cell and Coulombic efficiency as a function of cycle number at 1 C. All cell were measure at 25 °C and in the voltage range between 0.01 and 3 V vs Li^+/Li.

The galvanostatic rate performance of CoS_2, pure MWCNTs and as-prepared HESs at different currents is shown in Figure 5.3a. As HESs are mixed with MWCNTs in a 1:9 ratio, the maximum capacity contribution of MWCNTs for electrodes is also given in Figure 5.3a. During the rate performance test, MS2, MS2-Ti and MS2-Cu show improved discharge capacities of 994, 909 and 986 mA h g^{-1}, respectively, compared to MS of 642 mA h g^{-1} and CoS_2 of 795 mA h g^{-1} after 100 cycles. MS2-Cu initially shows the highest specific discharge capacities, however, as current density increases to 1 and 2.5 A g^{-1}, MS2 exhibits increasingly better performance. And after returning to 0.5 A g^{-1} and 0.1 A g^{-1}, they show comparable discharge capacities. During the first 100 cycles, HESs generally

show good cycling stability and rate stability. It is worth noting that the specific capacities rise about 200-300 mA h g^{-1} when the fraction of absolute S increases (HES1 to HES2s). It stems from the fact that metal disulfides take two-step reaction as explained in CV analysis, and are able to exchange more lithium ions and electrons than mono-sulfide materials. To illustrate the positive effect of the high-entropy concept, 4-component sulfide $(FeMnNiCo)S_2$ (4MS2) was studied and compared (Figure 5.3a). 4MS2 is prepared using the same method as other HESs as an example for a medium-entropy disulfides with configurational entropy below 1.5R. From the galvanostatic rate results, HES2s all present higher specific capacities than 4MS2 and CoS_2.

Since MS2 displays the best rate performance, its voltage profiles at different currents are discussed. As shown in Figure 5.3b, MS2 performs remarkably with reversible discharge capacities of 868, 860, 837, 812, 779 and 716 mA h g^{-1} at current rate of 0.05, 0.1, 0.25, 0.5, 1 and 2.5 A g^{-1}, respectively. The plateaus located at about 2.4 V and 1.9 V could also imply the two-stage reaction process of HES2s. A similar behavior for FeS_2 is observed by Fong et al..[134] Furthermore, MS2 exhibits good long-term stability as shown in Figure 5.3c. After 200 cycles at 1 A g^{-1}, the specific capacity of MS2 remains at 645 mAh g^{-1} (charge) and 660 mAh g^{-1} (discharge) at a high Coulombic efficiency of ~98%.

From Figure 5.3a, it seems that the capacity of HESs at lower C-rates surpasses the theoretical gravimetric capacity of 595 mAh g^{-1} for MS, 885 mAh g^{-1} for MS2, 850 mAh g^{-1} for MS2-Cu and 927 mAh g^{-1} for MS2-Ti. This additional capacity may stem from the reaction between Li and MWCNTs at lower potentials and exhibits variations in accordance with the corresponding C-rates. Furthermore, conversion reactions exhibit a slightly increased capacity than anticipated due to various factors such as the formation of solid electrolyte interphase (SEI), irreversible reactions and particle cracking. The rise in capacity shown in Figure 8a, beginning at cycle 35, may be attributed to the slow C-rate, which often results in a combination of significant volume expansions and the re/formation of SEI. This effect is no longer visible at higher C-rates (Figure 5.3c), as some slow reactions occurring during the conversion process are suppressed, resulting in a reduction in capacity.

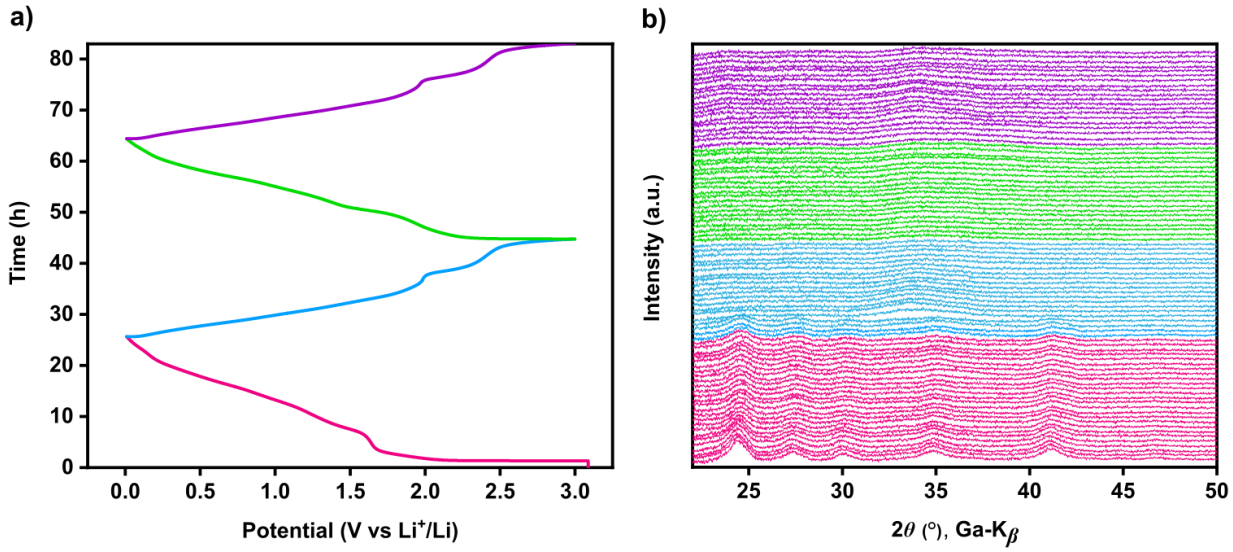

Figure 5.4: Operando XRD of MS2 collected during discharge and charge process in first two cycles at current density of 50 mA g^{-1} between 3 and 0.01 V vs Li^+/Li, including (a) corresponding voltage profiles and (b) diffraction patterns.

To have a better understanding of the conversion mechanism and structural changes during cycling, operando XRD of MS2 was conducted (Figure 5.4). During the first discharge process, the potential drops quickly to around 1.7-1.6 V, which could be ascribed to the intercalation of Li^+ into the structure and formation of Li_XMS_2 compound, as discussed in CV results. At this point, MS2 remains in the initial pyrite structure. As the lithiation proceeds, the XRD intensity of pyrite peaks becomes weaker. Additionally, an amorphous phase may be formed during lithiation, which is not easily detectable by XRD.[137,138] At the beginning of the first delithiation process, the characteristic reflections from the pyrite structure gradually disappear and do not reappear upon subsequent reaction. It could arise from the formation of small crystallites below the XRD detection limit, which is a typical behavior observed in conversion materials.[16,138,139]

5.2.3. Battery Performance of High Entropy Oxides

Compared to earlier work of NSP-produced rock-salt HEOs in batteries,[49] many of the HEOs in chapter 4.2 incorporated elements that could only be introduced utilizing the explained mechanochemical approach. Figure 5.5a displays the galvanostatic rate performance of four HEOs, (ZnNiCoMnCu)O (HEO-5MC), (ZnNiCoMnFe)O (HEO-5MF), (ZnNiCoMnFeCu)O (HEO-6M) and (ZnNiCoMnFeCuMg)O (HEO-7M), as conversion electrode materials in LIBs. During the first 100 cycles, HEOs generally show good cycling and rate stability. After 100 cycles at 0.1 A g^{-1}, HEO-5MC, HEO-5MF, HEO-6M and HEO-7M exhibit discharge capacities of 430, 290, 387 and 318 mA h g^{-1}, respectively. Among four HEOs, HEO-5MC exhibits the best performance, suggesting that the battery performance of high entropy materials is more influenced by the type of incorporated elements rather than an even higher value of configurational entropy. Figure 5.5b shows the voltage profiles of HEO-5MC with the discharge capacities of 672, 552, 424, 336, 260 and 171 mA h g^{-1} at current rate of 0.1, 0.2, 0.5, 1, 2 and 5 A g^{-1}, respectively.

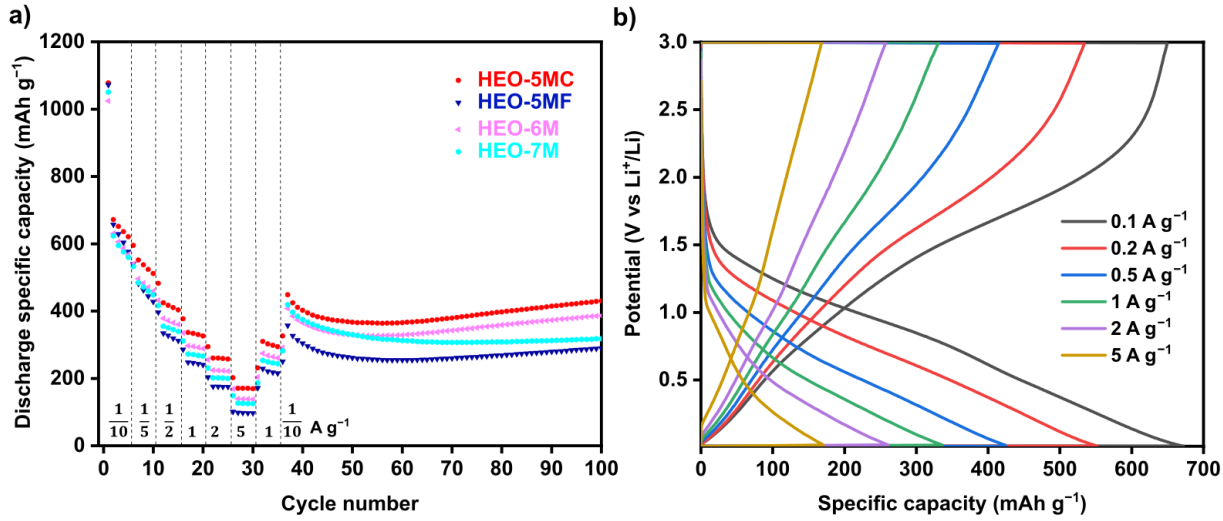

Figure 5.5: (a) Galvanostatic rate performance test of HEO-5MC, HEO-5MF, HEO-6M and HEO-7M half-cell at different current densities and 25 °C in the voltage range between 0.01 and 3 V vs Li^+/Li. (b) Voltage profiles of HEO-5MC half-cell at different current densities.

5.3. Conclusions

In summary, this work presents the application of novel HESs based on transition metals for the purpose of energy storage. Through comparison with binary sulfide CoS_2, and medium entropy sulfide 4MS2, HESs were evaluated as electrode materials for Li-ion batteries. The results revealed that high-entropy MS2 compounds exhibit superior performance, indicating the positive influence of the cocktail effects. The advent of the high-entropy concept enables the incorporation of metals into structures that would not typically form as binary sulfides (such as CrS_2). Furthermore, the comparison of HEOs indicates the battery performance of high entropy materials is more influenced by the type of incorporated elements rather than an even higher value of configurational entropy. The high-entropy concept facilitates customization of material's composition, wherein elements can be added or replaced. Thus, the potential exists for HESs containing elements with uncommon oxidation states or chemical environments, which may exhibit enhanced electrochemical performance. In light of the availability of customizable materials that allow for a very large number of possible combinations, it would be worth developing the application of HESs in rechargeable batteries. Some possible application of HESs for energy conversion will be discussed in the following two chapters.

Chapter 6

6. High Entropy Sulfides as Electrocatalysts for Oxygen Evolution Reaction

Major parts of the results in this chapter was published in Small Structure.[140]

6.1. Introduction

Owing to the global environmental and energy crises, research in sustainable energy conversion and storage has attracted great attention recently. One of the essential candidates for replacement of fossil fuels is clean hydrogen, which can be produced by electrocatalytic water splitting. Unfortunately, the oxygen evolution reaction (OER) at the respective anode has a complicated mechanism of four-electron transfer process[25,27,28] and usually shows slow reaction kinetics and high overpotentials. These features could be regarded as the key bottleneck hindering the application of electrocatalytic water splitting on a large scale. One solution is to develop improved catalyst materials, where transition metal-based materials have been studied widely to reduce the overpotential of OER and hence to improve reaction efficiency. In this prospect, transition metal sulfides are promising competitors as OER catalysts due to their greatly variable redox chemistry and high activities.[31,141,142]

Recently, transition metal-based HESs have been investigated as promising catalysts for OER. The first report was published by Cui et al. in 2020.[60] Cubic *Fm*-3*m* structured $(CrMnFeCoNi)_9S_8$, synthesized by a pulsed thermal decomposition method, has been shown to be a good OER electrocatalyst. Subsequently, in 2021,[76] pyrite *Pa*-3 structured $FeNiCoCrXS_2$ (with X = Mn, Cu, Zn, or Al), prepared by solvothermal method, was reported by Nguyen et al.. Subsequently, several relevant studies come out from 2022.[77,80,81,102]

Herein, based on the previous results obtained on orthorhombic (*Pnma*) and pyrite (*Pa*-3) structured HESs with equimolar incorporated metal, new *Pnma* structured HESs with non-equimolar metal are presented. The strucuture, composition and morphology of HESs are investigated and compared. With homogeneous element distribution, all HESs show particles with sizes ranging in the hundreds of nanometers. When serving as OER catalysts, most as-prepared HESs show better OER activities than commercial IrO_2. Compared to high entropy compounds with

different anions, such as O and F, HESs show a substantially improved OER performance. Chronopotentiometric measurements indicate good stability of HESs under alkaline conditions. This work contributes to more HES as promising catalysts for future OER applications.

6.2. Results and Discussion

In this character, seven *Pnma* structured HESs and three *Pa*-3 structured HESs are compared in composition, structure and morphology by ICP-OES, XRD, SEM, TEM, EDX measurements. All ten as-prepared HESs materials were investigated as OER electrocatalysts and compared with each other and with IrO_2 (commercial OER catalyst, as reference material). The investigation involved evaluating their OER overpotential, Tafel slope, ionic conductivity, electrochemically active surface area (ECSA), and durability through linear sweep voltammetry (LSV), electrochemical impedance spectroscopy (EIS), cyclic voltammetry (CV), and chronopotentiometry measurements. The OER activity of high entropy oxide and oxyfluoride are also compared with sulfides by LSV measurement.

6.2.1. Composition Design and Structure

Due to their low cost (compared with platinum-group metals) and their excellent electrocatalytic performance, 3d transition metal-based compounds, e.g., NiFe-based materials, are considered as promising OER electrocatalysts and attract great attention.[143,144] One way to further improve OER performance is through the incorporation of these catalysts with other metals (like Ti,[145] Mn,[146] and Co[141]), which allows for the adjustment of the electronic structure of the active center. Herein, the most promising metals are taken into consideration and finally several single-phase HESs including five or six transition metals (Ti, Fe, Co, Ni, Mn, Cu, Ag, Cr, Mo) are obtained. The overview of samples is shown in Table 6.1. All HESs were directly prepared by a one-step high-energy ball-milling route in Ar atmosphere and without further processing. The composition and nominal value shown in Table 6.1 is calculated based on the ratio of raw materials (metal sulfides, sulfur and metal). To confirm the compositions of the samples, ICP-OES and EDX were conducted and the results are compared in Table 6.1. Although Ag ratio of HESMoAg-1 and some S ratio measured by ICP-OES are lower than expected, these missing proportions could be attributed to unidentified part, such as undetectable precipitates insoluble in aqua regia. When further compared by combining the EDX results, the ratios of the elements are basically close to the expected.

Table 6.1: Overview of the synthesized different HESs.

Abbreviation	Synthetic Composition	S_{config}	Structure	Method	Mass ratio [%]
HESMo	$TiFe_2Co_2Ni_3MoS_{10}$	1.52*R*	*Pnma*	Nominal	Ti 5.5 Fe 12.8 Co 13.5 Ni 20.2 Mo 11.0 S 36.9
				ICP-OES	Ti 5.6 Fe 13.3 Co 13.6 Ni 19.8 Mo 10.2 S 28.5
					unidentified part 9.0
				EDX	Ti 5.2 Fe 12.2 Co 12.9 Ni 17.9 Mo 9.0 S 42.7
HESMoMn	$TiFe_2Co_2Ni_3MoMn_2S_{12}$	1.72*R*	*Pnma*	Nominal	Ti 4.6 Mn 10.5 Fe 10.7 Co 11.3 Ni 16.9 Mo 9.2 S 36.9
				ICP-OES	Ti 4.7 Mn 10.7 Fe 12.0 Co 12.2 Ni 17.1 Mo 8.6 S 31.4
					unidentified part 3.3
				EDX	Ti 4.8 Mn 11.0 Fe 11.4 Co 12.0 Ni 16.5 Mo 9.0 S 35.2
HESMoCu	$TiFe_2Co_2Ni_3MoCu_2S_{12}$	1.72*R*	*Pnma*	Nominal	Ti 4.5 Fe 10.5 Co 11.1 Ni 16.6 Cu 12.0 Mo 9.0 S 36.3
				ICP-OES	Ti 4.2 Fe 11.4 Co 12.1 Ni 17.4 Cu 13.3 Mo 8.9 S 32.4
					unidentified part 0.3
				EDX	Ti 4.6 Fe 10.0 Co 10.8 Ni 14.8 Cu 11.9 Mo 8.2 S 39.8
HESMoCu-1	$TiFe_2Co_2Ni_3MoCu_2S_{11}$	1.72*R*	*Pnma*	Nominal	Ti 4.7 Fe 10.9 Co 11.4 Ni 17.1 Cu 12.3 Mo 9.3 S 34.3
				ICP-OES	Ti 4.8 Fe 11.3 Co 11.7 Ni 17.0 Cu 12.7 Mo 8.7 S 33.6
					unidentified part 0.2
				EDX	Ti 4.5 Fe 10.2 Co 10.6 Ni 14.7 Cu 14.8 Mo 8.3 S 36.9
HESMoAg-1	$TiFe_2Co_2Ni_3MoAg_2S_{11}$	1.72*R*	*Pnma*	Nominal	Ti 4.3 Fe 10.0 Co 10.5 Ni 15.8 Mo 8.6 Ag 19.3 S 31.5
				ICP-OES	Ti 4.5 Fe 10.1 Co 10.2 Ni 16.0 Mo 7.8 Ag 0.7 S 27.7
					unidentified part 23.0
				EDX	Ti 4.5 Fe 9.8 Co 10.2 Ni 14.9 Mo 8.2 Ag 16.1 S 36.2
HESCu	$TiFe_2Co_2Ni_3Cu_2S_{10}$	1.56*R*	*Pnma*	Nominal	Ti 5.3 Fe 12.4 Co 13.1 Ni 19.5 Cu 14.1 S 35.6
				ICP-OES	Ti 5.0 Fe 11.7 Co 12.3 Ni 17.4 Cu 14.5 S 17.8
					unidentified part 21.3
				EDX	Ti 5.2 Fe 11.1 Co 12.2 Ni 16.4 Cu 16.6 S 38.6
MS	$MnFeNiCoCrS_5$	1.61*R*	*Pnma*	Nominal	Mn 12.5 Fe 12.7 Ni 13.3 Co 13.3 Cr 11.8 S 36.4
				ICP-OES	Mn 12.4 Fe 12.6 Ni 13.2 Co 12.4 Cr 11.5 S 34.3
					unidentified part 3.6
				EDX	Mn 13.2 Fe 13.9 Ni 13.3 Co 13.0 Cr 12.6 S 33.9
MS2	$MnFeNiCoCrS_{10}$	1.61*R*	*Pa*-3	Nominal	Mn 9.1 Fe 9.3 Ni 9.8 Co 9.8 Cr 8.7 S 53.3
				ICP-OES	Mn 8.4 Fe 8.8 Ni 9.0 Co 8.9 Cr 8.0 S 47.3
					unidentified part 9.6
				EDX	Mn 9.6 Fe 9.8 Ni 9.8 Co 9.8 Cr 8.9 S 52.0
MS2-Cu	$MnFeNiCoCuS_{10}$	1.61*R*	*Pa*-3	Nominal	Mn 9.0 Fe 9.1 Ni 9.6 Co 9.6 Cu 10.4 S 52.3
				ICP-OES	Mn 8.2 Fe 8.5 Ni 8.9 Co 8.6 Cu 9.7 S 45.7
					unidentified part 10.4
				EDX	Mn 8.6 Fe 8.8 Ni 8.7 Co 8.5 Cu 10.2 S 55.2
MS2-Ti	$MnFeNiTiCrS_{10}$	1.61*R*	*Pa*-3	Nominal	Mn 9.3 Fe 9.5 Ni 9.9 Ti 8.1 Cr 8.8 S 54.3
				ICP-OES	Mn 8.0 Fe 8.1 Ni 8.1 Ti 6.2 Cr 7.7 S 47.0
					unidentified part 14.9
				EDX	Mn 8.8 Fe 9.1 Ni 9.0 Ti 7.9 Cr 8.7 S 56.5

To determine the crystal structure of as-prepared HESs, powder XRD measurements were carried out and the results are compared in Figure 6.1. Depending on the metal to sulfur ratio near to 1:1 or 1:2, the phases of HESs mainly show orthorhombic (*Pnma*) or pyrite (*Pa*-3) structure. Since the structure details of MS, MS2, MS2-Cu

and MS2-Ti (HESs with equimolar metal) are analyzed in chapter 4, the Rietveld analysis of HESMo as an example for HESs with non-equimolar metal was performed and shown in Figure 6.2. It confirms the predominant Pnma phase with lattice parameters a = 5.489(2) Å, b = 3.404(8) Å, and c = 5.894(1) Å and a unit cell volume = 110.2(4) Å^3.

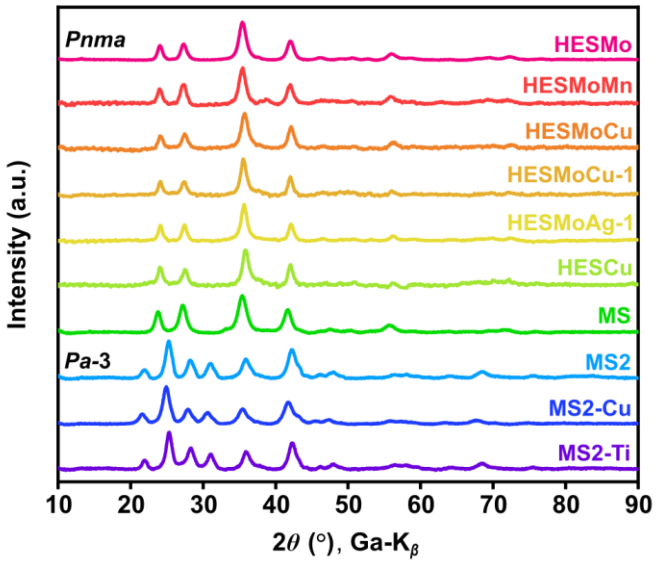

Figure 6.1: Comparison of XRD patterns of HESs with different elemental composition.

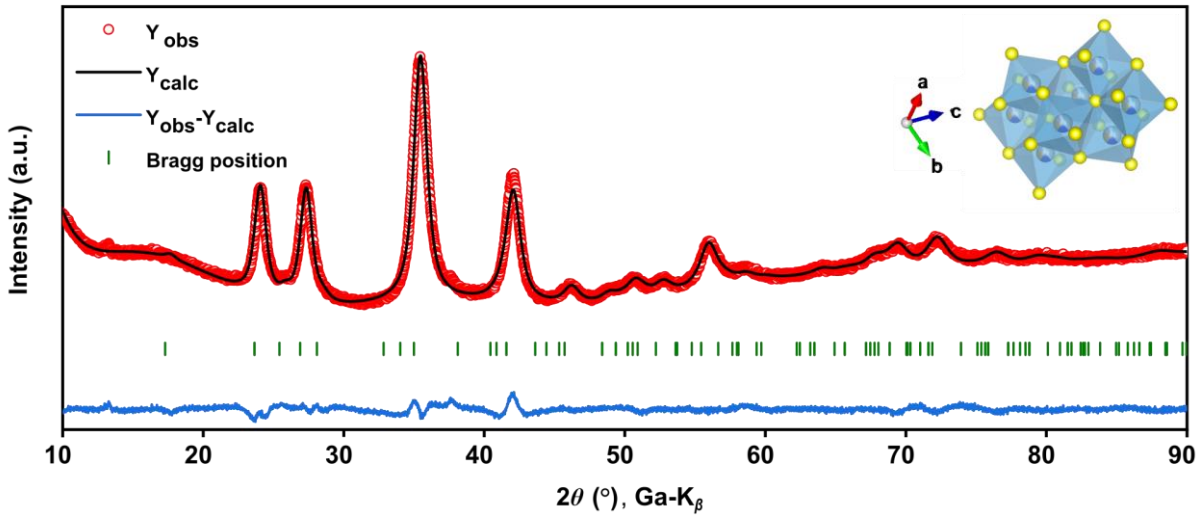

Figure 6.2: Example for the Rietveld refinement of HESMo.

6.2.2. Microstructure

Due to the strong effect of the morphology of catalysts on their catalytic performance,[147] SEM measurements were performed to investigate the morphology of all as-prepared HESs. As shown in Figure 6.3, some small and irregularly shaped particles are distributed on the surface of some relatively large blocks, or some small crystals

are aggregated to form larger particles. Most particles show sizes in the range of a few hundred nanometers. The SEM image of IrO_2 are also presented in Figure 6.3, which is used as commercial reference catalyst for the OER measurement later.

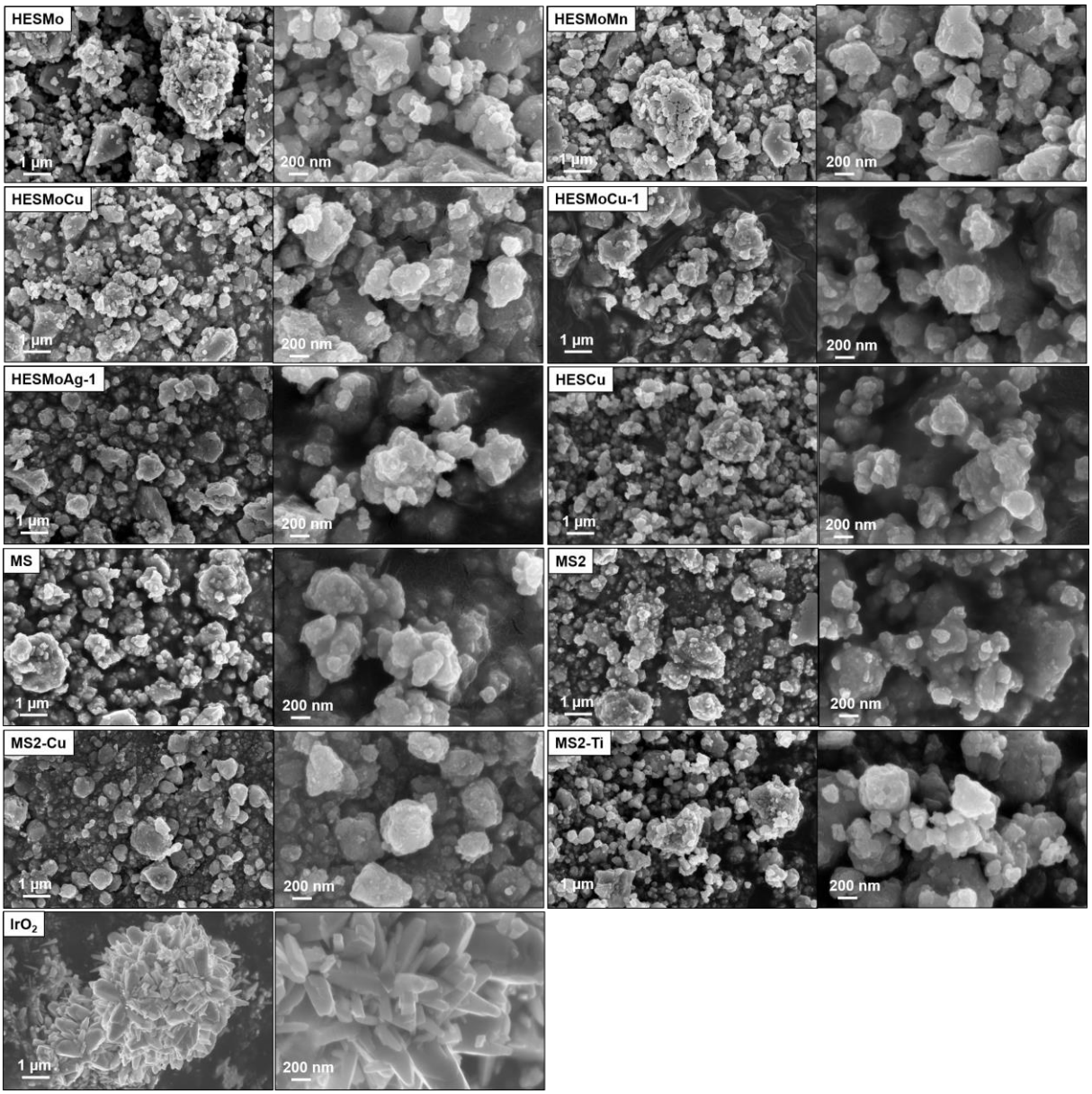

Figure 6.3: Exemplary top-view SEM images of HESs and IrO_2. The right figure for each sample provides a higher magnification view for detailed observation.

To further study the structural details, TEM was carried out for HESMo as an example of as-prepared *Pnma* structured HESs with non-equimolar metal. As HR-TEM images shown in Figure 6.4a, the yellow circled area correspond to lattice plane of (111) in HESMo with *d*-spacing of 0.26 nm. Additionally, to further confirm the crystal structure, SAED measurement of HESMo was also conducted and provided in Figure 6.4b. The diffraction ring indexing is consistent with XRD results and matches well the *Pnma* space group.

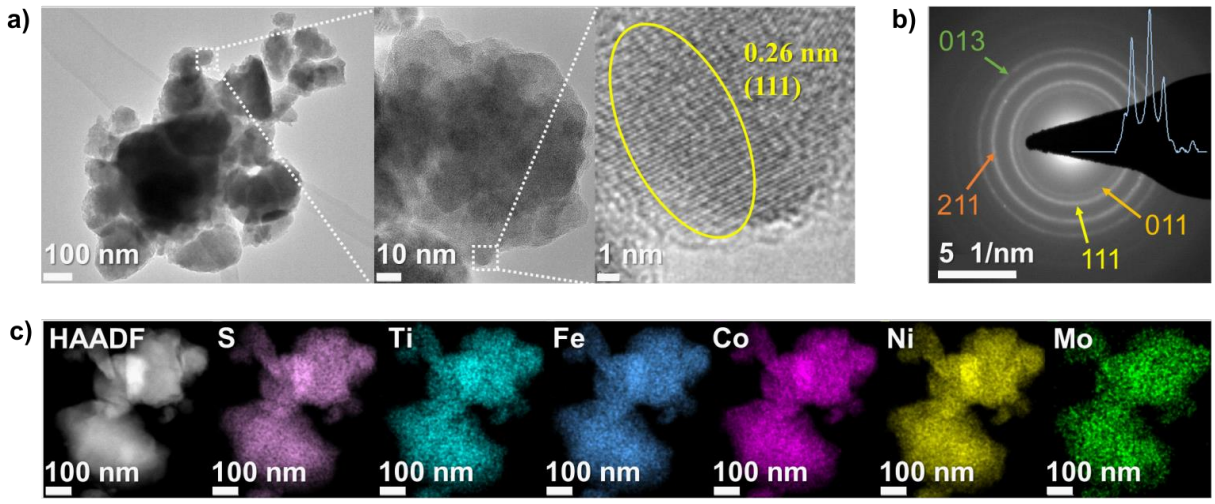

Figure 6.4: (a) HR-TEM micrographs, (b) SAED pattern and (c) STEM-EDX mapping of HESMo. The yellow cycle indicates the (111) lattice plane with *d*-spacing of 0.26 nm.

To investigate the elemental distribution, STEM-EDX mapping of HESs were performed. Since the EDX mapping of MS and MS2 are shown in chapter 4.3.3, Figure 6.5 summarizes the results of the remaining eight HESs. All elements are uniformly distributed at the nanometer scale without obvious segregation or aggregation of individual elements. It implies that all element can act independently as active centers, come in contact with water molecules simultaneously and interact with each other in the process of catalysis.

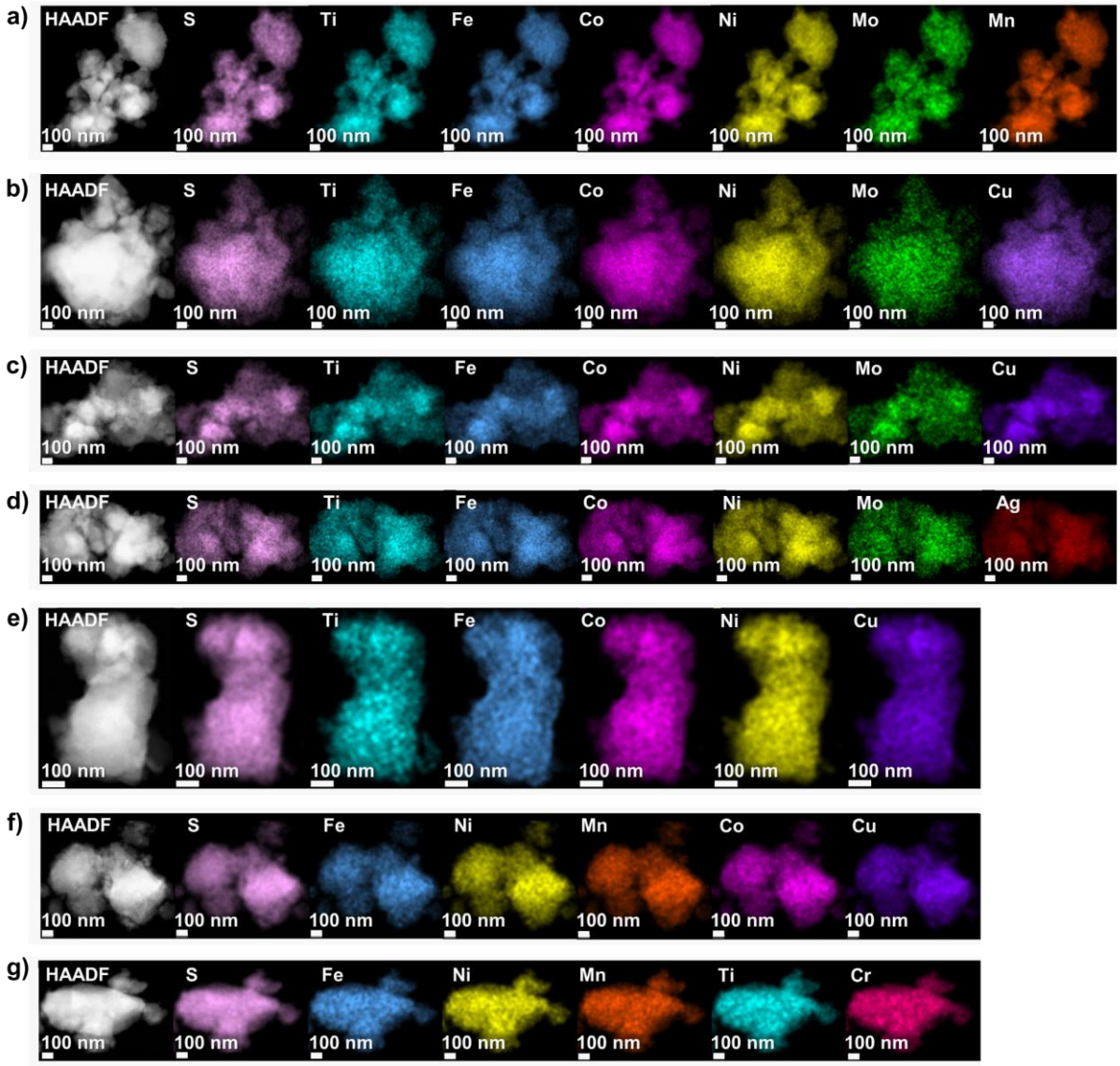

Figure 6.5: STEM-EDX mapping of (a) HESMoMn, (b) HESMoCu, (c) HESMoCu-1, (d) HESMoAg-1, (e) HESCu, (f) MS2-Cu and (g) MS2-Ti. All constituent elements show homogenous distribution.

6.2.3. OER Performance

The OER performance of as-synthesized HESs and the commercial IrO_2 reference was measured in the typical three-electrode system using electrolyte of O_2 saturated 1 mol L^{-1} KOH. For comparison of the catalytic activity among HESs and IrO_2 in OER, linear sweep voltammetry (LSV) was employed to obtain polarization curves as shown in Figure 6.6a and 6.6b. The resulting overpotentials at various current densities have been consolidated in Table 6.2 for reference. The commercial IrO_2 reference necessitates an overpotential of 258 mV to achieve a current density of 1 mA cm^{-2} (defined as the onset), and overpotential of 323 mV to reach 10 mA cm^{-2}, which are comparable to previously published results of IrO_2 in the literature.[148]

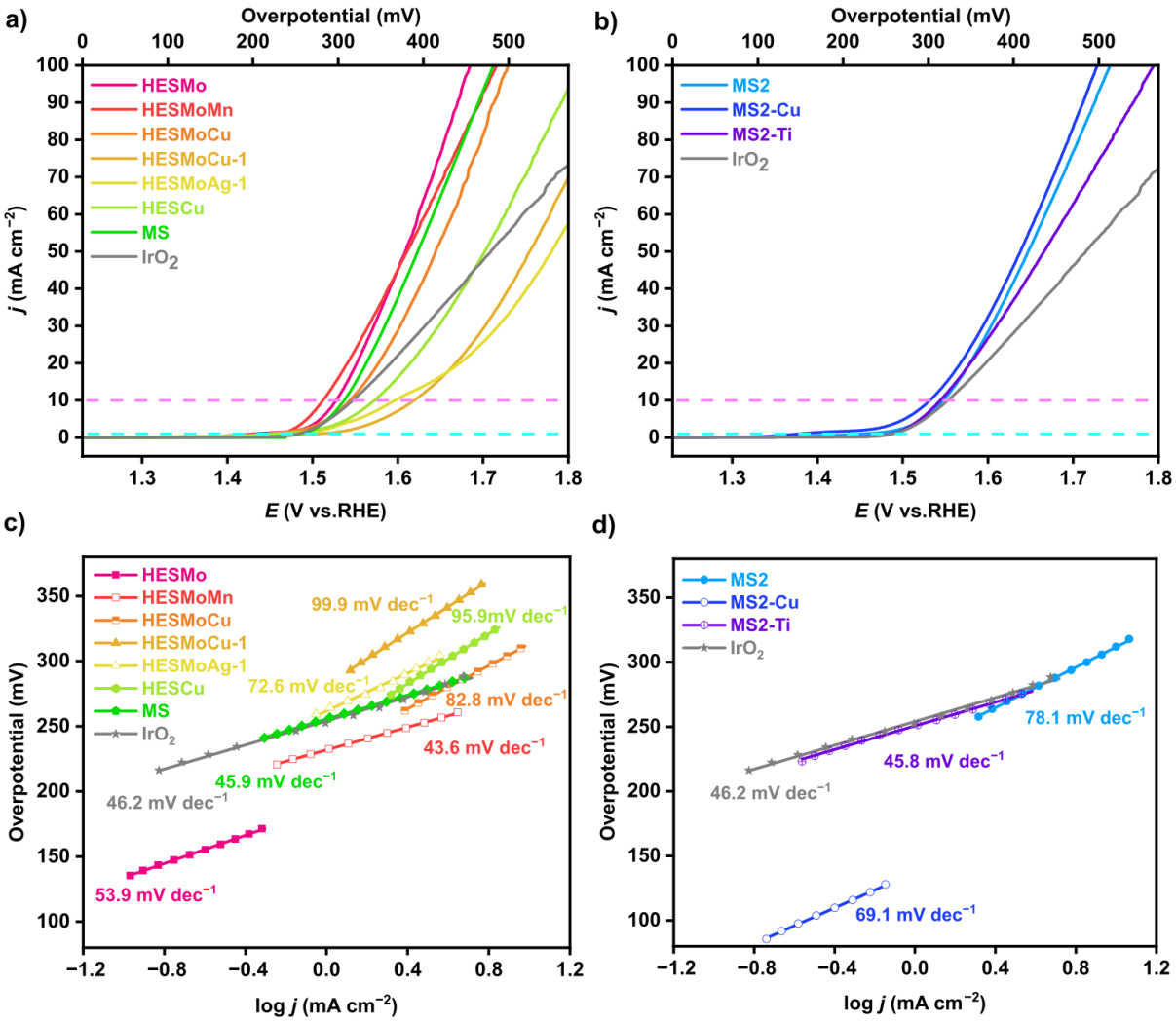

Figure 6.6: OER performance. (a) Polarization curves of *Pnma* structured HESs and IrO_2. (b) Polarization curves of *Pa*-3 structured MS2s and IrO_2. The blue and pink dashed lines mark the values for overpotential at onset and 10 mA cm^{-2}, respectively. (c) and (d) Tafel slopes derived from corresponding polarization curves.

Within the group of *Pnma* structured HESs, the materials MS, HESMoMn, HESMoCu and HESMo display higher catalytic activity than IrO_2 (Figure 6.6a). During the current density in the range of 1.5-45.5 mA cm^{-2}, HESMoMn exhibits the lowest overpotential, e.g. 288 mV at 10 mA cm^{-2}. HESMo demonstrates the most superior overall OER performance with overpotentials of 205, 303, 384 and 460 mV at current densities of 1 (onset), 10, 50 and 100 mA cm^{-2}, respectively. When compared to sample HESCu, HESMoCu shows a much lower overpotential by the introduction of Mo. Similar improvement in performance is also observed in HESMo containing Mo, which indicates that Mo doping in systems with multiple transition metals can enhance the catalytic OER activity. According to a recent report,[149] the coordination of Mo with FeCoNi weakens the bonding of OH* and accelerates the rate-determining step of OH* deprotonation in the OER process, resulting in enhanced OER performance.

While synthesizing, if the Cu precursor is altered from CuS (Cu^{2+}) to Cu_2S (Cu^{1+}), i.e. HESMoCu to HESMoCu-1, the overpotential of the transformed material HESMoCu-1 undergoes a substantial increase. Similar findings have been reported for copper oxides by Deng et al in 2016.[150] Compared to Cu and Cu_2O, CuO and $Cu(OH)_2$

exhibit nearly 10 times higher catalytic efficiency for OER, mainly due to the specialized presence of metastable Cu^{3+} species on the surface of CuO and $Cu(OH)_2$, which could be regarded as catalytically active species. Interestingly, HESMoAg-1 show similar inferior catalytic activity. It can be speculated that the addition of the +1 metal cations Cu or Ag results in a considerable decrease of OER performance. Additionally, to evaluate the OER reaction kinetics, Tafel slopes are calculated using the polarization curves as plotted in Figure 6.6c. Compared to IrO_2 with a Tafel slope of 46.2 mV dec^{-1}, HESMoMn and MS display smaller Tafel slopes of 43.6 mV dec^{-1} and 45.9 mV dec^{-1}, respectively. A smaller Tafel slope indicates that a smaller change in overpotential can lead to a faster increase in current density, and hence, the higher catalytic OER performance.

All *Pa*-3 structured HES2s show smaller overpotentials compared to IrO_2 (Figure 6.6b). MS2-Cu, the most efficient catalyst, requires overpotentials of 148, 302, 408 and 498 mV to reach the current densities of 1 (onset), 10, 50 and 100 mA cm^{-2}, respectively. Substituting Co with Ti, i.e. MS2-Ti, results in slightly higher overpotentials than the other HES2s. This observation may be attributed to the lack of a synergistic effect between Ti and other transition metals, such as Fe.[151] In contrast, Co-Fe catalysts are acknowledged for their synergistic effect.[152]

Table 6.2: Comparison of the OER activity of HESs and IrO_2 (Red and blue values represent improved and lower performance than IrO_2, respectively).

Electrocatalyst	Overpotential (mV)				Tafel slope (mV dec^{-1})
	Onset @1 mA cm^{-2}	@10 mA cm^{-2}	@50 mA cm^{-2}	@100 mA cm^{-2}	
HESMo	205	303	384	460	53.9
HESMoMn	237	288	386	491	43.6
HESMoCu	225	319	420	504	82.8
HESMoCu-1	281	395	530	/	99.9
HESMoAg-1	268	372	556	/	72.6
HESCu	221	348	477	/	95.9
MS	261	313	399	488	45.9
MS2	224	317	417	513	78.1
MS2-Cu	148	302	408	498	69.1
MS2-Ti	256	314	436	564	45.8

In contrast to the impact of the transition metal composition, the metal-sulfur ratio is found to have a small influence on the catalytic activity, as demonstrated by the comparison of MS and MS2. Both materials have similar morphology and metal composition with mostly 2+ oxidation states (excluding Fe and Cr), differing only in the proportion of sulfur anions (S^{2-} and S_2^{2-}, in chapter 4.3.4). MS (M:S = 1:1) exhibits lower Tafel slope and slightly lower overpotential than MS2 (M:S = 1:2) above the current densities of 5 mA cm^{-2}. Therefore, it is presumed that the higher proportion of metal cations contributes to catalytic activity.

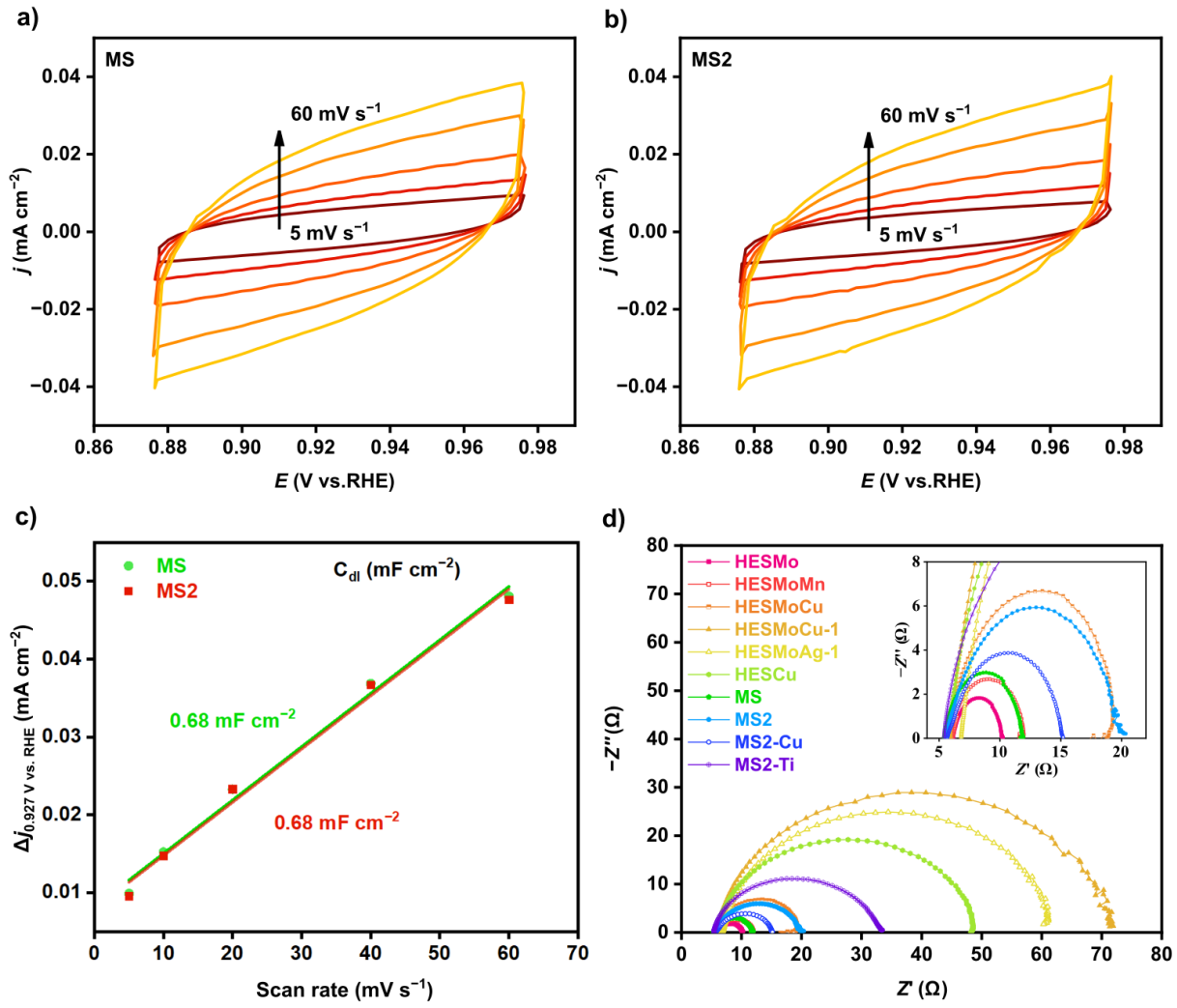

Figure 6.7: CV curves at different scan rates (5, 10, 20, 40, and 60 mV s^{-1}) of (a) MS and (b) MS2. (c) Current density differences (Δj) of MS and MS2 from CV curves plotted against the scan rate. The C_{dl} is equivalent to linear slope. (d) EIS spectra of all HESs in a three-electrode cell with an O_2-saturated 1M KOH electrolyte.

Because the catalytic OER process mainly occurs on the surface of the catalyst, the electrochemical active surface area (ECSA), which might be influenced by crystal structures, plays a crucial role during reaction. The ECSA was estimated based on the double layer capacitance (C_{dl}), the detailed method can be found in chapter 3.3. The C_{dl} was determined by CV in the non-Faradaic region for *Pnma* structured MS and *Pa*-3 structured MS2 (Figure 6.7a and 6.7b). As a result, both MS and MS2 have nearly the same C_{dl} of 0.68 mF cm^{-2} and ECSA of 17 cm^2 (Figure 6.7c), despite having different microscopic crystal structures. This implies that the difference in crystal structure here has a negligible effect on ECSA, and the OER activity is primarily determined by the elemental composition, especially when the morphology is similar.

To provide a further explanation for the effect of different HESs on OER performance, electrochemical impedance spectroscopy (EIS) measurements were carried out on all samples and plotted in Figure 6.7d. The charge transfer resistance (R_{ct}) of materials could be compared by the semicircles in the Nyquist plots at lower frequencies. Among all as-prepared HESs, HESMo displays the smallest semicircle, indicating the smallest R_{ct} and the quickest

charge transfer, which further accounts for the observed superior OER performance. Among HES2s materials, MS2-Cu exhibits the lowest R_{ct} value, which also lead to the higher OER activity. If we now compare the effects of the M to S ratio from EIS results, MS shows a smaller semicircle compared to MS2, implying a faster charge transfer during catalytic process and therefore further explain the better OER activity of MS.

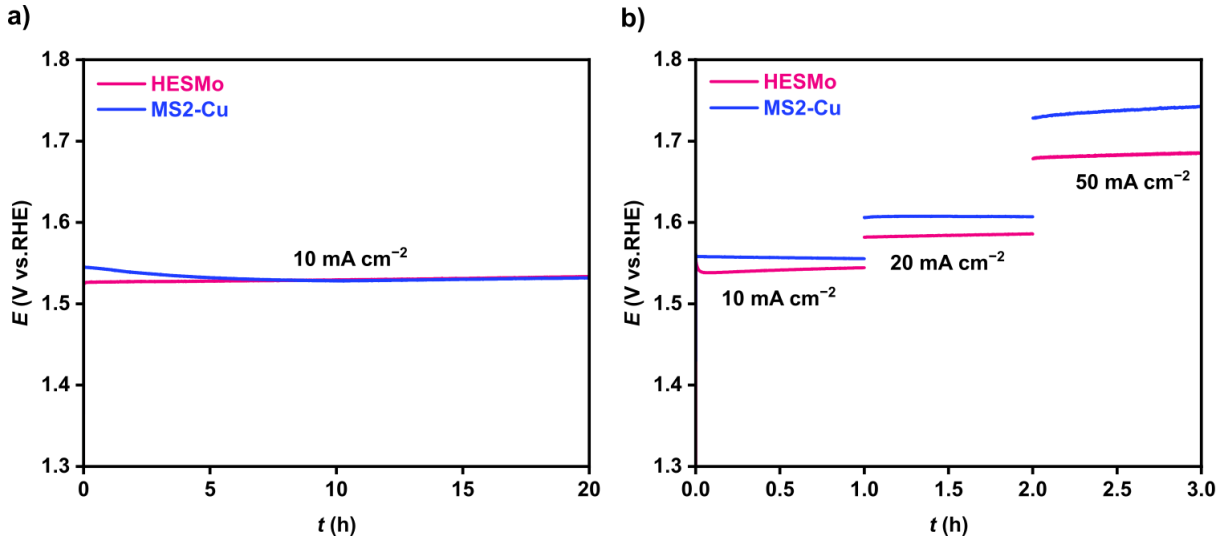

Figure 6.8: (a) Chronopotentiometry of HESMo and MS2-Cu for 20 h at 10 mA cm^{-2}. (b) Multi-step chronopotentiometry of HESMo and MS2-Cu at current densities of 10, 20 and 50 mA cm^{-2}.

To estimate the durability of HESs, the two *Pnma* structured HESMo and *Pa*-3 structured MS2-Cu with best performance were measured using chronopotentiometry. The *E-t* curves shown in Figure 6.8a indicate that HESMo exhibits a remarkably small increase in potential, only 7 mV, after keeping constant current of 10 mA cm^{-2} for 20 h. The overpotential of MS2-Cu initially experiences a decrease of 17 mV for the first 10 h and subsequently increases by 4 mV over the remaining 10 h. The negligible changes observed in the E-t measurement for both HESMo and MS2-Cu suggest that they exhibit good stability as OER catalysts in alkaline conditions. In addition to the above long time measurement, rate-based stability was also investigated by continuous multi-step chronopotentiometry at current densities of 10, 20, 50 mA cm^{-2} (Figure 6.8b). When the applied current density increases gradually, both HESMo and MS2-Cu show an increase in overpotential but quickly reach a plateau, which demonstrates the good rate capability of HESs. The observed stability of the catalysts may be partly attributed to the high entropy effect, which can help stabilize the catalyst structure and thus contribute to the overall improved stability of catalysts during reaction.[60]

Furthermore, to compare the influence of anions on OER catalytic performance, the polarization curves of rock-salt structured HEO-7M and LiHEOF-7M were performed and compared with IrO_2 shown in Figure 6.9. With the same seven incorporated metals Zn, Ni, Co, Mn, Fe, Cu, Mg, the LiHEOF-7M displays lower overpotentials of 371 mV at onset and 409 mV at 10 mA cm^{-2}, compared to HEO-7M with overpotentials of 401 mV at onset and 459 mV at 10 mA cm^{-2}. The improved OER activity of LiHEOF-7M might be attributed to the ability to adjust the electronic state of catalysts through the incorporation of multiple anions. However, it is noteworthy that both

samples show lower OER activity than IrO_2 as well as most HESs, indicating that rock-salt structured high entropy oxides and oxyfluorides prepared via similar mechanochemical methods are less promising as non-noble metal catalysts compared to HESs.

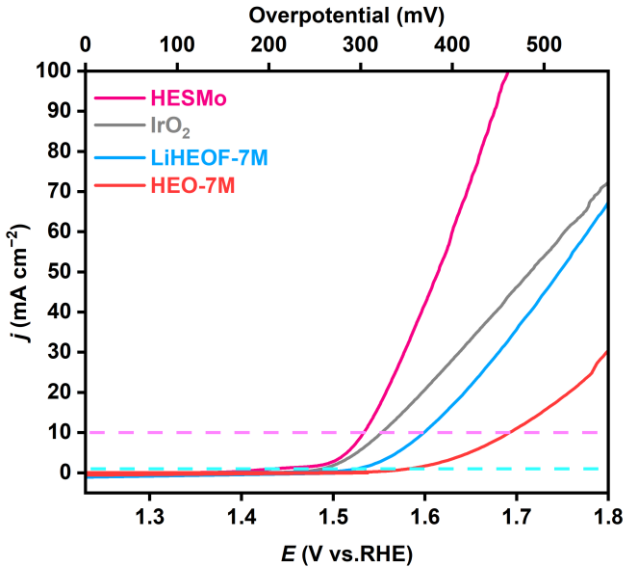

Figure 6.9: Polarization curves of HESMo, IrO_2 reference, rock-salt structured HEO-7M and LiHEOF-7M. The blue and pink dashed lines mark the values for overpotential at onset and 10 mA cm^{-2}, respectively

Many transition metal sulfides are known to work as "pre-catalysts". The surface could be activated by electrochemistry, leading to a self-reconstruction process where truly catalytically active oxides/hydroxides are generated. This process contributes to the improvement of the amount and activity of the surface active sites, thus enhance the OER performance.[153,154] The HES materials most likely serve as "pre-catalysts" as well. Additionally, due to the existence of various incorporated elements in high-entropy materials, the adjustability of composition and surface electronic structure offers a vast number of possible atomic configurations on the surface of catalysts.[76] As indicated in previous studies,[27,28,76] during the process of OER in an alkaline condition, metal sulfides M-S and amorphous sulfates on surface will react with hydroxyl radicals to generate metal hydroxide M-OH and sulfate anions. Subsequently, M-OH adsorbs more OH^- to produce the intermediate metal oxide M-O, which can further convert to metal oxide hydroxide M-OOH. Afterwards, MOOH-S or the MOOH containing sulfate will break down into the free active site and oxygen. In this process, the interaction between metals and sulfur and the synergy of multiple metals (referred to as the "cocktail effect") regulate the charge state and lead to improvement of OER catalytic activity and stability.[60,76,155]

The utilization of HES as OER catalysts has the potential to avoid the usage of noble metals in catalysts, such as Ir in IrO_2, resulting in cost-effective high-performance materials with remarkable OER performance. In fact, the HESs investigated in this chapter are mostly devoid of noble metals, but still exhibit superior catalytic activity when compared to IrO_2. Figure 6.10 provides an intuitive comparison of their catalytic activity, where warmer colors represent higher current densities (indicating better activity) at specific overpotentials, while the

corresponding current intensities are displayed in the right small diagram. Among the ten HES samples vertically listed in the figure, seven of them outperform noble metal OER catalyst IrO_2 at the overpotential of 400 mV.

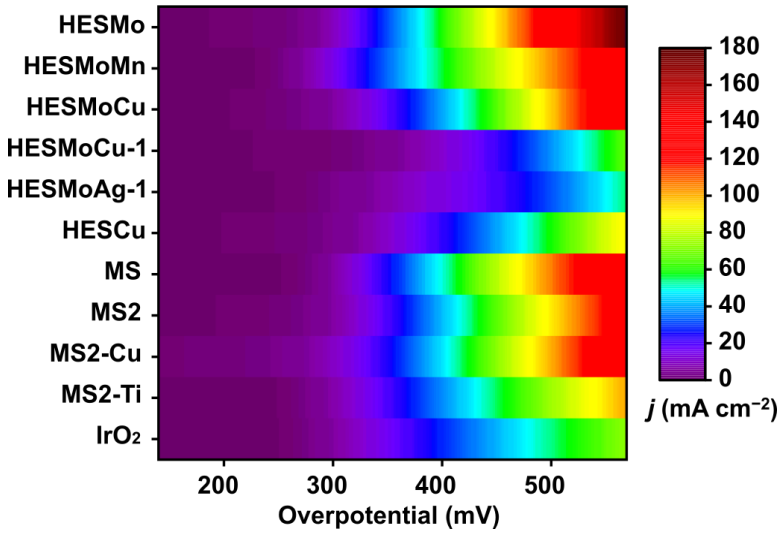

Figure 6.10: Comparison of current densities (*j*) among the HESs and IrO_2. Seven HES samples outperform IrO_2 at the overpotential of 400 mV.

Earlier research on the use of HES as OER catalysts involved different types of self-supporting substrates (such as Ni foams, carbon sheets, and PET films with silver paste) as working electrodes,[60,76,77] which can also enhance the OER performance. To enable a more direct comparison with other previously reported materials, all as-synthesized HESs were measured via three-electrode setup using a standard glassy carbon working electrode. The OER performance of HESMoMn was compared with that of some other transition metal sulfides reported in the literature, and the results are summarized in **Table S2**.

Table 6.3: Comparison of OER performance among HESMoMn and some reported transition metal sulfides or derivatives with glassy carbon working electrode in alkaline media.

Catalysts	Overpotential [mV] @10 mA cm^{-2}	Tafel slope ($mV\ dec^{-1}$)	Reference
$TiFe_2Co_2Ni_3MoMn_2S_{12}$	288	43.6	This work
hierarchical porous Ni_3S_4	307	67	[156]
CoS/CNT composite	330	142	[157]
Mo–N/C@MoS_2	390	72	[158]
3% Ni-doped CuS	390	96.8	[159]
$CuCo_2S_4$ nanosheets	310	86	[160]
$Ni_{1.29}Co_{1.49}Mn_{0.22}S_4$	348	65	[146]
$Co_{1-x}Ni_xS_2$–graphene composite	330	47	[161]
$FeNiS_2$ nanosheets	310	46	[162]
Ti–Fe mixed sulfide nanoboxes	350	55	[163]

6.3. Conclusion

Six new non-equimolar HESs and four equimolar HESs were successfully designed, synthesized via a simple mechanochemical synthesis. The structure and morphology of ten as-prepared HESs containing 5-6 transition metals are studied by XRD, ICP-OES, SEM, TEM and EDX. The OER catalytic performance of HES powders with various compositions and structures is compared by measuring in a standard three-electrode configuration. Most of HESs show an improved OER performance compared to IrO_2 in alkaline medium, which could be considered as competitive non-noble metal catalysts. The incorporation of Mo was found to significantly improve the catalytic performance. The introduction of metal cations with a +1 charge such as Cu^+ or Ag^+ leads to a significant reduction of OER performance. Additionally, with the same composition, the OER catalytic activity of *Pnma* structured MS (M:S ≈ 1:1) is compared with that of *Pa*-3 structured MS2 (M:S = 1:2). The stability of the two HES structure types in alkaline electrolytes is observed to be good by chronopotentiometry. Among different anionic high entropy compounds, sulfides show more promising performance than oxides and oxyfluorides. The cocktail effects of multiple metals, interaction between metal and sulfur, and tunability of the electronic state contribute to the improved OER performance of HES catalysts. In general, the HESs as a novel class of catalysts show their suitability and potential for future OER electro-catalytic development.

Chapter 7

7. High Entropy Sulfides as Electrocatalysts for Hydrogen Evolution Reaction

Major parts of the results in this chapter are ready for submission.

7.1. Introduction

Hydrogen, with its clean and renewable nature, offers an ideal alternative to fossil fuels in various industries and applications, such as transportation, manufacturing, and power generation, enabling the transition towards a sustainable energy future. Electrochemical water splitting to produce hydrogen gas is considered a clean and promising method that has received widespread attention in recent years.[164] The process of electrochemical water splitting comprises two reactions: HER occurring at the cathode and OER at the anode. Developing efficient and low-cost catalysts to reduce energy consumption during the process of water electrolysis is crucial for the industrialization of this process.

So far, Pt-group elements remain the most effective HER electrocatalysts, but the high cost and limited earth abundance hinder their widespread commercial use. Therefore, much attention has shifted to abundant non-precious metal electrocatalysts, such as Ni, Co, Fe and Mo, as alternative materials.[17] However, there are also some problems with non-precious metal catalysts, such as the corrosion under strong acid or base conditions and the tendency to agglomerate into larger particles during the catalytic process. It's a challenge to improve the stability of non-precious metal catalysts without sacrificing catalytic performance.

Very recently, multi-transition metal-based HESs have been studied as promising catalysts for water electrolysis. In 2022,[77] Lei et al reported the good catalytic activity and stability of carbon-supported CoZnCdCuMnS@CF for overall water splitting in alkaline medium. It is also the first study related to the application of HESs as HER electro-catalysts. The unique structure and highly tailorable electrochemical property of HESs are expected to attract growing interest in electrocatalytic applications.

Herein, new HESs are designed for HER application, successfully synthesized by high energy ball-milling process, and characterized in detail. Several HESs with different structure or composition are investigated and compared as HER electro-catalysts. The impact of the cocktail effect is explored in terms of structure and catalytic performance. The high entropy effect is studied by comparison with medium entropy sulfide. Additionally, the HER performance of HEO, LiHEOF and Pt/C are measured for comparison. This work contributes to more HES as promising catalysts for future HER applications.

7.2. Results and Discussion

In this character, two new HESs with *Pnma* (MS-Mo) and *Pa*-3 (MS2-Mo) structures are designed by introducing Mo followed by an investigation as catalysts for HER electro-catalysis. The structure details, morphology and chemical state of these novel HESs are studied using ICP-OES, XRD, TEM, EDX and XPS. Moreover, two new HESs, four previously studied HESs (MS, MS2, MS2-Cu, MS2-Ti), medium entropy sulfide 4MS2, commercial MoS_2 (the Mo source for synthesizing two new HESs), commercial Pt/C, HEO-7M and LiHEOF-7M are compared as HER catalysts in alkaline conditions.

7.2.1. Composition and Structure

A well-known promising catalyst for HER is MoS_2. Given MoS_2's established application as a catalyst for HER and its distinctive layered structure that offers additional active sites, novel catalyst materials were designed by incorporating Mo into existing HESs. The synthesis employed a straightforward high-energy ball-milling method under an inert atmosphere, resulting in the successful synthesis of two novel HESs with distinct structures. These HESs consist of five transition metals—Fe, Mn, Ni, Co, and Mo—in equal molar ratios. To determine the exact composition of two new HESs, ICP-OES was carried out. One sample shows the composition of $(Fe_{0.172}Mn_{0.164}Ni_{0.169}Co_{0.181}Mo_{0.168})S_1$, named as MS-Mo. Another sample shows the composition of $(Fe_{0.100}Mn_{0.101}Ni_{0.097}Co_{0.098}Mo_{0.097})S_1$, named as MS2-Mo.

For crystal structure determination, the XRD measurement was performed. Figure 7.1 provides the comparison for XRD patterns of all as-prepared sulfides which are measured as HER catalysts in this chapter. The phase of the new HES materials MS-Mo and MS2-Mo show almost a pure *Pnma* or *Pa*-3 crystal structure, which is related to the ratio of metal and sulfur near to 1:1 or 1:2. The *Pa*-3 structure is also the main phase for medium entropy disulfides 4MS2, but a few impure peaks from secondary phase are detected.

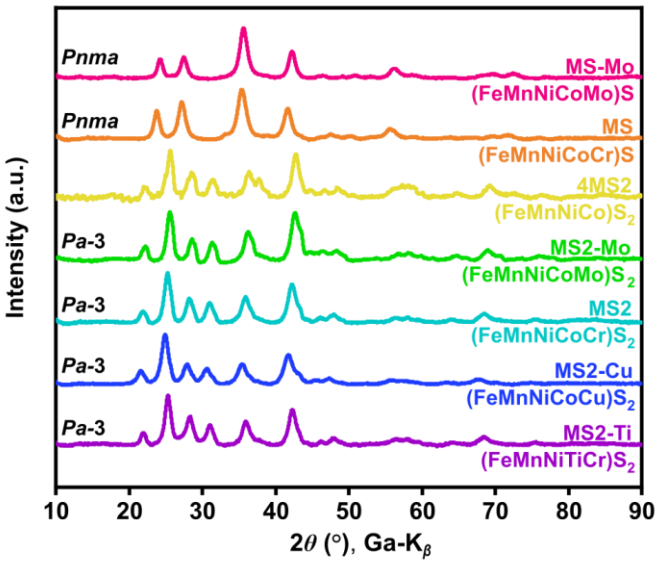

Figure 7.1: Comparison of XRD patterns of all as-synthesized sulfides used as HER catalysts. The data is background corrected.

Rietveld refinement of MS-Mo and MS2-Mo is shown in Figure 7.2. The result of MS-Mo confirms *Pnma* phase and a unit cell with volume of 108.8(3) Å^3 and lattice parameters of a = 5.462(2) Å, b = 3.388(5) Å, c = 5.876(1) Å. Refinement of MS2-Mo XRD pattern indicates the pure *Pa*-3 phase with unit cell volume = 181.8(4) Å^3 and a = 5.666(4) Å.

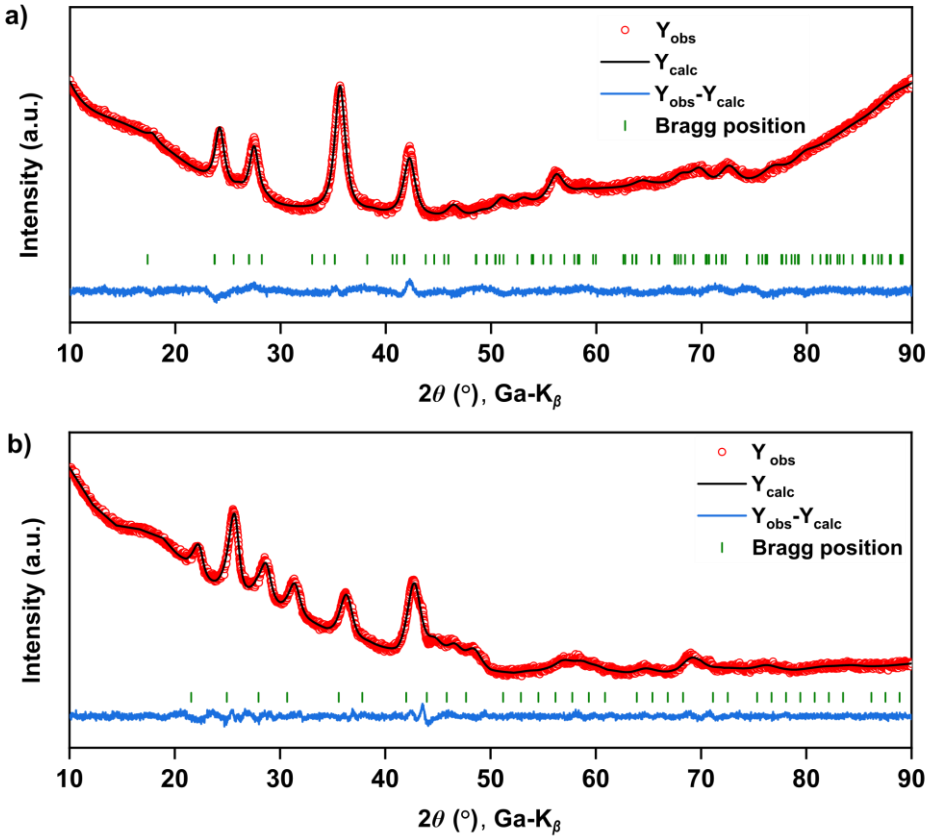

Figure 7.2: Rietveld refinement of (a) MS-Mo and (b) MS2-Mo.

The Mo-precursor for the synthesis process is commercial MoS_2, showing mainly *P*63/*mmc* structure in XRD pattern (Figure 7.3). MoS_2 is known to appear in two different structures, one belonging to a hexagonal crystal system (2H-MoS_2) and the other to a trigonal crystal system (3R-MoS_2).[165] Another reported structure belongs to tetragonal crystal system (1T-MoS_2), but it appears to be metastable and it is difficult to be prepared on a large scale by conventional methods. Nevertheless, due to a high electrical conductivity, 1T-MoS_2 is an attractive electro-catalyst for HER.[166] Interestingly, Mo could be incorporated perfectly into a *Pnma* (orthorhombic crystal system) and *Pa*-3 (cubic crystal system) high-entropy material, although *Pnma* and *Pa*-3 structures haven't been found for molybdenum sulfide before. Thus, high-entropy materials show significant potential for such catalysts, since with this approach Mo can be included in different and unusual structures, forming until now unknown materials with individual properties.

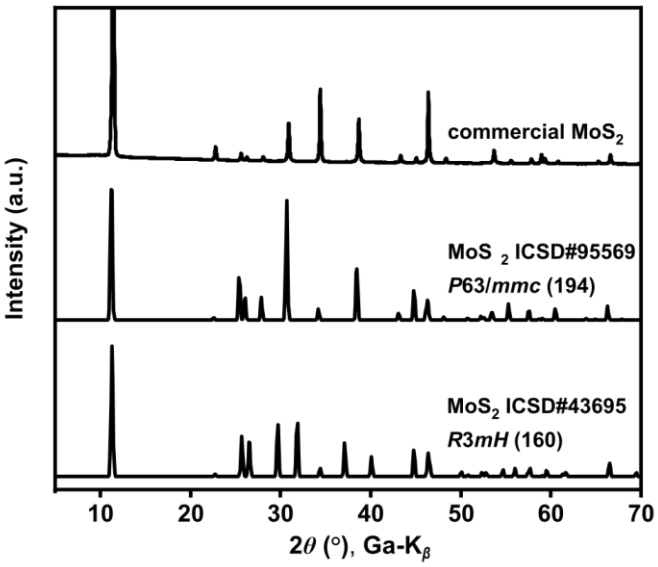

Figure 7.3: XRD pattern of MoS_2.

7.2.2. Microstructure

To further investigate the structural details and the morphology of MS-Mo and MS2-Mo, TEM analysis was performed. TEM micrographs in Figure 7.4 reveal irregularly shaped particles with sizes ranging in the hundreds of nanometers. The relatively large surface area of the nanoparticles facilitates more exposure of catalytic active sites to the electrolyte.

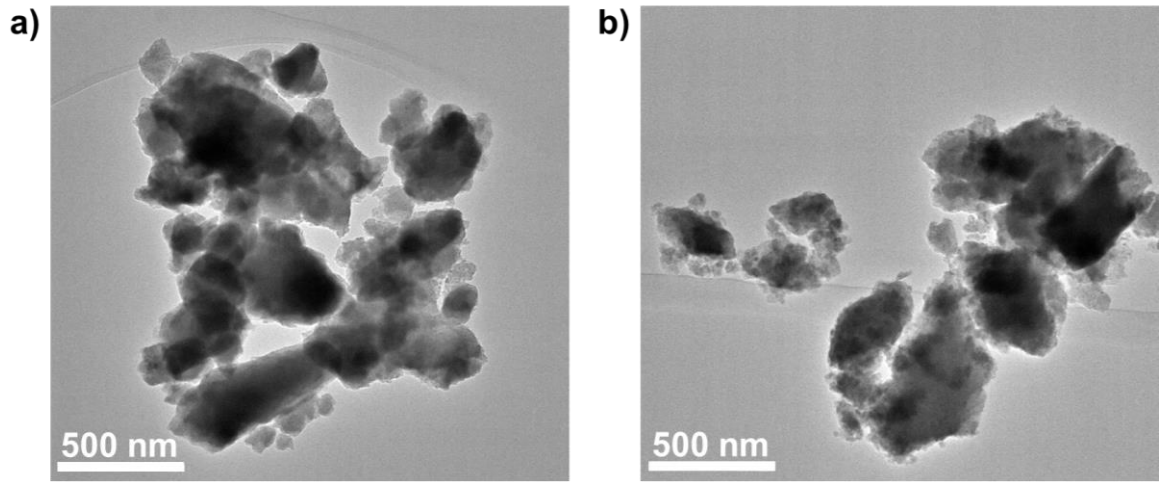

Figure 7.4: TEM images of (a) MS-Mo and (b) MS2-Mo.

To gain further insight into the crystal structure, SAED patterns were measured on powder particle (Figure 7.5). The diffraction rings observed in MS-Mo and MS2-Mo are consistent with the space group of *Pnma* and *Pa*-3, respectively, which is in general agreement with the XRD data (Table 7.1).

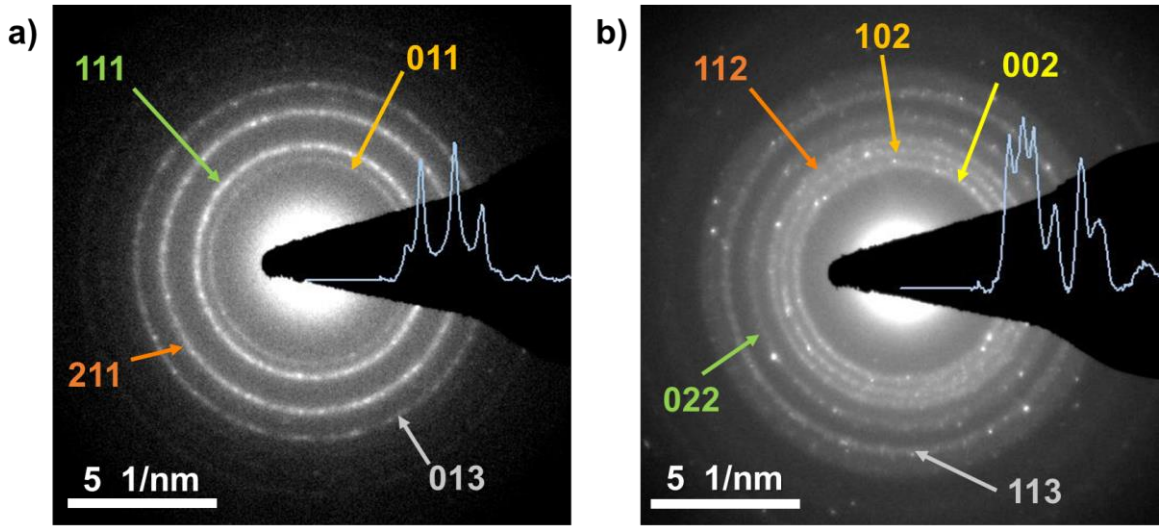

Figure 7.5: SAED pattern of (a) MS-Mo and (b) MS2-Mo. The diffraction rings observed for MS-Mo and MS2-Mo are consistent with the space group of *Pnma* and *Pa-3*, respectively.

Table 7.1: *d*-spacing comparisons of SAED and XRD for MS-Mo and MS2-Mo

MS-Mo reflection	011	111	211	013
d-spacing measured by SAED (nm)	0.293	0.260	0.200	0.170
d-spacing measured by XRD (nm)	0.288	0.255	0.197	0.168

MS2-Mo reflection	002	102	112	022	113
d-spacing measured by SAED (nm)	0.276	0.247	0.226	0.195	0.167
d-spacing measured by XRD (nm)	0.273	0.245	0.224	0.194	0.166

HR-TEM micrographs and the corresponding fast Fourier transform (FFT) images of MS-Mo and MS2-Mo are shown in Figure 7.6, indicating the good crystallinity of HES particles. In the higher magnification of the region demarcated by the white square, the red circled area corresponds to lattice planes of (111) in *Pnma* structured MS-Mo with lattice spacing of 0.26 nm, the blue circled area refers to (002) lattice plane in *Pa*-3 structured MS2-Mo with spacing of 0.27 nm. Additionally, compared to HR-TEM images of MS-Mo (Figure 7.6a), MS (Figure 4.16a) and MS2 (Figure 4.16b), MS2-Mo displays another feature, indicating a layered structure of the material (some layers marked with a yellow arrow in Figure 7.6b). The yellow lines refer to stacked MS2-Mo with an interlayer distance of 0.62 nm, which is similar to HR-TEM results of layer MoS_2 nanosheets in literature.[167] The corresponding FFT patterns generated from the region of HR-TEM micrographs confirm the *Pnma* phase of MS-Mo and the *Pa-3* phase of MS2-Mo. Furthermore, the yellow ring in the center ring of the FFT pattern of MS2-Mo corresponds to the spacing of 0.62 nm and 2θ of 11.2° in Ga-jet XRD pattern, which is barely detectable by XRD. It is interesting that with the introduction of Mo the HES maintains a *Pa*-3 structure while simultaneously incorporating a layered structure from MoS2, nicely showing the cocktail effect of HEMs.

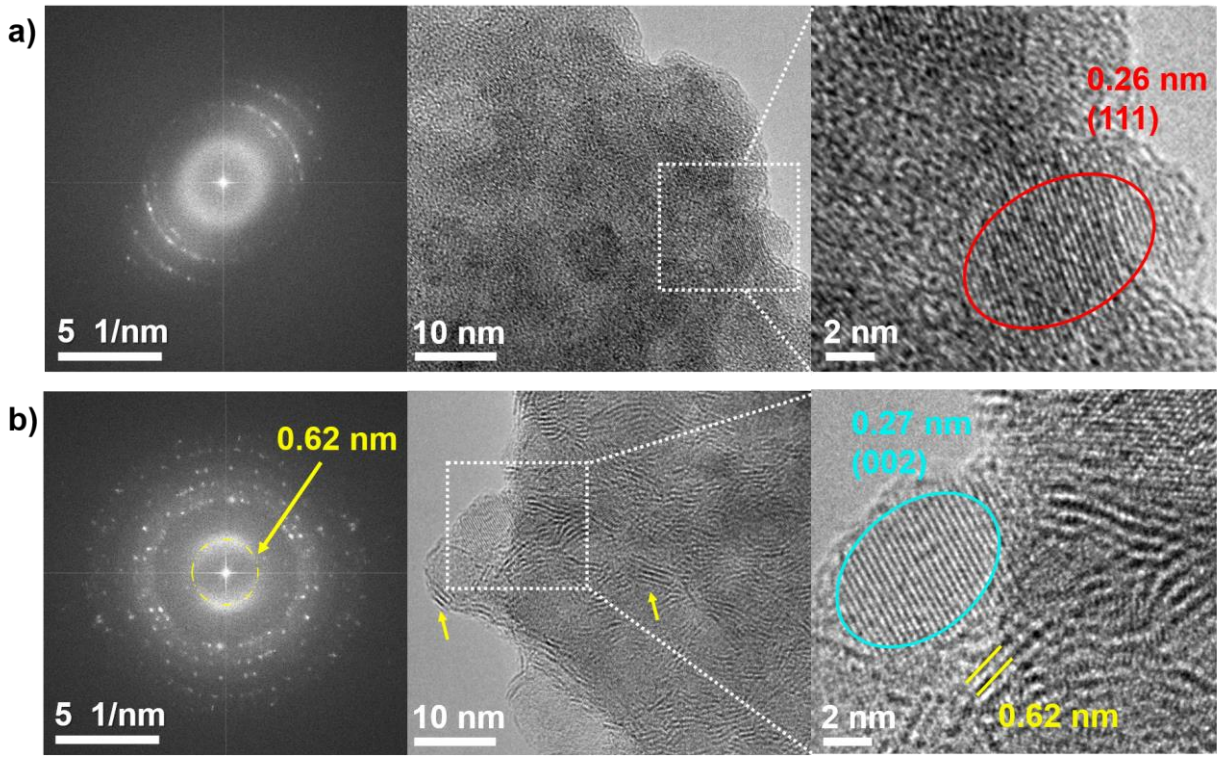

Figure 7.6: HR-TEM image with crystal lattices and corresponding FFT patterns of (a) MS-Mo and (b) MS2-Mo.

STEM-EDX mapping conducted to study the elemental distribution of MS-Mo and MS2-Mo is shown in Figure 7.7. The results indicate that all elements are homogeneously distributed at the nanometer scale, without noticeable segregation or aggregation. This suggests that each element can act independently as active centers, react with electrolytic solution simultaneously, and interact with each other during the catalytic process.

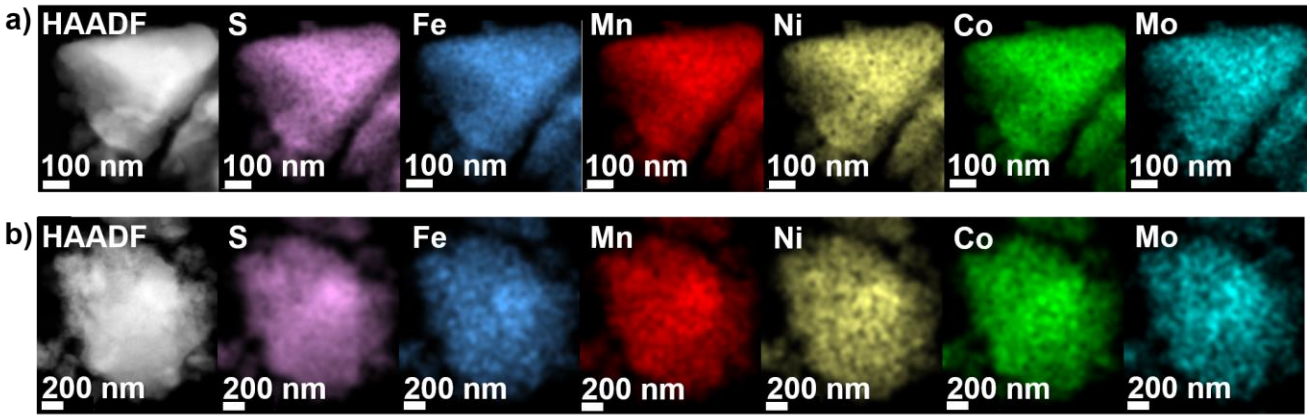

Figure 7.7: STEM-EDX mapping of (a) MS-Mo and (b) MS2-Mo.

7.2.3. Oxidation State

Because the electronic structure has impact on the catalytic properties, the oxidation state of the elements and the elemental composition in the surface region of MS-Mo and MS2-Mo were determined using XPS. Both samples, as indicated by the survey spectra (Figure 7.8), contain several elements on the surface, including manganese (Mn 2p), iron (Fe 2p), cobalt (Co 2p), nickel (Ni 2p), molybdenum (Mo 3d), sulfur (S 2p), carbon (C 1s), and oxygen (O 1s). The detail spectra for individual element regions are provided in Figure 7.8 and 7.9.

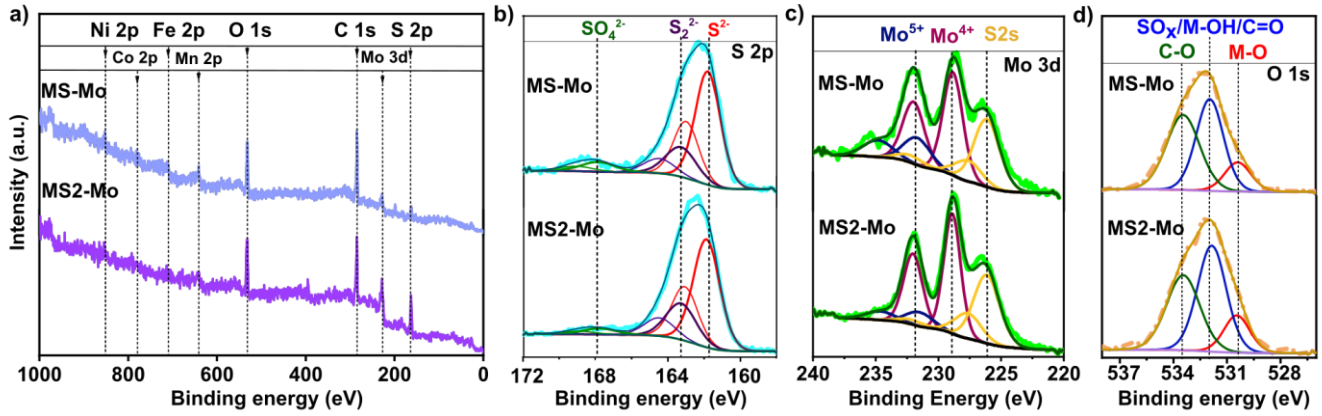

Figure 7.8: (a) Survey XPS spectra and detail spectra in the (b) S2p, (c) Mo3d and (d) O 1s regions of MS-Mo and MS2-Mo.

In the S 2p spectra (Figure 7.8b), both samples display three peak doublets. The sulfide species peak doublet (S^{2-}, S $2p_{3/2}$ at 161.8 eV) dominates in both samples, and smaller contributions at higher binding energy can be assigned to disulfide (S_2^{2-}, S $2p_{3/2}$ at 163.3 eV) and oxidized S species (SO_X, S$2p_{3/2}$ at 167.8 eV). It indicates that the surface of particles contains some oxidized sulfur species. Additionally, the presence of a peak at 530.4 eV in the O 1s spectra of both samples indicates the presence of metal oxide species in the surface region (Figure 7.8d). These species might be formed from a reaction between the surfaces and trace of oxygen during the storage or transfer process to XPS analysis.

In the Mo 3d detail spectra (Figure 7.8c), two Mo species peak doublets are observed, in addition to the S 2s peaks associated with S^{2-}, S_2^{2-} and SO_X. The Mo $3d_{5/2}$ peak doublet observed at 228.7 eV is most likely indicative of the presence of Mo^{4+} species, possibly in the form of sulfide and/or oxide. Moreover, another doublet ($Mo3d_{5/2}$ at 231.5 eV) could be assigned to Mo^{5+} species.[168,169]

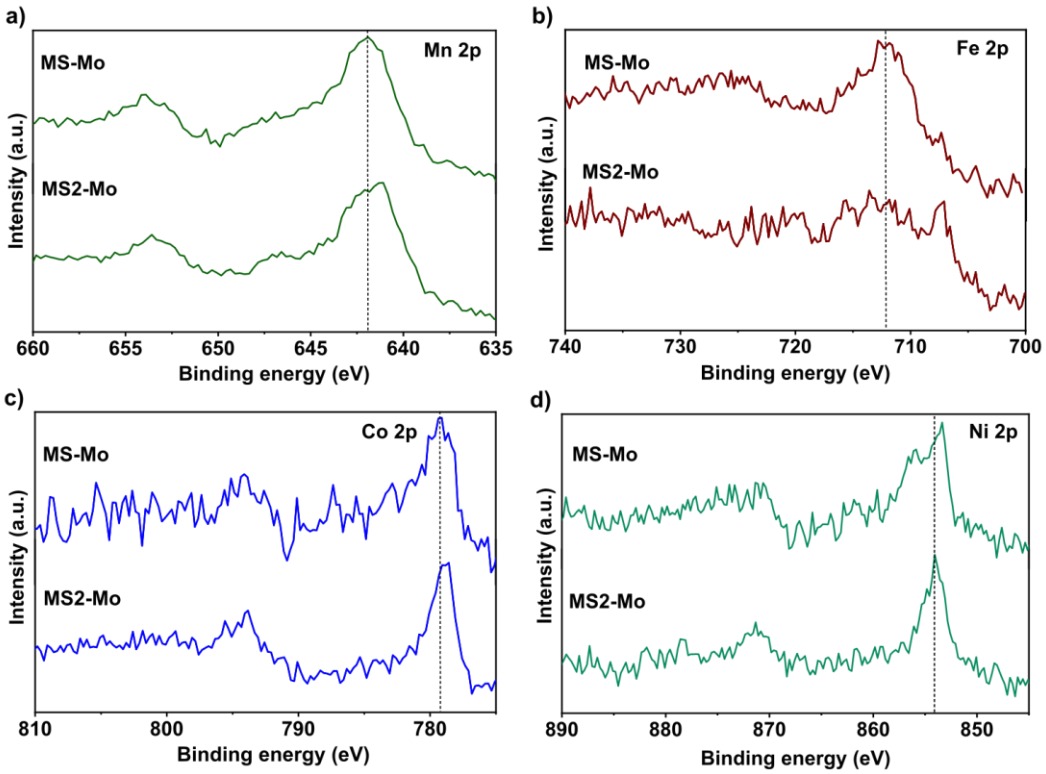

Figure 7.9: XPS detail spectra in the (a) Mn 2p, (b) Fe 2p, (c) Co 2p, and (d) Ni 2p regions of MS-Mo and MS2-Mo.

The analysis of spectra for other transition metals (Mn 2p, Fe 2p, Co 2p and Ni 2p; Figure 7.9) is complex due to multiplet splitting effects.[170] Therefore, a peak fit is not performed, and only a brief discussion of the shape and position of the spectra will be presented. The peak maximum of Mn $2p_{3/2}$ is found at 642.0 eV for MSMo and at 641.3 eV for MS2Mo, suggesting a slight difference in oxidation states of Mn between these two samples. Specifically, MSMo may have Mn^{3+}/Mn^{4+} while MS2Mo may have Mn^{2+}/Mn^{3+}. The main $2p_{3/2}$ peaks for Co and Ni are positioned similarly between MSMo and MS2Mo, with Co $2p_{3/2}$ at ~779 eV and Ni $2p_{3/2}$ at ~ 853.5 eV. The detection of the satellite feature at around 787 eV for Co and the above positions of the main $2p_{3/2}$ peak suggest a preferred oxidation state of +2 for both Co and Ni. The Fe 2p peak doublet shows low intensity and the presence of a Ni Auger feature that overlaps with the Fe $2p_{3/2}$ peak, making it impossible to analyze the results in this region.

7.2.4. HER Performance

The HER performances were measured using the typical three-electrode setup in the electrolyte of N_2-saturated 1 mol L^{-1} KOH. To increase the electronic conductivity, all materials were mixed with carbon black in a weight

ratio of 4:1, which were used as active materials in working electrode. Polarization curves of all samples were performed by LSV and shown in Figure 7.10. The resulting overpotentials required to achieve different current densities have been collected in Table 7.2 for reference.

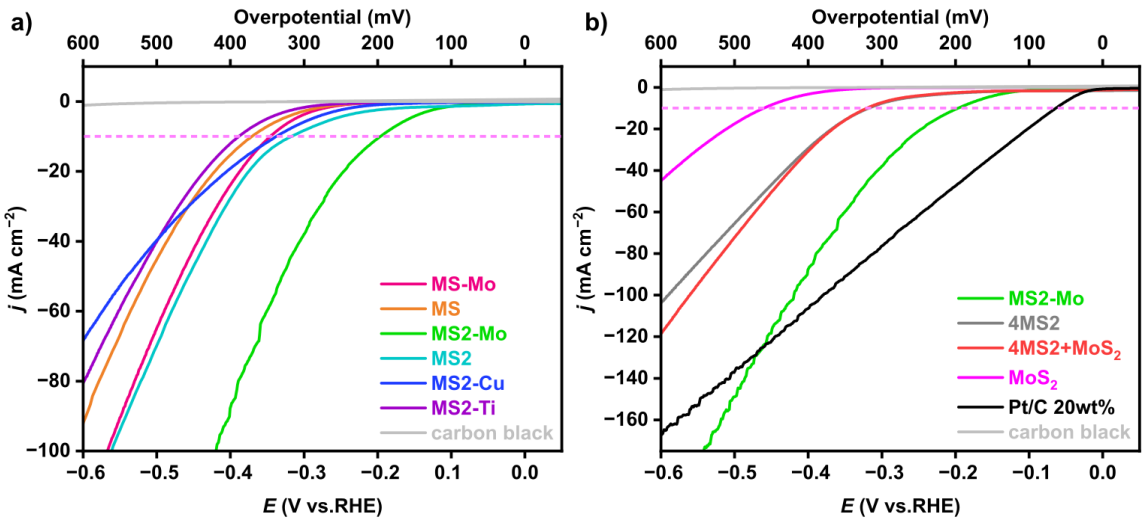

Figure 7.10: Polarization curves of (a) all HESs and (b) MS2Mo, 4MS2, MoS_2 and commercial reference Pt/C in a three-electrode cell with an N2-saturated 1M KOH electrolyte. The pink dashed lines mark the overpotential at current density of –10 mA cm^{-2}.

Table 7.2: Comparison of the overpotentials required to achieve different current densities.

Electrocatalyst	Overpotential (mV)			
	@–10 mA cm^{-2}	@–50 mA cm^{-2}	@–100 mA cm^{-2}	@–150 mA cm^{-2}
MS-Mo	345	467	567	/
MS	370	512	615	/
MS2-Mo	196	331	420	503
MS2	317	457	561	/
MS2-Cu	337	540	/	/
MS2-Ti	388	526	/	/
4MS2	318	458	561	/
4MS2+MoS_2	320	449	560	/
MoS_2	460	615	/	/
Pt/C (20 wt. % Pt)	64	210	380	546

Among all as-prepared HESs (Figure 7.10a), it is obvious that MS2-Mo exhibits the best HER catalytic performance with the lowest overpotential of 196, 331, 420 and 503 mV at current density (*j*) of –10, –50, –100 and –150 mA cm^{-2}, respectively. Compared to *Pnma* structured monosulfides MS-Mo and MS, *Pa*-3 structured disulfides MS2-Mo and MS2 have the same metal composition but show lower over potentials, indicating that HESs with *Pa*-3 structure (M:S = 1:2) is better than those with *Pnma* structure (M:S = 1:1) for HER electro-

catalysts. In comparison among four high entropy disulfides, MS2-Ti displays the worst HER activity probably because of the absence of Co, which has a strong synergistic effect with other transition metals.[152] MS2-Mo shows much higher HER performance than other disulfides, most likely due to the introduction of Mo.

Figure 7.10b show the comparison of HER catalytic performance for the best HES MS2-Mo, medium entropy sulfide 4MS2, commercial MoS_2, a mixture of 4MS2 and MoS_2, commercial Pt/C (20 wt% Pt) reference and carbon black. The carbon black used to improve conductivity displays little catalytic activity, which means it is unable to influence the comparison of HER performance for samples. In comparison to the commercial Pt/C catalyst, MS2-Mo displays a larger overpotential up to a current density of –125 mA cm^{-2}, followed by a lower overpotential thereafter. As mentioned before, the Mo source is not 1T-MoS_2 and thus commercial MoS_2 shows a low HER catalytic performance. The medium entropy sulfide 4MS2, which has same main structure (*Pa*-3) and similar composition (Fe, Co, Ni, Mn, S except Mo) as MS2-Mo, requires significantly larger overpotentials for HER compared to the high entropy sulfide MS2-Mo. Even when 4MS2 is mixed with commercial MoS_2 using conventional methods (such as grinding), the resulting mixture has the same elemental composition and ratio as MS2-Mo, exhibits an overpotential close to 4MS2 but still much higher than MS2-Mo. It can be assumed that the perfect incorporation of all elements, which are uniformly distributed in the lattice, and excellent elemental interaction in high entropy system lead to a significant improvement in catalytic performance of MS2-Mo.

Since the stability under harsh conditions is one critical factor for HER application, the durability of several typical samples was investigated by chronopotentiometry and the results are shown in Figure 7.11a. The potential of medium entropy sample 4MS2 undergoes a significant change in the first two hours (ΔE = 130 mV), compared to high entropy samples MS2-Mo, MS-Mo and MS2. The improved stability of HESs may be due to the high entropy effect, which contributes to structural stability during HER process. Furthermore, with the same *Pa*-3 structure, MS2-Mo (ΔE = 17 mV for 14 h) exhibits much more stable than MS2 (ΔE = 80 mV for 14 h) by incorporating Mo. Interestingly, the *Pnma* structured MS-Mo (ΔE = 38 mV for 14 h), which also contains Mo, shows better stability than MS2, indicating introduction of Mo greatly helps stability of HESs catalysts in an alkaline environment. Additionally, with the same metal composition, the potential of MS2-Mo rises less than MS-Mo, which means that the crystal structure of *Pa*-3 is more favourable to catalyst stability than *Pnma*.

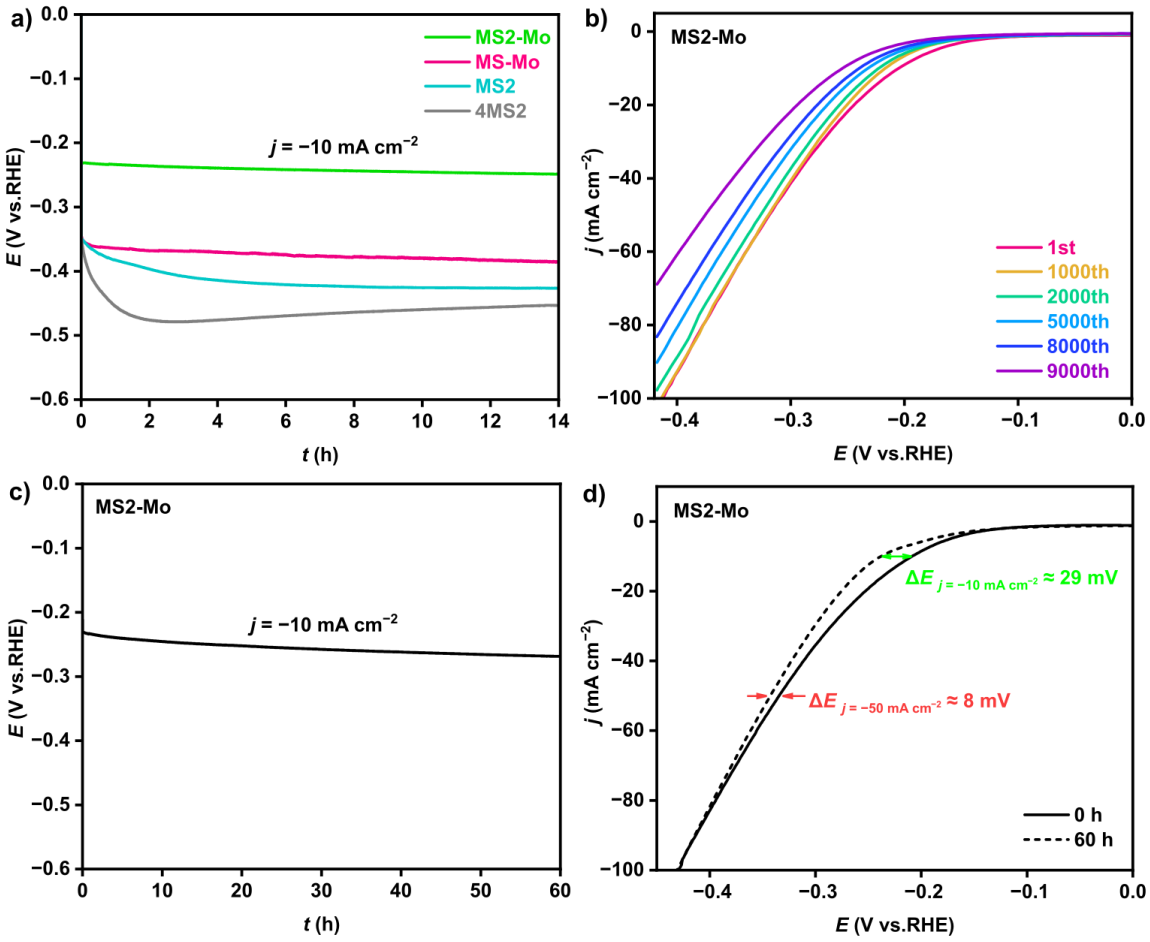

Figure 7.11: (a) Chronopotentiometry of MS2-Mo, MS2, MS-Mo and 4MS2 for 14 h at constant current density of –10 mA cm^{-2}. (b) HER polarization curves of MS2-Mo before and after CV cycles of 1000, 2000, 5000, 8000, 9000. (c) Chronopotentiometry of MS2-Mo for 60 h at constant current density of –10 mA cm^{-2}, and (d) corresponding polarization curves in the beginning and after 60 h.

As MS2-Mo exhibits best performance in durability, two more stability measurements were carried out. Figure 7.11b shows the corresponding polarization curves of MS2-Mo before and after thousands of CV cycles performed between 0.1 V and – 0.42 V vs RHE at the scan rate of 100 mV s^{-1}. Compared to the initial data, the potentials change 12, 17, 27, 34, 49 mV at –10 mA cm^{-2}, and 1, 8, 21, 32, 56 mV at –50 mA cm^{-2} after CV cycles of 1000, 2000, 5000, 8000 and 9000, respectively. MS2-Mo shows almost no loss after the first 1000 CV cycles and displays a slow change before 8000 cycles, demonstrating the excellent stability of materials during the catalytic working potentials in the alkaline condition. Figure 7.11c show longer chronopotentiometry of MS2-Mo for 60 h at constant current density of –10 mA cm^{-2}. MS2-Mo exhibits excellent long-term stability with a minor increase in potential after 60 h, only 29 mV at –10 mA cm^{-2} and 8 mV at –50 mA cm^{-2}, as indicated in comparison for initial and final polarization curves in Figure 7.11d.

Because the HER performance could be heavily influenced by surface area of catalysts, the ECSA of three typical HESs were studied and compared. The double layer capacitance (C_{dl}), as shown in Figure 7.12a, was measured to estimate the ECSA. Figure 7.12b-c plot the CV curves of MS2-Mo, MS-Mo and MS2 in the non-Faradaic region for calculating values of C_{dl}. It's clear that MS2-Mo has much higher C_{dl} (24.5 mF cm^{-2}) and ECSA (612.5

cm^2) than MS2 of C_{dl} (7.6 mF cm^{-2}) and ECSA (190 cm^2) as well as MS-Mo of C_{dl} (5.5 mF cm^{-2}) and ECSA (137.5 cm^2). The large area of MS2-Mo can be derived from special layered structure as discussed in previous HR-TEM results. The Figure 7.12e shows the replotted polarization curves based on corresponding ECSA instead of the same fixed geometric surface area (0.196 cm^2) determined from 5-mm diameter glassy carbon in working electrode. The results indicate that, after accounting for the influence of the catalytic active area, as determined by structural factors like the layered structure, these three HESs do not show a significant difference in catalytic activity as HER electrocatalysts. Because of the similarity of the incorporated metals (except Cr, Mo), the differences between their HER performance are more influenced by structure than by elemental composition. The cocktail effect of high entropy materials nicely combines layered MoS_2 with *Pa*-3 structured multi-metal sulfides, resulting in the huge ECSA and outstanding HER catalytic performance of MS2-Mo, revealing the great potential of the high entropy material for future applications.

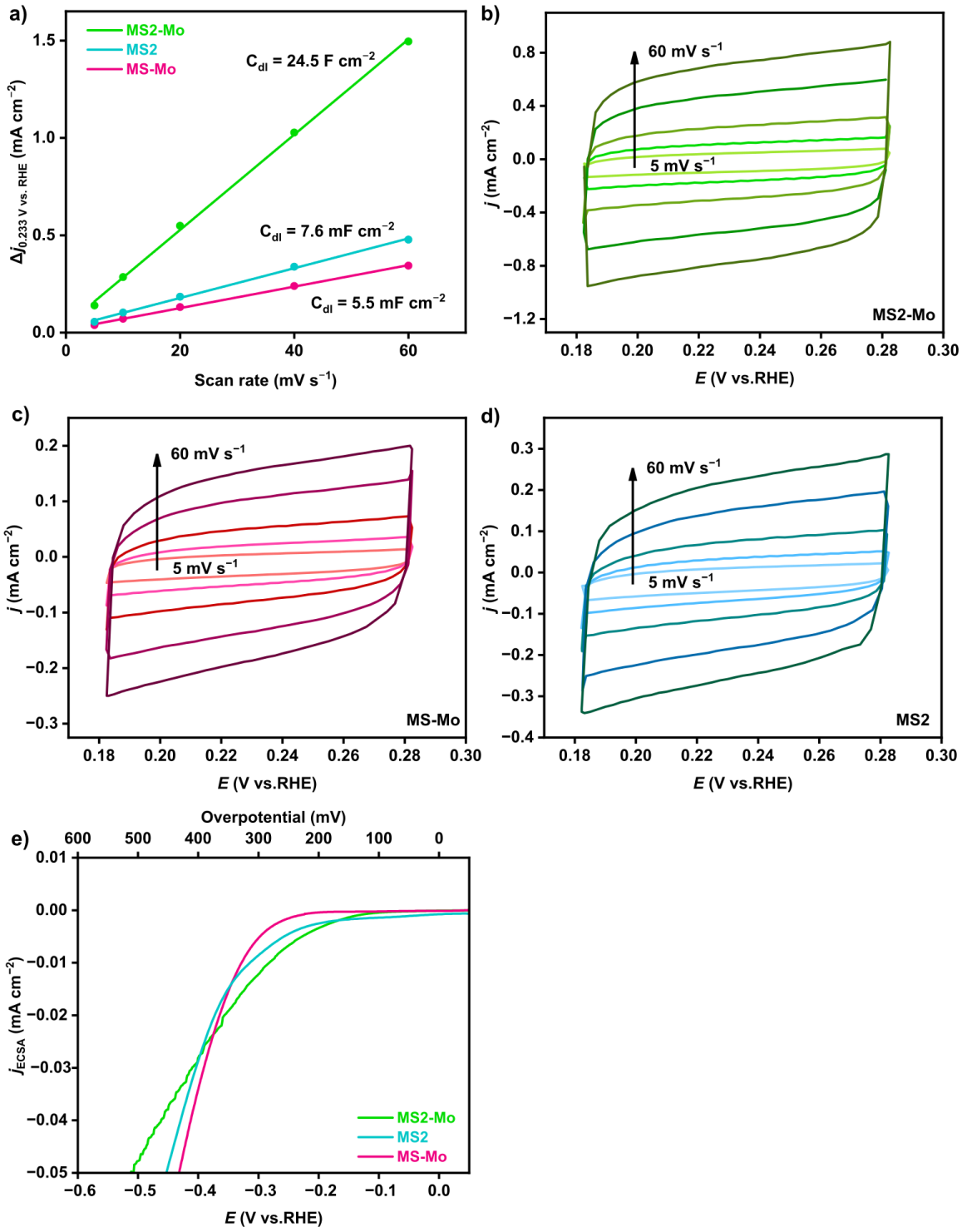

Figure 7.12: (a) Current density differences (Δ*j*) of MS2-Mo, MS2 and MS-Mo from CV curves plotted against the scan rate. The C_{dl} is equivalent to linear slope. CV curves at different scan rates of 5, 10, 20, 40, and 60 mV s^{-1} for (b) MS2-Mo, (c) MS-Mo and (d) MS2. (e) Polarization curves of MS2-Mo, MS2 and MS-Mo based on ECSA.

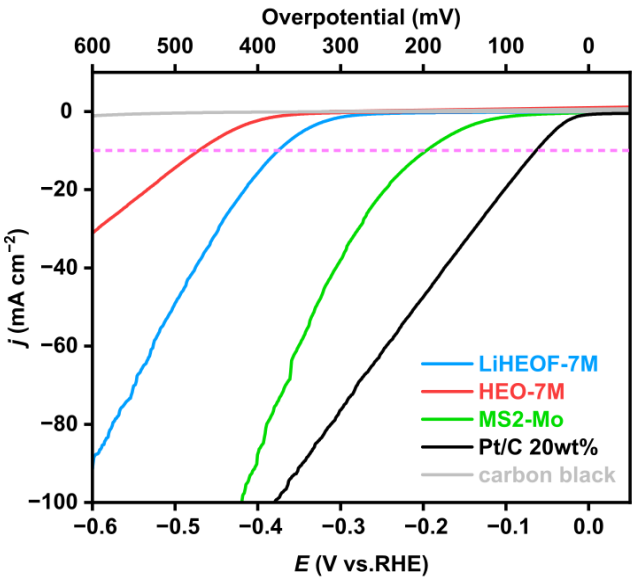

Figure 7.13: Polarization curves of LiHEOF-7M, HEO-7M, MS2-Mo, carbon black and commercial reference Pt/C in a three-electrode cell with an N_2-saturated 1M KOH electrolyte. The pink dashed lines mark the overpotential at current density of –10 mA cm^{-2}.

In addition, to compare the effect of anions in HER catalysis, the polarization curves of rock-salt structured HEO-7M and LiHEOF-7M were measured using the identical setup as for HESs (Figure 7.13). Carbon black was also mixed with samples in a weight ratio of 4:1, to increase conductivity. With the same transition metal composition, LiHEOF-7M shows better HER catalytic performance than HEO, probably benefiting from the interactions of multi-anions (O, F) and metals. The overpotentials of LiHEOF-7M and HEO-7M at a current density of –10 mA cm^{-2} are 374 and 470 mV, respectively, which is larger than most of as-prepared HESs except MS2-Ti. The lower activity of high entropy oxides and oxyfluorides indicates the superiority of S anion over O and F anions for HER high entropy catalysts.

7.3. Conclusion

Two new HESs containing 5 transition metals were designed by additional incorporating Mo, and successfully synthesized via one-step facile mechanochemical synthesis at an inert atmosphere. The MS2-Mo with structure of *Pa*-3 and MS-Mo with structure of *Pnma* were characterized in detail by XRD, ICP-OES, TEM, EDX and XPS. The size of particles ranges in hundreds of nanometers. Different from others, nano-sheets with a layered structure were observed in the TEM result of MS2-Mo. Six equimolar HESs with different compositions were investigated and compared as electrocatalysts for HER using the standard three-electrode setup in an alkaline environment. Compared to medium entropy sulfide, HES samples, especially MS2-Mo, exhibit excellent stability and HER performance under harsh alkaline conditions. MS2-Mo shows significantly higher HER catalytic performance and larger ECSA than other HESs, as it takes full advantage of the *Pa*-3 structured HES and layered MoS_2. The exciting properties of MS2-Mo from its unique structure and elemental interactions can be considered as a good example of the cocktail effect in high entropy materials. By comparison with high entropy oxides and oxyfluorides,

the interaction between the metal cations and the anion S in HESs contributes more to HER catalytic activity. In summary, the findings presented in this chapter underscore the promising potential of HESs as a novel class of catalysts, paving the way for future advancements in the field of electrocatalysis for HER.

Chapter 8

8. Conclusions and Outlook

As a newly developed material class with promising potential for energy applications, HEMs have gained significant attention in recent years, and their synthesis, characterization, and electrochemical applications are attractive areas for future research. This dissertation commences with a facile mechanochemical approach for HEMs, which were subsequently investigated for their potential applications in energy storage and electrocatalysis. The successful design and synthesis of new high entropy oxides, oxyfluorides and sulfides have extended the range of applicable elements and compositions, thereby enabling their utilization in diverse future applications. Moreover, the electrochemical properties of tailored HEMs were thoroughly investigated, and their performances as electrodes in LIBs as well as electrocatalysts for OER and HER were explored in detail.

Chapter 4 presents the full characterization of transition-metal-based high entropy oxides, oxyfluorides and sulfides using a low-cost, facile mechanochemical preparation route. This synthesis method avoids the need for high-temperature preparation or solution processes and enables the incorporation of redox-sensitive ions into single-phase HEMs while preventing oxidation during synthesis by using an inert atmosphere. There is no need for charge compensating components, such as Li ions. Internal disproportionation reactions in multi-metallic high-entropy systems do not alter the average charge of the anion or cation in sublattice, thereby avoiding structural changes required to maintain charge neutrality. Moreover, all as-prepared HEMs can display particles in the size range of a few hundreds of nanometers, with all elements uniformly distributed. By this mechanochemical method, four HEOs and four multi-anionic Li(HEO)Fs with novel element composition were successfully synthesized and show pure rock-salt phase. Furthermore, various HESs with different composition and designed M : S ratios (including 3:2, 1:1, 3:4, 2:3 and 1:2) were also easily prepared, resulting in the formation of novel single-phase HESs in crystal structures of *Pnma* and *Pa*-3. These new HEMs were characterized comprehensively using refined XRD, TEM, EDX, ICP-OES, Mössbauer spectroscopy and XPS. This chapter provides a simple and general pathway for synthesis of novel HEMs, extends the choice of applicable elements and possibility of countless further compositions for various applications.

Chapter 5 investigates the application of single-phase HESs prepared in chapter 4 as electrode materials for LIBs. Specifically, their performance was compared with that of binary sulfide CoS_2, medium entropy sulfide, and prepared HEOs. High entropy pyrite disulfides exhibited highest capacities, as more exchange of lithium ions and electrons through two-step reaction. Furthermore, HESs also exhibited good long-term stability. The superior performance of HESs indicates the beneficial influence of the cocktail effect. Additionally, the advent of the high-entropy concept facilitates customization of composition, enabling the incorporation of various favorable metals for batteries into structures that would not typically form as binary sulfides. Given the availability of tailorable materials with endless combinations, it is worthwhile to explore the application of HESs in rechargeable batteries.
Chapter 6 explores the application of HESs as catalysts for OER. Six new non-equimolar HESs, consisting of 5-6 transition metals, were designed and synthesized using the mechanochemical method. The structure and morphology of the prepared HESs were characterized using XRD, ICP-OES, SEM, TEM, and EDX. The OER catalytic performance of ten HESs (including four equimolar HESs mentioned in chapter 4 and six new designed non-equimolar HESs) was evaluated in a standard three-electrode configuration. Most of the HESs exhibited OER performance superior to that of commercial reference IrO_2 in alkaline electrolyte, suggesting that they are competitive non-noble metal catalysts. HESs also exhibited better OER performance than prepared oxides and oxyfluorides. The influences of different elemental composition and two crystal structure (*Pnma* and *Pa*-3) on OER catalytic activity of catalysts were studied. The catalytic performance was significantly improved by the incorporation of Mo, while the introduction of metal cations with charge of 1+, such as Cu^+ or Ag^+, led to a significant reduction in OER performance. The stability of HESs with the two structure types in alkaline electrolytes was observed to be good by chronopotentiometry. The improved OER performance of HESs can be attributed to the cocktail effects of multiple metals, the interaction between metal and sulfur, and the tunability of the electronic state. HESs can be regarded a promising novel class of non-noble metal catalysts with great potential for future development in OER electro-catalysis.
Chapter 7 discusses the application of prepared HESs as electrocatalysts for HER. Two new HESs with structure of *Pa*-3 and *Pnma* were designed by introducing Mo, successfully synthesized via one-step facile mechanochemical synthesis, and first characterized by XRD, ICP-OES, TEM, EDX and XPS in detail. Different from other prepared HESs, the layer structure nano-sheets were only observed in *Pa*-3 structured HES containing Mo (MS2-Mo), which can be considered as a good example of the cocktail effect in HEMs. The HER catalytic performance of four single phase HESs in chapter 4 and two new prepared HESs was investigated using the standard three-electrode setup in an alkaline electrolyte. HESs, particularly MS2-Mo, outperform medium entropy sulfides in terms of stability and HER catalytic performance in harsh alkaline conditions, thanks to the high entropy and cocktail effects. MS2-Mo exhibits significantly higher HER catalytic performance and a larger ECSA than other HESs, due to its full utilization of the *Pa*-3 structured multi-metal sulfides and layer structure from MoS_2. Compared to high entropy oxides and oxyfluorides, the interaction between the metal cations and anionic sulfur in HESs plays a larger role in enhancing HER catalytic activity. This chapter provides a compelling work that highlights the potential and capabilities of HEMs in electro-catalysis applications.

This dissertation makes significant contributions to the field of high entropy materials (HEMs) and their applications in energy systems. The development of a mechanochemical approach for synthesizing HEMs has introduced a simple and efficient method of preparation, facilitating the creation of numerous compositions for diverse applications. Through the exploration of HEMs in energy storage and conversion, novel high entropy sulfides have been successfully designed and synthesized, demonstrating their promising potential in various fields. This research work greatly advances the understanding and utilization of HEMs, paving the way for further exploration and application in future energy technologies.

A. List of Abbreviations and Symbols

AC	Alternating current
BSEs	Backscattered electrons
CV	Cyclic voltammetry
C_{dl}	Double-layer capacitance
CMC	Carboxymethyl cellulose
DEC	Diethyl carbonate
DMC	Dimethyl carbonate
EALs	Effective attenuation lengths
EC	Ethylene carbonate
ECSA	Electrochemical active surface area
EELS	Electron energy loss spectroscopy
EIS	Electrochemical impedance spectroscopy
EMC	Ethyl methyl carbonate
FSP	Flame spray pyrolysis
GF	Glass microfiber filter paper
HAADF	High angle angular dark field
HEAs	High entropy alloys
HECs	High entropy ceramics
HEMs	High entropy materials
HEOs	High entropy oxides
HESs	High entropy sulfides
HER	Hydrogen evolution reaction
HRTEM	High resolution transmission electron microscopy
HT	Hydrothermal
ICP-OES	Inductively coupled plasma optical emission spectroscopy
IS	Isomer shift
LCO	$LiCoO_2$
Li(HEO)Fs	High entropy Li-containing oxyfluorides
LFP	$LiFePO_4$
LIBs	Lithium-ion batteries
LMO	$LiMn_2O_4$
LSV	Linear sweep voltammetry
M	Metal
MWCNTs	Multi-walled carbon nanotubes
NCM	$LiNi_xCo_yMn_{1-x-y}O_2$

NCA	$LiNi_{0.8}Co_{0.15}Al_{0.05}O_2$
NMC-111	$LiNi_{1/3}Mn_{1/3}Co_{1/3}O_2$
NSP	Nebulized spray pyrolysis
OER	Oxygen evolution reaction
PGMs	Platinum group metals
Pt/C	Platinum on graphitized carbon
PVDF	Polyvinylidene fluoride
QS	Quadrupole splitting
RCP	Reverse co-precipitation
Rct	Charge transfer resistance
RHE	Reversible hydrogen electrode
SAED	Selected area electron diffraction
S_{config}	Configurational entropy
SEI	Solid electrolyte interphase
SEM	Scanning electron microscopy
SEs	Secondary electrons
SCS	Solution combustion synthesis
STEM	Scanning transmission electron microscopy
TEM	Transmission electron microscopy
TMSs	Transition metal sulfides
XPS	X-ray photoelectron spectroscopy
XRD	X-ray diffraction
η	Overpotential

B. List of Figures

C. List of Tables

D. References

[1] M. Wakihara, *Materials Science and Engineering: R: Reports* **2001**, *33*, 109.

[2] M. Bragard, N. Soltau, S. Thomas, R. W. De Doncker, *IEEE Transactions on Power Electronics* **2010**, *25*, 3049.

[3] Y. Ma, Y. Ma, Q. Wang, S. Schweidler, M. Botros, T. Fu, H. Hahn, T. Brezesinski, B. Breitung, *Energy & Environmental Science* **2021**, *14*, 2883.

[4] T. Chen, Y. Jin, H. Lv, A. Yang, M. Liu, B. Chen, Y. Xie, Q. Chen, *Transactions of Tianjin University* **2020**, *26*, 208.

[5] T. Or, S. W. Gourley, K. Kaliyappan, A. Yu, Z. Chen, *Carbon Energy* **2020**, *2*, 6.

[6] Y. Liang, C. Zhao, H. Yuan, Y. Chen, W. Zhang, J. Huang, D. Yu, Y. Liu, M. Titirici, Y. Chueh, *InfoMat* **2019**, *1*, 6.

[7] M. M. Thackeray, C. Wolverton, E. D. Isaacs, *Energy & Environmental Science* **2012**, *5*, 7854.

[8] C. De las Casas, W. Li, *Journal of Power Sources* **2012**, *208*, 74.

[9] L. Ji, Z. Lin, M. Alcoutlabi, X. Zhang, *Energy & Environmental Science* **2011**, *4*, 2682.

[10] S. Chae, M. Ko, K. Kim, K. Ahn, J. Cho, *Joule* **2017**, *1*, 47.

[11] W. J. Zhang, *Journal of Power Sources* **2011**, *196*, 13.

[12] G. Zubi, R. Dufo-López, M. Carvalho, G. Pasaoglu, *Renewable and Sustainable Energy Reviews* **2018**, *89*, 292.

[13] M. R. Palacin, *Chemical Society Reviews* **2009**, *38*, 2565.

[14] Y. Yuan, K. Amine, J. Lu, R. Shahbazian-Yassar, *Nature communications* **2017**, *8*, 15806.

[15] S. Imtiaz, I. S. Amiinu, Y. Xu, T. Kennedy, C. Blackman, K. M. Ryan, *Materials Today* **2021**, *48*, 241.

[16] F. Wang, R. Robert, N. A. Chernova, N. Pereira, F. Omenya, F. Badway, X. Hua, M. Ruotolo, R. Zhang, L. Wu, *Journal of the American Chemical Society* **2011**, *133*, 18828.

[17] J. Zhu, L. Hu, P. Zhao, L. Y. S. Lee, K. Y. Wong, *Chemical reviews* **2019**, *120*, 851.

[18] S. E. Hosseini, M. A. Wahid, *Renewable and Sustainable Energy Reviews* **2016**, *57*, 850.

[19] A. P. van Troostwijk, J. R. Deiman, *Observations sur la Physique* **1789**, *35*, 369.

[20] J. Joo, T. Kim, J. Lee, S. Choi, K. Lee, *Advanced materials* **2019**, *31*, 1806682.

[21] C. G. Morales-Guio, L. A. Stern, X. Hu, *Chemical Society Reviews* **2014**, *43*, 6555.

[22] J. O. M. Bockris, T. Otagawa, *Journal of the Electrochemical Society* **1984**, *131*, 290.

[23] W. H. Wade, N. Hackerman, *Transactions of the Faraday Society* **1957**, *53*, 1636.

[24] A. Krasilshchikov, *Zhurnal Fizicheskoi Khimii* **1963**, *37*, 531.

[25] J. Bockris, *The Journal of Chemical Physics* **1956**, *24*, 817.

[26] Y. Matsumoto, E. Sato, *Materials chemistry and physics* **1986**, *14*, 397.

[27] N. T. Suen, S. F. Hung, Q. Quan, N. Zhang, Y. J. Xu, H. M. Chen, *Chemical Society Reviews* **2017**, *46*, 337.

[28] A. Badruzzaman, A. Yuda, A. Ashok, A. Kumar, *Inorganica Chimica Acta* **2020**, *511*, 119854.

[29] Z. Wu, X. F. Lu, S. Zang, X. W. Lou, *Advanced Functional Materials* **2020**, *30*, 1910274.

[30] K. Zhang, R. Zou, *Small* **2021**, *17*, 2100129.

[31] S. Anantharaj, S. R. Ede, K. Sakthikumar, K. Karthick, S. Mishra, S. Kundu, *Acs Catalysis* **2016**, *6*, 8069.

[32] M. Wang, L. Zhang, Y. He, H. Zhu, *Journal of Materials Chemistry A* **2021**, *9*, 5320.

[33] N. Han, P. Liu, J. Jiang, L. Ai, Z. Shao, S. Liu, *Journal of Materials Chemistry A* **2018**, *6*, 19912.

[34] M. Huynh, C. Shi, S. J. Billinge, D. G. Nocera, *Journal of the American Chemical Society* **2015**, *137*, 14887.

[35] L. Xie, R. Zhang, L. Cui, D. Liu, S. Hao, Y. Ma, G. Du, A. M. Asiri, X. Sun, *Angewandte Chemie International Edition* **2017**, *56*, 1064.

[36] M. W. Kanan, D. G. Nocera, *Science* **2008**, *321*, 1072.

[37] P. Chen, K. Xu, T. Zhou, Y. Tong, J. Wu, H. Cheng, X. Lu, H. Ding, C. Wu, Y. Xie, *Angewandte Chemie International Edition* **2016**, *55*, 2488.

[38] M. S. Burke, L. J. Enman, A. S. Batchellor, S. Zou, S. W. Boettcher, *Chemistry of Materials* **2015**, *27*, 7549.

[39] D. Jin, F. Qiao, H. Chu, Y. Xie, *Nanoscale* **2023**, *15*, 7202.

[40] Z. Chen, X. Duan, W. Wei, S. Wang, B. J. Ni, *Journal of Materials Chemistry A* **2019**, *7*, 14971.

[41] W. F. Chen, J. T. Muckerman, E. Fujita, *Chemical communications* **2013**, *49*, 8896.

[42] Y. Wang, Y. Zhao, X. Ding, L. Qiao, *Journal of Energy Chemistry* **2021**, *60*, 451.

[43] Y. Shi, B. Zhang, *Chemical Society Reviews* **2016**, *45*, 1529.

[44] Y. Jiang, Y. Lu, *Nanoscale* **2020**, *12*, 9327.

[45] L. Lin, K. Wang, A. Sarkar, C. Njel, G. Karkera, Q. Wang, R. Azmi, M. Fichtner, H. Hahn, S. Schweidler, *Advanced energy materials* **2022**, *12*, 2103090.

[46] B. Cantor, I. Chang, P. Knight, A. Vincent, *Materials Science and Engineering: A* **2004**, *375*, 213.

[47] J. Yeh, S. Chen, S. Lin, J. Gan, T. Chin, T. Shun, C. Tsau, S. Chang, *Advanced engineering materials* **2004**, *6*, 299.

[48] C. M. Rost, E. Sachet, T. Borman, A. Moballegh, E. C. Dickey, D. Hou, J. L. Jones, S. Curtarolo, J. P. Maria, *Nature communications* **2015**, *6*, 8485.

[49] A. Sarkar, L. Velasco, D. Wang, Q. Wang, G. Talasila, L. de Biasi, C. Kübel, T. Brezesinski, S. S. Bhattacharya, H. Hahn, *Nature communications* **2018**, *9*, 3400.

[50] Z. Lun, B. Ouyang, D. H. Kwon, Y. Ha, E. E. Foley, T. Y. Huang, Z. Cai, H. Kim, M. Balasubramanian, Y. Sun, *Nature materials* **2021**, *20*, 214.

[51] Q. Wang, A. Sarkar, D. Wang, L. Velasco, R. Azmi, S. S. Bhattacharya, T. Bergfeldt, A. Düvel, P. Heitjans, T. Brezesinski, *Energy & Environmental Science* **2019**, *12*, 2433.

[52] J. Gild, Y. Zhang, T. Harrington, S. Jiang, T. Hu, M. C. Quinn, W. M. Mellor, N. Zhou, K. Vecchio, J. Luo, *Scientific reports* **2016**, *6*, 37946.

[53] P. Sarker, T. Harrington, C. Toher, C. Oses, M. Samiee, J. P. Maria, D. W. Brenner, K. S. Vecchio, S. Curtarolo, *Nature communications* **2018**, *9*, 4980.

[54] T. Jin, X. Sang, R. R. Unocic, R. T. Kinch, X. Liu, J. Hu, H. Liu, S. Dai, *Advanced materials* **2018**, *30*, 1707512.

[55] P. A. Sukkurji, Y. Cui, S. Lee, K. Wang, R. Azmi, A. Sarkar, S. Indris, S. S. Bhattacharya, R. Kruk, H. Hahn, *Journal of Materials Chemistry A* **2021**, *9*, 8998.

[56] T. Wang, H. Chen, Z. Yang, J. Liang, S. Dai, *Journal of the American Chemical Society* **2020**, *142*, 4550.

[57] X. Chen, Y. Wu, *Journal of the American Ceramic Society* **2020**, *103*, 750.

[58] Y. Qin, J. X. Liu, F. Li, X. Wei, H. Wu, G. J. Zhang, *Journal of Advanced Ceramics* **2019**, *8*, 148.

[59] Z. Deng, A. Olvera, J. Casamento, J. S. Lopez, L. Williams, R. Lu, G. Shi, P. F. Poudeu, E. Kioupakis, *Chemistry of Materials* **2020**, *32*, 6070.

[60] M. Cui, C. Yang, B. Li, Q. Dong, M. Wu, S. Hwang, H. Xie, X. Wang, G. Wang, L. Hu, *Advanced Energy Materials* **2021**, *11*, 2002887.

[61] C. R. McCormick, R. E. Schaak, *Journal of the American Chemical Society* **2021**, *143*, 1017.

[62] R. Z. Zhang, F. Gucci, H. Zhu, K. Chen, M. J. Reece, *Inorganic chemistry* **2018**, *57*, 13027.

[63] X. Zhao, Z. Xue, W. Chen, Y. Wang, T. Mu, *ChemSusChem* **2020**, *13*, 2038.

[64] D. Lai, Q. Kang, F. Gao, Q. Lu, *Journal of Materials Chemistry A* **2021**, *9*, 17913.

[65] D. B. Miracle, O. N. Senkov, *Acta Materialia* **2017**, *122*, 448.

[66] J. W. Yeh, *JOM* **2013**, *65*, 1759.

[67] L. Boltzmann, *Über die Beziehung zwischen dem zweiten Hauptsatze des mechanischen Wärmetheorie und der Wahrscheinlichkeitsrechnung, respective den Sätzen über das Wärmegleichgewicht*, K.K. Hof- und Staatsdruckerei, **1877**.

[68] C. H. Tsau, Y. C. Yang, C. C. Lee, L. Y. Wu, H. J. Huang, *Procedia Engineering* **2012**, *36*, 246.

[69] M. H. Hsieh, M. H. Tsai, W. J. Shen, J. W. Yeh, *Surface and Coatings Technology* **2013**, *221*, 118.

[70] Y. Wang, D. Li, L. Parent, H. Tian, *Wear* **2011**, *271*, 1623.

[71] M. C. Gao, J. W. Yeh, P. K. Liaw, Y. Zhang, *High-Entropy Alloys; Fundamentals and Applications*, Springer, **2016**.

[72] Y. Yao, Z. Huang, P. Xie, S. D. Lacey, R. J. Jacob, H. Xie, F. Chen, A. Nie, T. Pu, M. Rehwoldt, *Science* **2018**, *359*, 1489.

[73] S. H. Albedwawi, A. AlJaberi, G. N. Haidemenopoulos, K. Polychronopoulou, *Materials & Design* **2021**, *202*, 109534.

[74] S. Shafeie, S. Guo, Q. Hu, H. Fahlquist, P. Erhart, A. Palmqvist, *Journal of Applied Physics* **2015**, *118*, 184905.

[75] C. Zhao, F. Ding, Y. Lu, L. Chen, Y. Hu, *Angewandte Chemie International Edition* **2020**, *59*, 264.

[76] T. X. Nguyen, Y. Su, C. Lin, J. Ting, *Advanced Functional Materials* **2021**, *31*, 2106229.

[77] Y. Lei, L. Zhang, W. Xu, C. Xiong, W. Chen, X. Xiang, B. Zhang, H. Shang, *Nano Research* **2022**, *15*, 6054.

[78] J. Cavin, A. Ahmadiparidari, L. Majidi, A. S. Thind, S. N. Misal, A. Prajapati, Z. Hemmat, S. Rastegar, A. Beukelman, M. R. Singh, *Advanced Materials* **2021**, *33*, 2100347.

[79] J. Zhao, Y. Zhang, X. Chen, G. Sun, X. Yang, Y. Zeng, R. Tian, F. Du, *Advanced Functional Materials* **2022**, *32*, 2206531.

[80] F. Li, Y. Ma, H. Wu, Q. Zhai, J. Zhao, H. Ji, S. Tang, X. Meng, *The Journal of Physical Chemistry C* **2022**, *126*, 18323.

[81] M. Moradi, F. Hasanvandian, A. Bahadoran, A. Shokri, S. Zerangnasrabad, B. Kakavandi, *Electrochimica Acta* **2022**, *436*, 141444.

[82] A. Ali, Y. W. Chiang, R. M. Santos, *Minerals* **2022**, *12*, 205.

[83] C. G. Pope, *Journal of chemical education* **1997**, *74*, 129.

[84] M. De la Guardia, S. Armenta, In *Comprehensive Analytical Chemistry*, Elsevier, **2011**, *57*. 121–156.

[85] K. D. Vernon-Parry, *III-Vs Review* **2000**, *13*, 40.

[86] W. Zhou, R. Apkarian, Z. L. Wang, D. Joy, *Scanning Microscopy for Nanotechnology: Techniques and Applications*, Springer Science & Business Media, **2007**.

[87] D. B. Williams, C. B. Carter, D. B. Williams, C. B. Carter, *The transmission electron microscope*, Springer, **1996**.

[88] J. Liu, J. Cowley, *Ultramicroscopy* **1993**, *52*, 335.

[89] K. L. Parry, A. Shard, R. Short, R. White, J. Whittle, A. Wright, *Surface and Interface Analysis: An International Journal devoted to the development and application of techniques for the analysis of surfaces, interfaces and thin films* **2006**, *38*, 1497.

[90] J. H. Scofield, *Journal of Electron Spectroscopy and Related Phenomena* **1976**, *8*, 129.

[91] S. Tanuma, C. Powell, D. Penn, *Surface and interface analysis* **2011**, *43*, 689.

[92] J. Chastain, R. C. King Jr, *Perkin-Elmer Corporation* **1992**, *40*, 221.

[93] C. C. McCrory, S. Jung, J. C. Peters, T. F. Jaramillo, *Journal of the American Chemical Society* **2013**, *135*, 16977.

[95] L. Lin, K. Wang, R. Azmi, J. Wang, A. Sarkar, M. Botros, S. Najib, Y. Cui, D. Stenzel, P. Anitha Sukkurji, *Journal of Materials Science* **2020**, *55*, 16879.

[96] J. Dąbrowa, M. Stygar, A. Mikuła, A. Knapik, K. Mroczka, W. Tejchman, M. Danielewski, M. Martin, *Materials Letters* **2018**, *216*, 32.

[97] A. Sarkar, R. Djenadic, D. Wang, C. Hein, R. Kautenburger, O. Clemens, H. Hahn, *Journal of the European Ceramic Society* **2018**, *38*, 2318.

[98] K. Chen, X. Pei, L. Tang, H. Cheng, Z. Li, C. Li, X. Zhang, L. An, *Journal of the European Ceramic Society* **2018**, *38*, 4161.

[99] R. Djenadic, A. Sarkar, O. Clemens, C. Loho, M. Botros, V. S. Chakravadhanula, C. Kübel, S. S. Bhattacharya, A. S. Gandhi, H. Hahn, *Materials Research Letters* **2017**, *5*, 102.

[100] A. Sarkar, R. Djenadic, N. J. Usharani, K. P. Sanghvi, V. S. Chakravadhanula, A. S. Gandhi, H. Hahn, S. S. Bhattacharya, *Journal of the European Ceramic Society* **2017**, *37*, 747.

[101] M. Biesuz, L. Spiridigliozzi, G. Dell'Agli, M. Bortolotti, V. M. Sglavo, *Journal of materials science* **2018**, *53*, 8074.

[102] A. Mao, F. Quan, H. Z. Xiang, Z. G. Zhang, K. Kuramoto, A. L. Xia, *Journal of Molecular Structure* **2019**, *1194*, 11.

[103] A. Mao, H. Z. Xiang, Z. G. Zhang, K. Kuramoto, H. Yu, S. Ran, *Journal of Magnetism and Magnetic Materials* **2019**, *484*, 245.

[104] D. Bérardan, S. Franger, A. Meena, N. Dragoe, *Journal of Materials Chemistry A* **2016**, *4*, 9536.

[105] D. Bérardan, S. Franger, D. Dragoe, A. K. Meena, N. Dragoe, *physica status solidi (RRL)–Rapid Research Letters* **2016**, *10*, 328.

[106] J. Wang, D. Stenzel, R. Azmi, S. Najib, K. Wang, J. Jeong, A. Sarkar, Q. Wang, P. A. Sukkurji, T. Bergfeldt, *Electrochem* **2020**, *1*, 60.

[107] R. D. Shannon, *Acta crystallographica section A: crystal physics, diffraction, theoretical and general crystallography* **1976**, *32*, 751.

[108] R. G. Burns, *Mineralogical applications of crystal field theory*, Cambridge university press, **1993**.

[109] Y. Shimura, *Bulletin of the Chemical Society of Japan* **1988**, *61*, 693.

[110] F. Menil, *Journal of Physics and Chemistry of Solids* **1985**, *46*, 763.

[111] D. Sen, C. W. Kim, N. H. Heo, K. Seff, *Journal of Porous Materials* **2014**, *21*, 321.

[112] K. Morishita, H. Suto, I. Kamiya, *IEEE 42nd photovoltaic specialist conference (PVSC)*, New Orleans, **2015**, 1–4.

[113] M. C. Biesinger, *Surface and Interface Analysis* **2017**, *49*, 1325.

[114] P. Metcalf, P. Fanwick, Z. Kakol, J. Honig, *Journal of Solid State Chemistry* **1993**, *104*, 81.

[115] Y. Kesler, S. Smirnov, K. Pokholok, B. Viting, *Inorganic materials* **1991**, *27*, 977.

[116] F. Jellinek, *Acta Crystallographica* **1957**, *10*, 620.

[117] He. King, C. Prewitt, *Acta Crystallographica Section B: Structural Crystallography and Crystal Chemistry* **1982**, *38*, 1877.

[118] A. P. Chandra, A. R. Gerson, *Geochimica et Cosmochimica Acta* **2011**, *75*, 6239.

[119] Z. Rak, C. Rost, M. Lim, P. Sarker, C. Toher, S. Curtarolo, J. P. Maria, D. Brenner, *Journal of Applied Physics* **2016**, *120*, 095105.

[120] N. Osenciat, D. Bérardan, D. Dragoe, B. Léridon, S. Holé, A. K. Meena, S. Franger, N. Dragoe, *Journal of the American Ceramic Society* **2019**, *102*, 6156.

[121] L. Benoist, D. Gonbeau, G. Pfister-Guillouzo, E. Schmidt, G. Meunier, A. Levasseur, *Thin Solid Films* **1995**, *258*, 110.

[122] D. Gonbeau, C. Guimon, G. Pfister-Guillouzo, A. Levasseur, G. Meunier, R. Dormoy, *Surface Science* **1991**, *254*, 81.

[123] M. C. Biesinger, B. P. Payne, B. R. Hart, A. P. Grosvenor, N. S. McIntryre, L. W. Lau, R. S. Smart, *Journal of Physics: Conference Series* **2008**, *100*, 012025.

[124] R. Azmi, V. Trouillet, M. Strafela, S. Ulrich, H. Ehrenberg, M. Bruns, *Surface and Interface Analysis* **2018**, *50*, 43.

[125] J. L. Junta, M. F. Hochella Jr, *Geochimica et Cosmochimica Acta* **1994**, *58*, 4985.

[126] J. Yin, F. Zhu, J. Lai, H. Chen, M. Zhang, J. Zhang, J. Wang, T. He, B. Zhang, J. Yuan, *Advanced optical materials* **2019**, *7*, 1801303.

[127] G. Chatzitheodorou, S. Fiechter, M. Kunst, J. Luck, H. Tributsch, *Materials research bulletin* **1988**, *23*, 1261.

[128] P. Geng, S. Zheng, H. Tang, R. Zhu, L. Zhang, S. Cao, H. Xue, H. Pang, *Advanced Energy Materials* **2018**, *8*, 1703259.

[129] N. Sethulakshmi, A. Mishra, P. M. Ajayan, Y. Kawazoe, A. K. Roy, A. K. Singh, C. S. Tiwary, *Materials today* **2019**, *27*, 107.

[130] J. Zhao, Y. Zhang, Y. Wang, H. Li, Y. Peng, *Journal of Energy Chemistry* **2018**, *27*, 1536.

[131] C. Rao, K. Pisharody, *Progress in Solid State Chemistry* **1976**, *10*, 207.

[132] H. W. Nesbitt, M. Reinke, *American Mineralogist* **1999**, *84*, 639.

[133] Y. Ma, Y. Ma, D. Bresser, Y. Ji, D. Geiger, U. Kaiser, C. Streb, A. Varzi, S. Passerini, *ACS nano* **2018**, *12*, 7220.

[134] R. Fong, J. Dahn, C. Jones, *Journal of The Electrochemical Society* **1989**, *136*, 3206.

[135] Q. Wang, L. Jiao, Y. Han, H. Du, W. Peng, Q. Huan, D. Song, Y. Si, Y. Wang, H. Yuan, *The Journal of Physical Chemistry C* **2011**, *115*, 8300.

[136] L. Liu, Z. Yuan, C. Qiu, J. Liu, *Solid State Ionics* **2013**, *241*, 25.

[137] D. Larcher, J. M. Tarascon, *Nature chemistry* **2015**, *7*, 19.

[138] Y. Cui, P. A. Sukkurji, K. Wang, R. Azmi, A. M. Nunn, H. Hahn, B. Breitung, Y. Y. Ting, P. M. Kowalski, P. Kaghazchi, *Journal of Energy Chemistry* **2022**, *72*, 342.

[139] P. Poizot, S. Laruelle, S. Grugeon, L. Dupont, J. Tarascon, *Nature* **2000**, *407*, 496.

[140] L. Lin, Z. Ding, G. Karkera, T. Diemant, M. V. Kante, D. Agrawal, H. Hahn, J. Aghassi-Hagmann, M. Fichtner, B. Breitung, S. Schweidler, *Small Structures* **2023**, 2300012.

[141] S. R. Ede, Z. Luo, *Journal of Materials Chemistry A* **2021**, *9*, 20131.

[142] Y. Sun, T. Zhang, C. Li, K. Xu, Y. Li, *Journal of Materials Chemistry A* **2020**, *8*, 13415.

[143] J. Zhao, J. Zhang, Z. Li, X. Bu, *Small* **2020**, *16*, 2003916.

[144] D. Li, H. Liu, L. Feng, *Energy & Fuels* **2020**, *34*, 13491.

[145] T. Bao, Y. Xia, J. Lu, C. Zhang, J. Wang, L. Yuan, Y. Zhang, C. Liu, C. Yu, *Small* **2022**, *18*, 2103106.

[146] Y. Xu, A. Sumboja, A. Groves, T. Ashton, Y. Zong, J. A. Darr, *RSC advances* **2020**, *10*, 41871.

[147] F. Dong, Y. Meng, W. Han, H. Zhao, Z. Tang, *Scientific reports* **2019**, *9*, 1.

[148] L. Li, G. Li, Y. Zhang, W. Ouyang, H. Zhang, F. Dong, X. Gao, Z. Lin, *Journal of Materials Chemistry A* **2020**, *8*, 25687.

[149] Y. Mei, Y. Feng, C. Zhang, Y. Zhang, Q. Qi, J. Hu, *ACS Catalysis* **2022**, *12*, 10808.

[150] Y. Deng, A. D. Handoko, Y. Du, S. Xi, B. S. Yeo, *ACS Catalysis* **2016**, *6*, 2473.

[151] L. Gong, J. Koh, B. S. Yeo, *ChemSusChem* **2018**, *11*, 3790.

[152] M. S. Burke, M. G. Kast, L. Trotochaud, A. M. Smith, S. W. Boettcher, *Journal of the American Chemical Society* **2015**, *137*, 3638.

[153] S. Jin, *ACS Energy Letters* **2017**, *2*, 1937.

[154] W. Wang, S. Zhu, X. Chen, X. Zhang, Y. Tao, Y. Zhang, R. Xiang, X. Wu, *Nanotechnology* **2020**, *31*, 475402.

[155] Y. Sun, S. Dai, *Science Advances* **2021**, *7*, 1600.

[156] K. Wan, J. Luo, C. Zhou, T. Zhang, J. Arbiol, X. Lu, B. Mao, X. Zhang, J. Fransaer, *Advanced Functional Materials* **2019**, *29*, 1900315.

[157] K. Prabakaran, M. Lokanathan, B. Kakade, *Applied Surface Science* **2019**, *466*, 830.

[158] I. S. Amiinu, Z. Pu, X. Liu, K. A. Owusu, H. G. R. Monestel, F. O. Boakye, H. Zhang, S. Mu, *Advanced Functional Materials* **2017**, *27*, 1702300.

[159] J. Kundu, S. Khilari, K. Bhunia, D. Pradhan, *Catalysis Science & Technology* **2019**, *9*, 406.

[160] M. Chauhan, K. P. Reddy, C. S. Gopinath, S. Deka, *ACS Catalysis* **2017**, *7*, 5871.

[161] H. Han, K. M. Kim, H. Choi, G. Ali, K. Y. Chung, Y. R. Hong, J. Choi, J. Kwon, S. W. Lee, J. W. Lee, *ACS Catalysis* **2018**, *8*, 4091.

[162] J. Jiang, S. Lu, H. Gao, X. Zhang, H. Q. Yu, *Nano Energy* **2016**, *27*, 526.

[163] J. Nai, Y. Lu, X. Y. Yu, *Journal of Materials Chemistry A* **2018**, *6*, 21891.

[164] L. Li, P. Wang, Q. Shao, X. Huang, *Chemical Society Reviews* **2020**, *49*, 3072.

[165] A. N. Enyashin, L. Yadgarov, L. Houben, I. Popov, M. Weidenbach, R. Tenne, M. Bar-Sadan, G. Seifert, *The Journal of Physical Chemistry C* **2011**, *115*, 24586.

[166] S. Wang, D. Zhang, B. Li, C. Zhang, Z. Du, H. Yin, X. Bi, S. Yang, *Advanced Energy Materials* **2018**, *8*, 1801345.

[167] C. P. Veeramalai, F. Li, Y. Liu, Z. Xu, T. Guo, T. W. Kim, *Applied Surface Science* **2016**, *389*, 1017.

[168] Y. J. Lee, D. Barrera, K. Luo, J. W. Hsu, *Journal of Nanotechnology* **2012**, *2012*, 195761.

[169] V. Fominski, M. Demin, V. Nevolin, D. Fominski, R. Romanov, M. Gritskevich, N. Smirnov, *Nanomaterials* **2020**, *10*, 653.

[170] M. C. Biesinger, B. P. Payne, A. P. Grosvenor, L. W. Lau, A. R. Gerson, R. S. C. Smart, *Applied Surface Science* **2011**, *257*, 2717.

E. Curriculum Vitae

Education

12/2019-present	PhD candidate, Germany Institute of Nanotechnology (INT), Karlsruhe Institute of Technology (KIT) Technische Universität Darmstadt (TUD) Research field: High entropy materials for Rechargeable Batteries and Water Splitting Electrocatalysis
09/2014-07/2017	Master of Science in Inorganic Chemistry, P. R. China Fujian Institute of Research on the Structure of Matter, Chinese Academy of Sciences University of Chinese Academy of Sciences Research field: Organic-inorganic hybrid optical functional materials for Organic Light-Emitting Diode devices (OLED)
09/2010-07/2014	Bachelor of Science in Chemistry (Teacher Education), P. R. China Nanjing Normal University

Peer-reviewed publications (* = during Ph.D. program):

1. High entropy sulfides for HER. (In submission) *
2. **Ling Lin**, Ziming Ding, Guruprakash Karkera, Thomas Diemant, Mohana Veerraju Kante, Daisy Agrawal, Horst Hahn, Jasmin Aghassi, Maximilian Fichtner, Ben Breitung, and Simon Schweidler, "High-Entropy Sulfides as Highly Effective Catalysts for the Oxygen Evolution Reaction", *Small Structure*, 2023, 2300012.*

   https://doi.org/10.1002/sstr.202300012
3. Claudia Triolo, Simon Schweidler, **Ling Lin**, Gioele Pagot, Vito Di Noto, Ben Breitung, Saveria Santangelo, "Evaluation of electrospun spinel-type high-entropy $(Cr_{0.2}Mn_{0.2}Fe_{0.2}Co_{0.2}Ni_{0.2})_3O_4$, $(Cr_{0.2}Mn_{0.2}Fe_{0.2}Co_{0.2}Zn_{0.2})_3O_4$ and $(Cr_{0.2}Mn_{0.2}Fe_{0.2}Ni_{0.2}Zn_{0.2})_3O_4$ oxide nanofibers as electrocatalysts for oxygen evolution in alkaline medium", *Energy Advances*, 2023, 2, 667-678. *

   https://doi.org/10.1039/D3YA00062A
4. **Ling Lin**, Kai Wang, Abhishek Sarkar, Christian Njel, Guruprakash Karkera, Qingsong Wang, Raheleh Azmi,

Maximilian Fichtner, Horst Hahn, Simon Schweidler, Ben Breitung, “High‐Entropy Sulfides as Electrode Materials for Li-Ion Batteries”, *Advanced Energy Materials*, 2022, 12(8), 2103090. *

https://doi.org/10.1002/aenm.202103090

5. Simon Schweidler, Yushu Tang, **Ling Lin**, Guruprakash Karkera, Alaa Alsawaf, Lucile Bernadet, Ben Breitung, Horst Hahn, Maximilian Fichtner, Albert Tarancón, Miriam Botros, “Synthesis of perovskite-type high-entropy oxides as potential candidates for oxygen evolution”, *Frontiers in Energy Research*, 2022, 10, 983979. *

   https://doi.org/10.3389/fenrg.2022.983979

6. David Stenzel, Bei Zhou, Chukwudalu Okafor, Mohana Veeraju Kante, **Ling Lin**, Georgian Melinte, Thomas Bergfeldt, Miriam Botros, Horst Hahn, Ben Breitung, Simon Schweidler, “High-entropy spinel-structure oxides as oxygen evolution reaction electrocatalyst”, *Frontiers in Energy Research*, 2022, 10, 942314. *

   https://doi.org/10.3389/fenrg.2022.942314

7. **Ling Lin**, Kai Wang, Raheleh Azmi, Junbo Wang, Abhishek Sarkar, Miriam Botros, Saleem Najib, Yanyan Cui, David Stenzel, Parvathy Anitha Sukkurji, Qingsong Wang, Horst Hahn, Simon Schweidler, and Ben Breitung, “Mechanochemical synthesis: route to novel rock-salt structured high-entropy oxides and oxyfluorides”, *Journal of Materials Science*, 2020, 55, 16879-16889. *

   https://doi.org/10.1007/s10853-020-05183-4

8. **Ling Lin**, Dong-Hui Chen, Rongmin Yu, Xu-Lin Chen, Wen-Juan Zhu, Dong Liang, Jian-Fei Chang, Qing Zhang and Can-Zhong Lu, “Photo- and electro-luminescence of three TADF binuclear Cu(I) complexes with functional tetraimine ligands”, *Journal of Materials Chemistry C*, 2017, 5, 4495-4504.

   https://doi.org/10.1039/C7TC00443E

9. **Lin Ling**, Chen Xu-Lin, Chen Dong-Hui, Wu Xiao-Yuan, Yu Rong-Min, Lu Can-Zhong, “Synthesis, Crystal Structure, and Photo- and Electro-luminescence of a TADF Cu(I) Complex”, *Chinese Journal of Structural Chemistry*, 2017, 36, 1493-1501.

   https://doi.org/10.14102/j.cnki.0254-5861.2011-1560

Patents (during PhD)

Ling Lin, Simon Schweidler, Ben Breitung and Horst Hahn, “High-Entropy Sulfide als HER Katalysatoren”, 2023, in submission.

Conference talks (during PhD)

Ling Lin, Ben Breitung, Simon Schweidler, Horst Hahn "Mechanochemical route to novel high entropy sulfides for rechargeable battery and electrocatalytic water splitting", European Materials Research Society (E-MRS) 2023 Spring Meeting & Exhibit, Strasbourg, France, 2023.

Posters (during PhD)

Ling Lin, Ben Breitung, Horst Hahn "High-Entropy Materials For Li-ion Batteries", POLiS - Joint Cluster of Excellence of KIT & Ulm University with Associated Partners JLU Gießen & ZSW, Ulm, Germany, 2020.

Ling Lin, Ben Breitung, Simon Schweidler, Qingsong Wang, Horst Hahn "Mechanochemical Synthesis: Route to Novel High-Entropy Materials", NiPS-EnABLES Summer School, Perugia, Italy, 2021.

F. Acknowledgements

The successful completion of this dissertation has been made possible through fruitful collaboration, the support of colleagues, friends and family, as well as the generous funding from Chinese Scholarship Council (CSC). I extend my heartfelt gratitude to all those who have helped and supported me throughout my PhD study.

First, I would like to express my sincere gratitude to my PhD supervisor, Prof. Dr. Horst Hahn, for giving me the chance to join his research group at the Institute of Nanotechnology (INT) at Karlsruhe Institute of Technology (KIT). The group has offered the optimal conditions for scientific research, a thriving international research environment, and significant opportunities for personal growth.

I would like to express my deep appreciation to my main supervisor, Dr. Ben Breitung, for his patient guidance, fruitful scientific discussions, insightful comments and revisions for my manuscripts, and warm help regarding various problems during my whole PhD program. Next, I would like to thank Dr. Qingsong Wang for his scientific guidance, generous help and valuable insights in my experimental work and battery research. I would also like to thank Dr. Simon Schweidler for his inspiration, constructive discussions and kind support, particularly in the areas of XRD refinement and electrocatalysis.

I would like to appreciate all my coworkers and friends during my PhD journey. Thanks to the group of Prof. Dr. Christian Kübel, particularly Ziming Ding and Dr. Kai Wang, and Karlsruhe Nano Micro Facility (KNMF) for their support in TEM characterization. Thanks to Dr. Abhishek Sarkar for Mössbauer spectroscopy measurement and analysis. Thanks to Dr. Guruprakash Karkera for ICP-OES and XPS analysis. Thanks to Dr. Christian Njel, Dr. Raheleh Azmi, and Dr. Thomas Diemant for XPS measurements and analysis. Thanks to Martin Limbach for his support in the setup and maintenance of many devices. In addition, I would like to thank Dr. Yanyan Cui, Dr. Junbo Wang and Dr. Parvathy Anitha Sukkurji for sharing much experience in material synthesis, electrochemistry and doctoral studies. Thanks to Dr. Miriam Botros, Dr. Yanjiao Ma, Dr. Ibrahim Issac, Dr. Surya Abhishek Singaraju, David Stenzel, Ruby Singh, Mohana Veerraju Kante, Bei Zhou, Anurag Dinesh Khandelwal, Yueyue He, Alaa Alsawaf, Yan Liu and all other INT colleagues for support and help.

I am sincerely grateful to my motherland, China. Thanks to CSC for the financial support and the invaluable opportunity to pursue my PhD studies abroad. Additionally, I would like to thank my MSc supervisor, Prof. Dr. Can-Zhong Lu, as well as the dedicated teachers and supportive colleagues I have encountered throughout my academic journey.

I would like to extend my deepest thanks to my parents and my family for their unwavering support, encouragement and love. Their presence in my life is my greatest fortune. I am also very grateful to my boyfriend for his companionship, steadfast support and numerous help in daily life.

Finally, I would like to appreciate my past efforts and perseverance. Many thanks to all the lovely people who have helped me in my life.